MULTISCALE MODELING OF THERMAL TRANSPORT IN GALLIUM NITRIDE MICROELECTRONICS

A Dissertation
Presented to
The Academic Faculty

by

Adam Paul Christensen

In Partial Fulfillment
of the Requirements for the Degree
Doctor of Philosophy in the
G.W Woodruff School of Mechanical Engineering

Georgia Institute of Technology
December 2009

MULTISCALE MODELING OF THERMAL TRANSPORT IN GALLIUM NITRIDE MICROELECTRONICS

Approved by:

Dr. Samuel Graham, Chair
School of Mechanical Engineering
Georgia Institute of Technology

Dr. Sankar Nair
School of Chemical & Biomolecular Engineering
Georgia Institute of Technology

Dr. Douglas Yoder
School of Electrical & Computer Engineering
Georgia Institute of Technology

Dr. Zhuomin Zhang
School of Mechanical Engineering
Georgia Institute of Technology

Dr. Micheal Leamy
School of Mechanical Engineering
Georgia Institute of Technology

Dr. Donald Dorsey
Electronics and RF Materials Section
Air Force Research Laboratory

Date Approved: [Nov 6, 2009]

ACKNOWLEDGEMENTS

I would like to take a moment to say Thank You to my advisor, Dr. Samuel Graham. The combination of his high expectations as well as his guidance resulted in me pushing myself to grow as an engineer/scientist in ways that I might not have thought possible. This gift is something that I will always be grateful for. I would also like to say a special Thank You to Dr. Douglas Yoder who was also very supportive of the research and offered skilled advice during times of frustration. I would also like to thank several fellow group members that I am proud to say are friends as well as colleagues, Dr. Thomas Beechem, Dr. Roderick Jackson, and Dr. Abe Greenstein. They made life in the Love Building, both intellectually fulfilling as well as fun.

Of course my journey through graduate school could not have been possible with the love and support of my parents as well as my sister. Special recognition also goes to my loving wife, Krista. I am truly blessed to be able to come home at the end of the day to such a supportive and nurturing home where we can relax and have fun together. I truly could not have done it without you and am lucky to have you in my life.

TABLE OF CONTENTS

LIST OF TABLES

Page

LIST OF FIGURES

SUMMARY

One of the most significant advances in GaN devices has evolved from the AlGaN/GaN high electron mobility transistor (HEMT). Technologies that incorporate such devices span the range from next generation WiMAX stations to advanced military radar applications. As a result of the large power densities being applied to these devices there can develop intense hot spots near areas of highest electric field. The hot spot phenomenon has been linked to a decrease in device reliability through a range of degradation mechanisms. In order to minimize the effect that hot spot temperatures have on device reliability a detailed understanding of relevant transport mechanisms must be developed.

This study focuses on two main aspects of phonon transport within GaN devices. The first area of focus was to establish an understanding of phonon relaxation times within bulk GaN. Relaxation times for optical modes were compared to experimental data obtain through Raman Spectroscopy measurements; acoustic phonon relaxation times were calculated to capture the bulk thermal conductivity values. This analysis gives insight into the details behind the macroscopic thermal conductivity parameter. The second area of focus was on developing a multiscale phonon transport modeling methodology to couple the Boltzmann Transport Equation and the energy equation. This coupling overcomes some computational limits and allows for nanoscale phenomena to be resolved within a macroscopic domain. Results of the transport modeling were focused on benchmarking the coupling method as well as calculating the temperature distribution within an operating 6 finger HEMT.

CHAPTER 1

INTRODUCTION

1.1 Motivation and Problem Statement

For the past few decades gallium nitride (GaN) has been given significant attention due its unique set of electronic and optoelectronic properties. Gallium nitride is a wide bandgap semiconductor (3.4 eV) and therefore can be used to create blue and UV emitting LEDs [1]. Through developing compound semiconductor materials based on InGaN or AlGaN, this bandgap can be tuned to allow for low bandgap photovoltaics as well as optoelectronics with a broad range of emission wavelengths. It also possesses a high breakdown voltage (~$5x10^6$ V/cm) that is approximately 10 times that of silicon. The large breakdown voltage allows for the development of devices that can operate under much larger power densities (>30 W/mm) [2, 3]. Typical applications for GaN-based electronics include next generation WiMAX stations, advanced military radar applications, and high power light emitting diodes that are used for general lighting applications [4-8]. While development of GaN-based electronics has seen enormous growth due to improvements in epitaxial growth technology, further development has been hampered by reliability and performance concerns [9]. While the exact mechanisms that cause this decrease in performance have yet to be determined, studies have shown that defect formation, cracking and dopant diffusion may play a major role [10-12]. Even though there is some debate as to the exact degradation mechanism there remains an empirical link between the operational temperature, device stress state and device reliability. In addition to these mechanical failure modes, electrically induced impact ionization (avalanche breakdown) can lead to rapid increases in device current

and ultimately failure of the device. The subject of this work will be to examine the details of the operational temperature through computational results. These computational results will be facilitated through the use of a multiscale thermal model that includes critical information about the complicated energy relaxation pathways and timescales starting from high energy electrons to rapidly propagating acoustic phonons.

Though GaN based electronics are being developed for a variety of applications, one of the most important is based on the AlGaN/GaN heterojunction field effect transistor which can be used in radio frequency (RF) and power applications. These high electron mobility transistors (HEMTs) are capable of operating at frequencies above 150 GHz and at power densities >10 W/mm [13]. The majority of the power that is dissipated to the crystal lattice occurs in a region close to the gate as seen in Figure 1 and Figure 2. Due to the nature of the transport and interaction between charge and thermal energy carriers, a localized "hot spot" develops that, if not controlled, can lead to device failure.

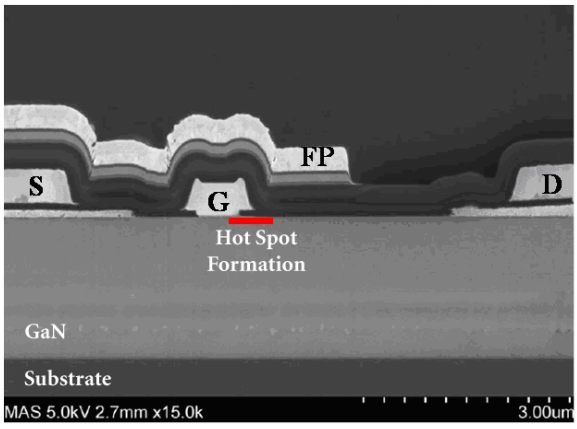

Figure 1: Cross-Section view of an AlGaN/GaN device with the hot spot area shown in red. This particular device also includes a field plate (FP) above the source and gate contacts (figure adopted from [14])

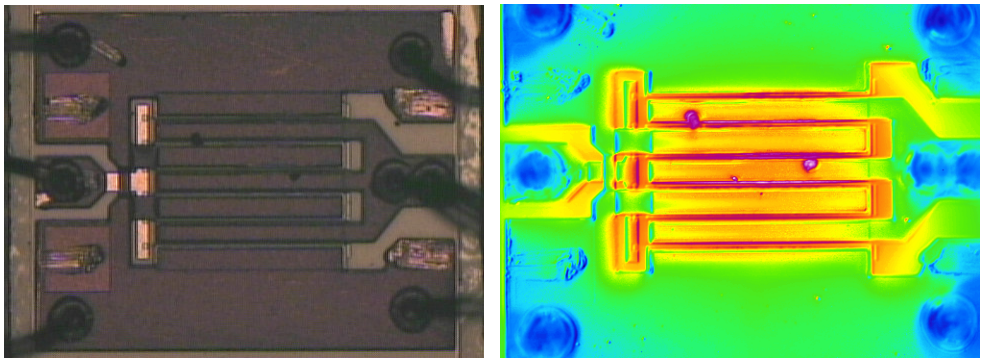

Figure 2: (Left) Optical microscope image of a 6 finger GaN High Electron Mobility Transistor (HEMT); top view. (Right) Infrared image of the same device under operating conditions; highest temperatures are seen in the vicinity of the gate [15].

The process of transferring energy from high energy electrons to the crystal lattice (in the form of phonons) is not trivial, however it has been quantified by several groups for both GaN and silicon based systems [16, 17]. These simulations have detailed the electron-phonon interactions in the channel, but rely on simplified heat transfer models based on Fourier diffusion to account for the energy propagation within the device. There is an inherent assumption that energy carriers are in local equilibrium states when the diffusion equation is used to model heat transfer. In order to account for the underlying non-equilibrium nature of the phonon energy a solution method based on the Boltzmann Transport Equation (BTE) is necessary. In addition to ignoring the non-equilibrium nature of the phonon distribution, the diffusion equation modeling method also ignores the discrete nature of the phonons. The discreteness of crystal lattice gives rise to several types of vibrational phonon modes, each mode has the ability to carry heat but that burden is not carried equally among all. Optical phonons, which tend to interact preferentially with electrons, due to energy and momentum conservation restrictions, are slow moving and can take a relatively long time to decay into rapidly propagating acoustic modes. In silicon devices typical phonon emission times are on the order of 10

fs while their relaxation times can be several orders of magnitude longer (~5 ps). This disparity results in a non-equilibrium optical phonon population that behaves as a thermal energy capacitor. In GaN devices this thermal capacitor effect is compounded by the presence of a phononic bandgap, which hinders the decay of high-energy optical phonons. This bandgap is illustrated in Figure 3.

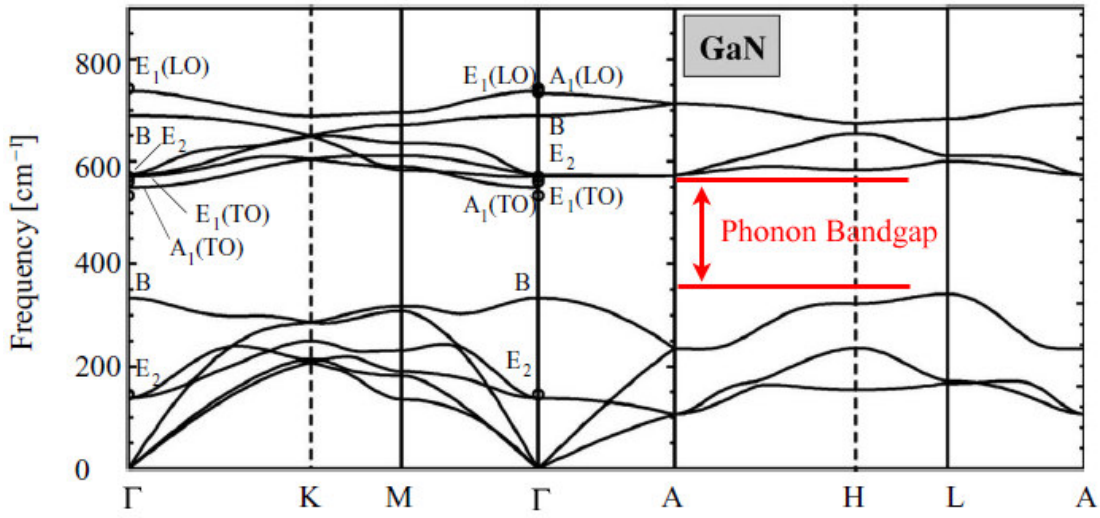

Figure 3: Phonon dispersion curves and density of states calculated by a bond charge model [18].

High-energy electrons will typically interact with zone center phonon modes, through the Fröhlich interaction. These non-equilibrium phonons will eventually relax through several scattering processes. During this relaxation process, a high energy phonon will tend to decay into a high energy mode as well as an acoustic mode; this process is typically referred to as the Ridley process [8-11]. The resulting mode is also plagued by small group velocities as well as by relatively long phonon lifetimes before they can they decay into lower energy phonon modes that can dissipate the energy. This intermediate

phonon decay process can lead to a bottleneck effect, i.e. when the energy loss rate from electron scattering events is greater than the decay rate of optical phonon modes. Thus, regions in the vicinity of the hot spot can experience drastic increases in the effective temperature due to these optical phonons. While non-equilibrium phonon populations are difficult to probe experimentally, their effect is hypothesized to be a contributing factor to the device failure rate.

One common method used by reliability engineers to quantify the failure rate of a device is to extrapolate out from experimental data using an Arrhenius equation in which this rate increases with increasing temperature. As an input parameter, the Arrhenius model relies on accurate knowledge of the failure mechanism's activation energy. The activation energy parameter intrinsically accounts for a number of degradation mechanisms (dislocation formation, material cracking, metal contact diffusion, dopant diffusion, etc.) [19]. Thus, fitting this type of model to experimental data allows the activation energy to be determined and allows the device lifetime to be estimated at other operating conditions. In general, the activation energy is determined through electrical stress testing and related to the device junction temperature, which has not been directly measured. Typically, optical methods are used to measure GaN device temperatures (e.g., IR, Raman, thermoreflectance, etc.). However, these methods lack spatial resolution or the ability to directly probe the hot spot near the gate, especially when a field plate is located above the gate contact. Thus, device temperatures are generally measured within the visible channel and across the metal contacts. These temperatures are then used as inputs to an inverse heat transfer calculation which predicts the actual hot spot temperature. Other methods have been proposed and attempt to calculate a

thermal resistance for the device based on power dissipation. With this thermal resistance value it is then possible to predict the junction temperature rise over the base plate temperature used during stress testing. Regardless of the method used, some type of model is critical in determining the hot spot temperature at the junction, which is then related to device failure. An under prediction of the hot-spot temperature may lean to erroneous conclusions in determining the mechanisms of failure such as eletro-thermo-mechanical behavior, device cracking, material diffusion, and trap depopulation. Thus, beyond the accounting for activation energy, accurate temperatures are needed for proper assessment of specific phenomena that can lead to failure.

The need for a detailed model of the phonon transport, which can better resolve temperatures at the hot spot, has led to the development of several computational tools. The two main approaches for quantifying phonon transport at these scales have led to molecular dynamics (MD) simulations as well as in the development of tools to solve the Boltzmann transport equation. Both of these tools will be discussed in greater detail in Chapter 3. It is important to note now that whichever method is ultimately used, there are large computational loads that must be addressed if the problem is to be solved. These loads can be partially handled through several variants of parallel computation (spatial decomposition, massively parallel MD algorithms, etc…) [20, 21]. Even still, modeled physical domain sizes have been limited to a range of ~100 nm -1 μm. Computational domains of this size must rely on simplified boundary conditions, which could result in inaccurate hot spot temperatures. Even still, careful modeling of these small domains can be acceptable for current silicon technologies as the characteristic lengths of a silicon-based FET is typically on the order of 50-100 nm, as seen in Figure 4. However, there

are issues in limiting the domain to the nanometer scale when simulating GaN based HEMTs as the characteristic length of these devices is on the order of microns (typical gate lengths can be ~300-400 nm while the gate-drain spacing can be 2-4 μm).

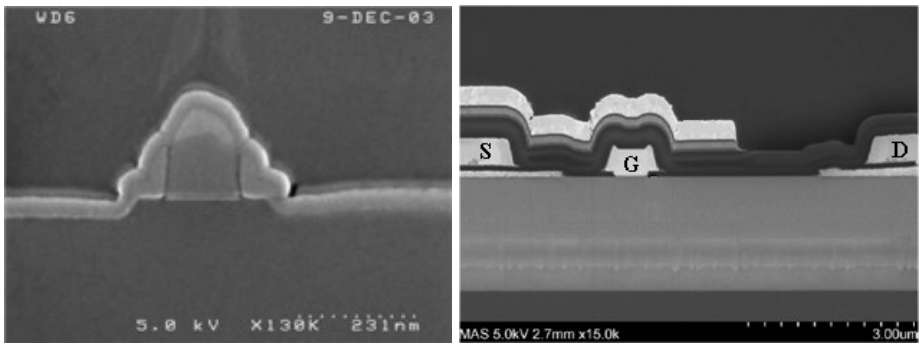

Figure 4: The cross-section scanning electron microscope image of a silicon based FET device (left) and a GaN HEMT (right). The GaN HEMT has a characteristic length many times that of the silicon device [14].

Already, phonon relaxation processes have been discussed as a critical component of the transport model and as such a model should be developed that incorporates these nanoscale processes within these macroscopic devices. To this end, a multiscale computational approach is desired in order to capture these effects. In order to bridge several transport scales the strategy of coupling the Boltzmann transport equation to the energy equation is proposed. In regions where the granularity of the phonon transport process is of critical importance the BTE is solved in order to capture details that are lost when a diffusive based modeling approach is taken. The multiscale strategy addresses the problem introduced by large computation loads associated with BTE modeling and provides a convenient method to apply boundary conditions on nanoscale domains. As briefly mentioned, applied boundary conditions are often simplified for BTE domains in order to approximate heat transport through the substrate material and the electronic

package that are external to the domain. These simplified boundaries are often approximated as Neumann conditions that reflect an effective package thermal resistance; approximations that assume a constant temperature boundary have also been utilized. Using these inaccurate boundary conditions have been shown to have a direct effect on the ultimate temperature distribution inside the device [22]. By taking the multiscale modeling approach some of these concerns can be eliminated as the computational domain size better reflects the physical scale of the device under test.

1.2 Specific Methods and Outline of Study

The findings in this study will contribute in two primary areas of research that are subjects of interest in GaN based electronics; phonon transport modeling via solutions to the Boltzmann Transport Equation and phonon relaxation time calculations. In the phonon transport modeling, a multiscale thermal transport tool has been developed to couple the Boltzmann transport equation and the energy equation utilized for diffusive transport. The Boltzmann transport equation is solved through the application of the Lattice Boltzmann method. The theory behind the coupling method is developed and numerical errors that are introduced are discussed in detail in Chapter 3. Within the framework of the Lattice Boltzmann method, several phonon dispersion models (gray and two-fluid) are incorporated in order to resolve dispersive effects of high energy optical phonons; this work is contained in Chapter 5. The main input parameters for these transport simulations are the phonon group velocities and relaxation times. For the gray and two-fluid phonon models a mode averaged group velocity is calculated from phonon dispersion curves that have been generated from lattice dynamical calculations. This group velocity is used to back calculate a mode averaged relaxation time. In this manner

the bulk thermal conductivity values will always be recovered at large length scales. This method of calculating the relaxation time is straight forward and provides some qualitative information about the behavior of phonons; however a more detailed understanding of the energy relaxation process is desired. To address this, the calculated phonon dispersion curves were analyzed in order to find 3-phonon interactions that abide by momentum and energy conservation. Upon finding triads of interacting phonons the phonon transition probability and ultimately the anharmonic relaxation time are calculated using Fermi's Golden Rule as discussed in Chapter 4. The developed theoretical model has been fit to temperature dependent relaxation time data for zone center optical phonons available from literature; these values are typically measured with Raman spectroscopy linewidth methods or time-resolved Raman spectroscopy. Using these theoretical models to correlate with the data, the phonon relaxation time along different directions of the Brillouin zone is predicted in order to investigate any possible anisotropic phonon transport processes. In addition to calculating the optical phonon relaxation times, it was necessary to investigate trends of the three acoustic modes as well. The relaxation time data that have been generated from the above calculations sheds some unique insight into the problem of heat transport in GaN based devices. This data was also used in order to verify that the bulk thermal conductivity of GaN is recovered from the modeled relaxation times. Several previous studies have calculated the theoretical thermal conductivity of GaN; however these investigations have relied on simplified Brillouin zone volumes as well as simplified dispersions curves [23-28]. These simplifying assumptions are not made in this study. The final portion of this study,

located in Chapter 6, serves to summarize the major findings contained in the previous chapters as well as to discuss future directions for this research.

CHAPTER 2

HEAT TRANSPORT IN CRYSTALLINE MATERIALS

This chapter begins by outlining some of the basic theory used in the study of heat transport in crystalline materials. It proceeds with a review of current transport modeling tools including molecular dynamics as well as other partial differential equation (PDE) based models. Transitioning from this review, the Boltzmann transport equation is presented and several numerical methods are highlighted that were designed to solve the BTE.

2.1 Heat Transport in Crystalline Materials

2.1.1 Phonons

In many macroscale engineering applications the description of heat transport is adequately described through the application of the energy equation shown in Eq. (2.1).

$$k\nabla^2 T = \rho c_p \frac{\partial T}{\partial t} \tag{2.1}$$

Here, ρc_p is the specific heat capacity and k is the diffusion coefficient commonly called the thermal conductivity. The parameter k describes the how efficient heat can diffuse through a material and is typically considered a temperature dependent quantity. The processes that determine the magnitude of k are complex and have their roots in how a specific material is structured on the atomic level. Properties, such as crystal structure, bond strength, density, and other microscopic properties all contribute to the final value

of the thermal conductivity. These properties act together to either enhance or inhibit motion of heat carriers; the primary heat carriers in solids are electrons and phonons. In the case of semiconductor materials, such as GaN, the number of free electrons is small and as such the majority of heat is carried through phonon motion [29, 30]. In short, these phonons are crystal vibrations that have been generated by a disturbance from the equilibrium atomic positions of a crystal lattice. The disturbance can be generated by a number of external forces but phonons can also be generated through scattering events that involve other particles such as electrons. The resulting vibration carries with it an amount of energy as it travels throughout the crystal lattice; this is the mechanism for heat transport in semiconductor materials. These vibrations will be mathematically treated as waves that travel throughout the material. At small length scales, the wave nature of these phonons is important to consider when modeling transport. Since the thermal conductivity is a macroscopic quantity, the details of this wave-like behavior are lost although their averaged effect is captured. Even when the averaged effect is captured, modeling thermal transport in microelectronic devices with a thermal conductivity parameter may result in an under predicted maximum temperature.

The vibrational properties of these generated phonons are determined by an examination of the interatomic potential. In a simple system the interatomic potential can be model as a harmonic spring as in the following diatomic linear chain shown in Figure 5.

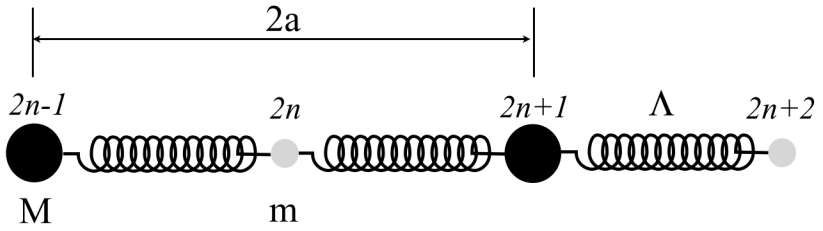

Figure 5: Diatomic linear chain of atoms modeled with a harmonic spring force as the interatomic potential.

In this perfectly periodic system the crystal dynamics can be described in terms of the linear combination of waves modes. A wave mode is described as a traveling wave with the form $A\exp\left[i\left(\mathbf{q}\cdot\mathbf{r}-\omega t\right)\right]$, where **q** points in the direction of wave propagation, ω is the angular frequency, and *A* is the amplitude, and **r** is the atomic position vector. The equations of motion for this diatomic linear chain are written from Newton's law and Hooke's law and assuming only nearest neighbor interactions are significant [31].

$$m\frac{d^2u_{2n}}{dt^2}=\Lambda\left[u_{2n+1}+u_{2n-1}-2u_{2n}\right] \tag{2.2}$$

$$M\frac{d^2u_{2n+1}}{dt^2}=\Lambda\left[u_{2n+2}+u_{2n}-2u_{2n+1}\right] \tag{2.3}$$

Here, u_{2n} is the displacement of the atom at the *2n* position. To solve the system of ordinary differential equations a wave mode solution for the displacements is investigated.

$$u_{2n}=A_1\exp\left[i\left(2nqa-\omega t\right)\right] \tag{2.4}$$

$$u_{2n+1}=A_2\exp\left\{i\left[\left(2n+1\right)qa-\omega t\right]\right\} \tag{2.5}$$

Upon substitution of Eq. (2.4) and (2.5) into (2.2) and (2.3) the previous system of ODEs is transformed into an eigenvalue equation.

$$-\omega^2 m A_1 = \Lambda\left[A_2 e^{iqa} + A_2 e^{-iqa} - 2A_1 \right] \tag{2.6}$$

$$-\omega^2 M A_2 = \Lambda\left[A_1 e^{-iqa} + A_1 e^{iqa} - 2A_2 \right] \tag{2.7}$$

By defining a matrix *D*, called the dynamical matrix the equations shown in Eq. (2.6) and Eq. (2.7) can be rewritten in the form of Eq. (2.8).

$$\omega^2 A_i = \sum_{j=1}^{2} D_{ij} A_i \tag{2.8}$$

$$D = \begin{pmatrix} 2\Lambda/m & -(2\Lambda/m)\cos qa \\ -(2\Lambda/M)\cos qa & 2\Lambda/M \end{pmatrix} \tag{2.9}$$

Solutions to Eq. (2.8) are found by solving for the eigenvalues of the dynamical matrix.

$$\left| D_{ij} - \omega^2 \delta_{ij} \right| = 0 \tag{2.10}$$

For this problem the solutions have a closed form analytical solution that describes the relationship between the frequency and the wavevector; this relationship, $\omega(\mathbf{q})$, is referred to as the dispersion relationship.

$$\omega^2 = \Lambda\left(\frac{1}{m}+\frac{1}{M}\right)\pm\left[\left(\frac{1}{m}+\frac{1}{M}\right)^2-\frac{4}{mM}\sin^2 qa\right]^{1/2} \tag{2.11}$$

The two signs in Eq. (2.11) correspond to two different types of vibrational modes as depicted in Figure 6; therefore the dispersion relationship is a multivalued function for every unique wavevector.

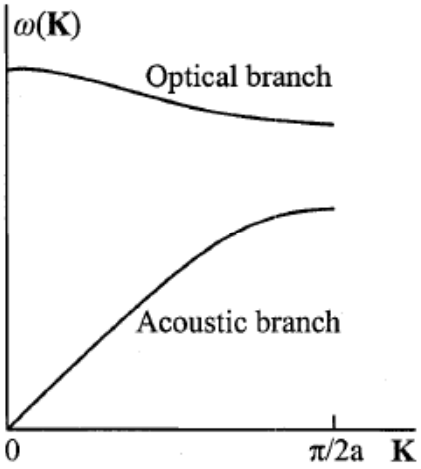

Figure 6: Simple phonon dispersion curve for a diatomic linear chain of atoms. Reproduced from [32].

There are several artifacts that are important to highlight in the above dispersion relationship. First is that the maximum meaningful wavevector is directly related to the lattice spacing. This is analogous to saying that the minimum wavelength that a phonon can have is twice the lattice constant (a). The extent of the wavevector space is referred to as the Brillouin zone; this zone contains information about all possible normal modes available in a crystal. In a 1D system the Brillouin zone is simply a line, in a 2D system

the Brillouin zone is an area that can be constructed in the same manner as the Wigner-Seitz cell is created. In a general 3D crystal the Brillouin zone is defined as a volume and has a more complicated shape. For example, silicon's (diamond crystal) Brillouin zone is a truncated octahedron, and GaN's (hexagonal crystal) Brillouin zone is a hexagonal prism as seen in Figure 7.

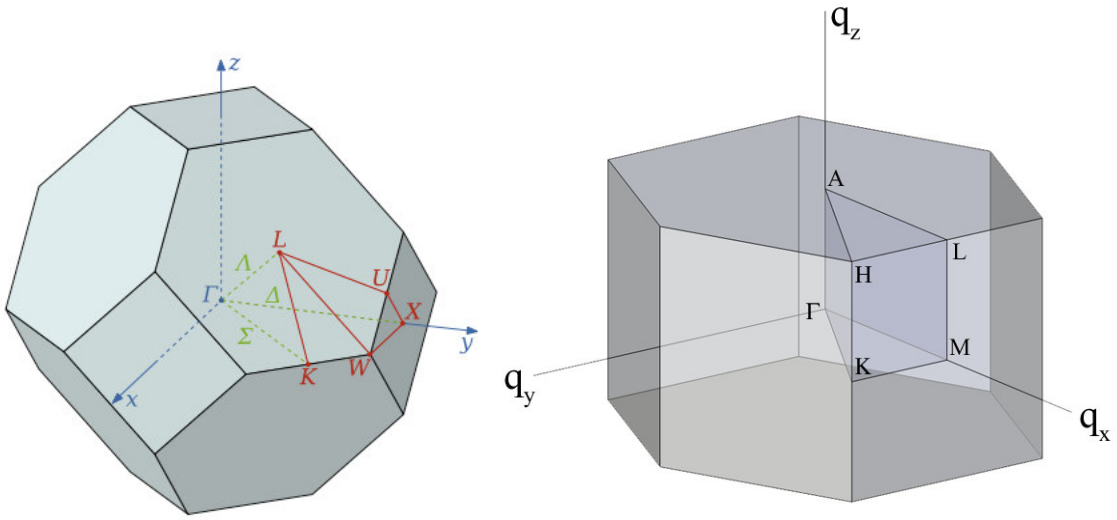

Figure 7: Brillouin zone shape and high symmetry points for silicon (left) and GaN (right).

The second important artifact that should be highlighted above dispersion curves is that as the masses of the two atoms in the unit cell differ, there is a gap that forms at the edge of the Brillouin zone. This gap is similar to an electronic bandgap and is important since it affects available phonon decay pathways. In silicon there is only one type of atom in a unit cell and therefore there is no phononic bandgap; in GaN the mass ratio is $m_{Ga}/m_N = 4.98$ and therefore a significant phononic bandgap exists. Further effects of this bandgap phenomenon will be discussed in a later chapter.

The modeled interatomic potential used to solve the above diatomic linear chain problem was simply a harmonic spring type relationship. To model more complicated

materials a more detailed force field is needed to correctly resolve different types of bonds as well as bond angles. In a 3D crystal the harmonic approximation is still utilized and the total crystal potential energy can be expanded in a Taylor series of atomic displacement, $\mathbf{u}(\mathbf{lb})$, of the an atom with a basis vector $\mathbf{b}$ in the unit cell at position $\mathbf{l}$. Following the notation in [31],

$$V = V_o + \sum_{\mathbf{lb}\alpha} \left.\frac{\partial V}{\partial u_\alpha(\mathbf{lb})}\right|_o u_\alpha(\mathbf{lb}) + \frac{1}{2}\sum_{\mathbf{lb},\mathbf{l'b'}}\sum_{\alpha\beta}\Phi_{\alpha\beta}(\mathbf{lb};\mathbf{l'b'})u_\alpha(\mathbf{lb})u_\beta(\mathbf{l'b'}) + \ldots$$
$$V = V_o + V_1 + V_2 + \ldots \tag{2.12}$$

where V_o is the equilibrium value of the potential energy and

$$\Phi_{\alpha\beta}(\mathbf{lb};\mathbf{l'b'}) = \left.\frac{\partial^2 V}{\partial u_\alpha(\mathbf{lb})\partial u_\beta(\mathbf{l'b'})}\right|_o \tag{2.13}$$

The first two terms of the expanded potential do not contribute to the dynamical problem, only the harmonic term, V_2, is critical. The generalized equations of motion are then

$$m_b \ddot{u}_\alpha(\mathbf{lb}) = -\sum_{\mathbf{l'b'}\beta}\Phi_{\alpha\beta}(\mathbf{lb};\mathbf{l'b'})u_\beta(\mathbf{l'b'}) \tag{2.14}$$

After assuming solutions exist in a form similar to Eq. (2.4) and by defining a dynamical matrix D, the eigenvalue problem is in the form

$$\left| D_{\alpha\beta}\left(\mathbf{bb}'\,|\,\mathbf{q}\right) - \omega^2 \delta_{\alpha\beta}\delta_{\mathbf{bb}'} \right| = 0 \tag{2.15}$$

where D has the form

$$D_{\alpha\beta}\left(\mathbf{bb}'\,|\,\mathbf{q}\right) = \frac{1}{\sqrt{m_b m_{b'}}} \sum \Phi_{\alpha\beta}\left(\mathbf{0b};\mathbf{l}'\mathbf{b}'\right) \exp\left[i\mathbf{q}\cdot\mathbf{x}\left(\mathbf{l}'\right)\right] \tag{2.16}$$

The dynamical matrix is then a *3p x 3p* matrix, where *p* is the number of atoms in the unit cell. A detailed formulation of the dynamical matrix can be found in [33, 34]. The eigenvalues of the dynamical matrix are then equal to ω^2. From Figure 7 there are special high symmetry directions in the 3D Brillouin zone that are of particular interest. A 2D plot of the dispersion relations for a 3D crystal is shown in Figure 3 where the *x*-axis marches along line segments between special points in the Brillouin zone.

In addition to providing the $\omega(\mathbf{q})$ relationship the dispersion curves also reveal information about the group velocity of the phonons. The group velocity is related to the wavevector through the following relationship.

$$\mathbf{v} = \nabla_{\mathbf{q}}\omega \tag{2.17}$$

From this expression it is obvious that for some phonon modes, particularly optical modes, the group velocity is near zero. This means that these modes are poor at transporting energy since they are standing waves inside the crystal.

2.1.2 Phonon Statistics

Phonons have been treated as a wave for the dynamical problem as briefly outlined in the previous section. While the wave picture of phonons provides physical insight and mathematical convenience, it does not tell the whole story; for a general material there may be phonon frequencies that cannot exist. This implies that the energy of a lattice vibration is actually quantized with an energy equal to $(n+1/2)\hbar\omega$, where n is a quantum number [32]. In this way phonons exhibit properties of waves as well as particles, similar to photons, and are therefore referred to as *quasi*-particles. Additionally, as a matter of convenience, the quantum number is generally not referred to but rather the number of phonons present with wavevector $\mathbf{q}$ and polarization s [35]. The Bose-Einstein distribution, which describes the number of phonons with a certain wavevector and polarization, is given by

$$n_s(\mathbf{q}) = \frac{1}{\exp\left(\hbar\omega_s(\mathbf{q})/k_bT\right)-1} \tag{2.18}$$

Here, k_b is Boltzmann's constant. To continue the analogy with photons, the concept of crystal momentum is introduced. Phonons cannot carry physical momentum since there is only relative motion of atoms rather than bulk motion of their center of mass. However, phonons can be characterized as having a quantity of crystal momentum, $\hbar\mathbf{q}$, which must be conserved during any scattering processes that may occur [35]. This conservation law combined with conservation of energy forms the basis for how phonon-phonon

interactions occur; these interaction processes will be discussed in more detail in the next section.

While phonons are responsible for energy transport in solids they are also responsible for temperature trends in the specific heat of a material. The internal energy of a material is defined by Eq. (2.19).

$$u = u_o + \frac{1}{V}\sum_{\mathbf{q}s}\frac{1}{2}\hbar\omega_s(\mathbf{q}) + \frac{1}{V}\sum_{\mathbf{q}s}\frac{\hbar\omega_s(\mathbf{q})}{\exp\left[\hbar\omega_s(\mathbf{q})\big/k_bT\right]-1} \tag{2.19}$$

In the first two terms there is no dependence on temperature, the entire contribution to the specific heat is obtained from the third term.

$$c_v \equiv \frac{\partial u}{\partial T} = \frac{1}{V}\sum_{\mathbf{q}s}\frac{k_b x^2 e^x}{\left(e^x-1\right)^2} \tag{2.20}$$

The non-dimensional frequency, x, has been defined as $\hbar\omega_s(\mathbf{q})/k_bT$ and the summation is taken over all wavevectors and all polarizations. Details of the high and low temperature limiting cases are given in [35]. In some cases it is desirable to transform the summation over all wavevectors into an integral over all phonon frequencies. This transformation is used to highlight the distribution of phonon frequencies in a material. To perform this transformation the density of states must be defined as Eq. (2.21).

$$g(\omega) = \sum_s \int \frac{d\mathbf{q}}{(2\pi)^3} \delta(\omega - \omega_s(\mathbf{q})) \tag{2.21}$$

Using the definition for the density of states another useful quantity, the phonon occupation number, can also be defined.

$$f(\omega) = n(\omega(\mathbf{q}))\, g(\omega) \tag{2.22}$$

The phonon occupation number is a useful quantity because it describes phonon states that are excited at a temperature *T*; phonons with energy $\hbar\omega \gg k_b T$ will not be active in equilibrium conditions as they are "frozen-out".

2.1.3 Phonon Interaction Processes

A phonon can be viewed as a wave that propagates through the crystal lattice. If this propagating wave encounters any disturbance in the periodicity of the crystal there is an opportunity for the phonon to scatter. These disturbances can be in the form of point defects, impurity atoms, dislocations, or boundaries. Additionally, scattering with other phonons is possible through anharmonic interactions. The effect of these scattering events is to reduce the effective relaxation time. The relaxation time is a characteristic time constant in which a phonon in an excited state will relax back to an equilibrium state. The rate of change in the phonon distribution function due to scattering can be approximated by with the single mode relaxation time approximation.

$$\left(\frac{\partial n}{\partial t}\right)_{scatter} \approx \frac{n^o - n}{\tau} \tag{2.23}$$

This approximation forces phonon relaxation to behave with an exponential dependence.

$$n - n^o = e^{-t/\tau} \tag{2.24}$$

It is important to note that during this time there is no account of how many scattering processes actually occur, only the time constant of relaxation is known [29]. In Eq. (2.23) and (2.24) n^o is the equilibrium phonon distribution function.

Phonon interactions that occur with defects, impurity atoms, dislocations, and boundaries are typically thought of as temperature independent quantities. They are, however, functions of phonon frequency. If a material is of very poor quality the combined effects of these scattering mechanisms overshadow any of the temperature dependence of the total relaxation time. This results a small and nearly temperature-independent thermal conductivity. On the contrary, if the material is of high quality, the contribution to the total relaxation time from these temperature independent scattering mechanisms is small; the thermal conductivity can then be a strong function of temperature. Klemens studied the frequency dependence of mass difference scattering, dislocations, and stacking faults and found their dependence to proportional to ω^4, ω, and ω^2 respectively [22-24]. Klemens also studied scattering on grain boundaries (modeled as a plane of dislocations) and found a frequency dependence of ω^2 if the planes were spaced at distances less than the phonon wavelength [36]. An ω^n dependence (where n is between 0 and 1) was found if the planes were taken as independent from

each other [37]. Boundary scattering of phonons was proposed to not have a frequency dependence, but rather a dependence on group velocity such that

$$\tau_b^{-1} = v/LF \tag{2.25}$$

where L is the equivalent sample size and F is a geometrical factor [26-29].

The temperature dependent phonon scattering mechanism is primarily in the form of phonon-phonon scattering. Phonons, in the harmonic potential approximation will not interact with each other; therefore a V_3 term in Eq. (2.12) must be included to study phonon interactions. This term is the anharmonic component of the crystal potential as shown graphically in Figure 8. The anharmonic component of the potential causes phonons to scatter with each other, but it is also responsible for macroscopic effects such as thermal expansion [38].

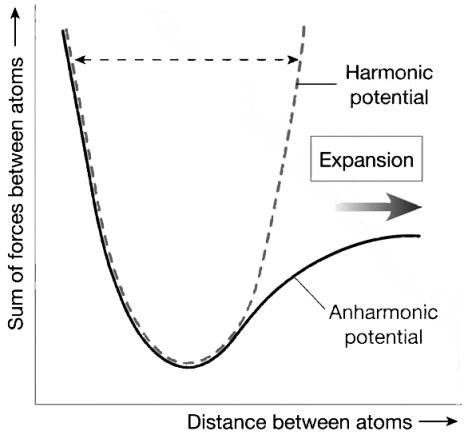

Figure 8: Sample Interatomic potential that is showing the harmonic potential approximation, and the true anharmonic potential.

When phonons scatter with other phonons conservation of energy and conservation of crystal momentum must be maintained. These two restrictions allow only certain phonons to interact together due to the complicated and non-linear nature of the dispersion curves. Phonon collisions can be described as Class 1-type events or Class 2-type events, as suggested by [31]. Class 1 (fusion) events occur when two phonons fuse together to form a third phonon.

$$\mathbf{q}+\mathbf{q}'=\mathbf{q}''+\mathbf{G} \tag{2.26}$$

$$\omega_s(\mathbf{q})+\omega_s(\mathbf{q}')=\omega_s(\mathbf{q}'') \tag{2.27}$$

In contrast, a phonon can decay into two lower energy phonons following a Class 2 (fission) event.

$$\mathbf{q}+\mathbf{G}=\mathbf{q}'+\mathbf{q}'' \tag{2.28}$$

$$\omega_s(\mathbf{q})=\omega_s(\mathbf{q}')+\omega_s(\mathbf{q}'') \tag{2.29}$$

The vector **G** is a reciprocal lattice vector, and appears if (in the case of a Class 1 event), the resultant third phonon lies outside the first Brillouin zone; adding the **G** vector causes the third phonon to flip back inside. Processes that occur without the addition of a **G** vector are called Normal processes (N-process), while processes that rely on the addition of a reciprocal lattice vector are called Umklapp processes (U-processes). It is evident that U-processes result in a phonon that has crystal momentum that is in the opposite direction from $\mathbf{q}+\mathbf{q}'$. These U-processes therefore result in a resistance to heat flow through a material, while N-processes do not provide a direct resistance to heat flow. It

has been discussed that N-processes redistribute low momentum phonons into states that will then scatter through U-processes [39, 40]. This indirect resistive process is still critical to include in the theory of phonon scattering and thermal conductivity. Full calculation of the relaxation times in GaN is presented in Chapter 4; however it is important to discuss the frequency and temperature dependencies of these processes now. In the literature there are a number of approximations made to estimate the scattering rate for both N and U processes. These approximations have been tuned for both high and low temperatures as well as for acoustic phonon modes. In considering an N-process first, the scattering rate is proportional to $\omega^2 T^3$ for longitudinal modes and proportional to ωT^4 for transverse modes, both at low temperatures [41]. At high temperatures these dependencies change and behave as $\omega^2 T$ and ωT, for longitudinal and transverse modes respectively [41]. For a general U-process, at any temperature, Klemens suggested that

$$\tau_u^{-1} \propto \omega^2 T^2 \exp\left(-\theta/\alpha T\right) \tag{2.30}$$

where θ is typically taken to be the Debye temperature. The Debye temperature is a theoretical value that describes the temperature at which all phonon modes have been excited. Additionally, the Debye temperature can be thought of as a measure of the "stiffness" of the bonds in the material. In Eq. (2.30) α is a parameter that depends on the phonon spectrum [42, 43]. A refinement to account for dispersive transverse acoustic modes was suggested to follow [44].

$$\tau_U^{-1} \propto \begin{cases} \dfrac{\omega^2}{\sinh x} & \text{for } \omega_1 < \omega < \omega_2,\ x = \hbar\omega / k_b T \\ 0, \text{ for } \omega < \omega_1 \end{cases} \tag{2.31}$$

Callaway's approximation differed slightly from Klemens' as he suggested the scattering rate was proportional to $\omega^2 T^3$, without the exponential dependence on temperature [45]. To emphasize, all of these scattering rates are for acoustic phonon modes only; the assumption being that acoustic phonons contribute most to the bulk thermal conductivity. The proportionality constant that exists in all these approximations is a complicated parameter, and typically is treated as a fitted constant to resolve experimental data. Additionally, with these models simplified Brillouin zone volumes are typically assumed; as in the Debye model [35]. While there are deficiencies in the modeling of the thermal conductivity with these methods, the trends with frequency and temperature provide valuable insight into the nature of phonon scattering processes. A more complete analysis of phonon relaxation times in GaN is presented in Chapter 4.

All the processes described above occur simultaneously within a material. The cumulative effect from all these scattering processes can be found through application of Matthiessen's rule.

$$\frac{1}{\tau_{total}} = \sum_i \frac{1}{\tau_i} \tag{2.32}$$

2.2 Computational Models for Phonon Transport

2.2.1 Ballistic-Diffusive Equations

The ballistic diffusive equations were derived from the Boltzmann transport equation with the idea in mind that the phonon distribution function n can be divided up into two components, $n = n_b + n_m$. In this model the component n_b originates from the boundary of the domain, while n_m originates from within the domain. In this way the boundary term can be handled with the Boltzmann transport equation and the interior transport is handled through a modified hyperbolic heat equation [30, 46]. Results for test cases have revealed good agreement when compared to a full BTE solution. Recent emphasis has been focused on benchmarking the BD-equations for bridging nano to macro scales [47], conduction in superlattices [48], and multidimensional problems [49]. These methods have not included effects of phonon dispersion; later an extension of the method was made to include polarization and dispersion effects [50]. The method was shown to work well within the computational domain, however deviations at the boundaries were shown to exist making the method not as appealing for nanoscale structures [34, 50].

2.2.2 Molecular Dynamics

Molecular dynamics simulations have recently been used to study phonon properties, phonon transport, and thermal conductivity [41-46]. These tools require, as an input, knowledge of the interatomic potential for the structure under investigation. From this point a simulation domain is defined and the individual atomic motions are solved (Newton's laws) for at every time step, typical time steps can be on the order of femtoseconds. Since the only input in these models is the interatomic potential, all phonon branches are inherently considered during the simulations. Typical output from MD simulations must be post-processed in order to resolve key parameters such as

thermal conductivity and phonon relaxation times. While the post-processing step is not trivial, MD provides a way to study basic thermal properties of nanostructures. The major limitation with molecular dynamics tools is due to the associated computational load. With systems on the order of thousands of atoms it is possible to run on a desktop computer, but domains much larger than this require massively parallel systems to obtain reasonable simulation times. In this study system sizes are on the order of microns and larger, therefore MD is not suitable at this time.

2.2.3 Atomistic Green's Functions

An atomistic Green's function method was recently developed by Mingo *et al.*. that has been used to calculate phonon transport in Si-Ge heterostructures [51, 52]. This method has also been used to study the thermal boundary resistance between two dissimilar materials. An extension of the method was proposed that includes anharmonic effects and has studied phonon flow through molecular-sized junctions [53].

While the Green's function method has provided promising results, the computational burden has limited it to systems with small numbers of atoms. Similar to MD, it was not possible to simulate full sized microelectronic devices with the AGF method.

2.3 Boltzmann Transport Equation

2.3.1 Background

A useful quantity known as the Knudsen number can be used a metric to probe the nature of transport in a material. The Knudsen number is defined as the ratio of the mean free path of the heat carriers to some characteristic length in the system.

$$Kn = \frac{\Lambda}{L} \tag{2.33}$$

As the Knudsen number approaches values of 1 or higher, the wave nature of the phonons begins to take precedence and must be included to perform accurate studies of thermal transport. For this study phonon transport was considered by solving the Boltzmann transport equation (BTE). The BTE describes the spatial and temporal evolution of the phonon distribution function, in this case the Bose-Einstein distribution. The full phonon BTE can be written as [54].

$$\frac{\partial n}{\partial t} + \mathbf{v} \cdot \nabla_x n = \left(\frac{\partial n}{\partial t} \right)_{scatter} \tag{2.34}$$

In Eq. (2.34) n is the distribution function, $\mathbf{v}$ is the group velocity, and the right hand side describes the evolution of the distribution function due to scattering events. By taking a modeling approach based on the BTE there are inherent assumptions that the domain being studied is large enough that coherent quantum effects can be ignored. Therefore at very large Kn numbers (very short length scales) there is a possibility for the semi-classical description of the BTE to produce inaccurate results. However, for quantum coherence effects to play a significant role the domain size should be on the order of the phonon wavelength. At these sizes, other tools such as MD and AGF methods mentioned earlier should be investigated. This study focuses on domains that are much larger than

the phonon wavelength, and as such the BTE provides strong foundation for phonon transport in microelectronic devices.

The BTE presents difficulties when trying to solve the equation in full, primarily due to the scattering term on the right side of Eq. (2.34). The 3-phonon scattering term can be defined as in [39].

$$\left(\frac{\partial n}{\partial t}\right)_{scatter} = \sum_{\mathbf{q},\mathbf{q}'} \left\{ \begin{array}{c} \left[n_{\mathbf{q}} n_{\mathbf{q}'} \left(1+n_{\mathbf{q}''}\right) - \left(1+n_{\mathbf{q}}\right)\left(1+n_{\mathbf{q}'}\right) n_{\mathbf{q}''} \right] S_{\mathbf{q},\mathbf{q}'}^{\mathbf{q}''} + \\ \frac{1}{2}\left[n_{\mathbf{q}} \left(1+n_{\mathbf{q}'}\right)\left(1+n_{\mathbf{q}''}\right) - \left(1+n_{\mathbf{q}}\right) n_{\mathbf{q}'} n_{\mathbf{q}''} \right] S_{\mathbf{q}''}^{\mathbf{q},\mathbf{q}'} \end{array} \right\} \tag{2.35}$$

Here, the first square bracketed term is the probability that a fusion (Eq. (2.26)) phonon collision will occur, while the second square bracketed term is the probability that a fission (Eq. (2.28)) phonon scattering process will occur; the factor of *1/2* appears to prevent double counting. It should be pointed out that in Eq. (2.35) terms $n_{\mathbf{q}}, n_{\mathbf{q}'}$, and $n_{\mathbf{q}''}$ are non-equilibrium distribution functions. The term *S* is the scattering rate for either fusion or fission events and inherently contains information that ensures energy is conserved during scattering processes. The full scattering operator is then the net effect of these two processes together, and is difficult to solve for directly. Recently advances have made it possible to solve the BTE with the full scattering operator in silicon systems [34, 55]. Though these advances are significant, the system geometries are limited to sub-micron sizes due to the computational time needed to calculate individual phonon interactions.

Pomeranchuk used perturbation theory techniques to simplify the term in the braces in Eq. (2.35) according to the conservation laws in Eqs. (2.26), (2.27), (2.28), and (2.29) [56]. The derivation then yields:

$$\left(\frac{\partial n}{\partial t}\right)_{scatter} = \sum_{\mathbf{q}',\mathbf{q}''} D_{\mathbf{q},\mathbf{q}',\mathbf{q}''}\left\{n_{\mathbf{q}} n_{\mathbf{q}'}\left(1+n_{\mathbf{q}''}\right)-\left(1+n_{\mathbf{q}}\right)\left(1+n_{\mathbf{q}'}\right)n_{\mathbf{q}''}\right\} \tag{2.36}$$

Where the coefficients *D* depend on the anharmonicities and will vanish unless energy is conserved; the form of *D* will be presented in Chapter 4 [42]. This form of the scattering operator can be further simplified in the limit of small deviations from equilibrium. The non-equilibrium distribution function can be written as the equilibrium distribution with a perturbation term.

$$n = n^{o} + n' \tag{2.37}$$

The expanded form of the term in braces in Eq. (2.36) is then

$$\left\{\begin{array}{l}\left(n^{o}_{\mathbf{q}}+n'_{\mathbf{q}}\right)\left(n^{o}_{\mathbf{q}'}+n'_{\mathbf{q}'}\right)\left(1+\left(n^{o}_{\mathbf{q}''}+n'_{\mathbf{q}''}\right)\right)- \\ \qquad\left(1+\left(n^{o}_{\mathbf{q}}+n'_{\mathbf{q}}\right)\right)\left(1+\left(n^{o}_{\mathbf{q}'}+n'_{\mathbf{q}'}\right)\right)\left(n^{o}_{\mathbf{q}''}+n'_{\mathbf{q}''}\right)\end{array}\right\} \tag{2.38}$$

In assuming that the single mode relaxation time holds $n'_{\mathbf{q}'} = n'_{\mathbf{q}''} = 0$ (as well as any cross terms that may exist) Eq. (2.23) is recovered and repeated here for clarity.

$$\left(\frac{\partial n}{\partial t}\right)_{scatter} \approx \frac{n^o - n}{\tau} \tag{2.39}$$

While these are drastic simplifications it was found that the second and third interacting phonons do not deviate far from equilibrium even at high temperatures and that the bulk thermal conductivity in silicon can be recovered [34].

2.3.2 Continuity of Energy Density

One of the initial models of phonon transport, based on the BTE was developed into the Equations of Phonon Radiative Transfer (EPRT) [57]. These equations solved explicitly for a phonon intensity variable that could then be correlated back to a temperature as a post-processing step. Since this initial formulation, the energy density form of the BTE has been used extensively [58, 59]. By multiplying the BTE by the function ψ, integrating over all phonon frequencies and summing over all phonon polarizations the energy density moment of the BTE can be derived.

$$\psi = \hbar\omega D(\omega) \tag{2.40}$$

$$\sum_p \int \psi \frac{\partial n}{\partial t} d\omega + \mathbf{v} \cdot \nabla_x \sum_p \int \psi n d\omega = \sum_p \int \psi \frac{n^o - n}{\tau} d\omega \tag{2.41}$$

Defining the phonon energy density as

$$e = \sum_p \int \hbar\omega n D(\omega) d\omega \tag{2.42}$$

The energy density moment then takes the following form.

$$\frac{\partial e}{\partial t} + \mathbf{v} \cdot \nabla_x e = \frac{e^o - e}{\tau} + q''' \tag{2.43}$$

Equation (2.43) is the primary equation being solved in this work; the relaxation time approximation will be utilized for all future simulations. A phonon generation term is added into Eq. (2.43) that represents phonon emission from high-energy electrons. Again, this phonon emission occurs when high energy electrons interact (scatter) with the ion cores of the crystal lattice and produce vibrations (phonons) in the material. Under the adiabatic assumption, electrons can instantaneously respond to motion of the ion cores of a crystal. With this, the two systems (electron and phonon) are effectively de-coupled from each other and the phonon generation rate can be expressed as a constant term in the BTE.

Besides the phonon generation rate, the key phonon parameters needed for Eq. (2.43) are the group velocity and the relaxation time. These properties are needed before any transport simulations are to be performed and can be obtained from the dispersion relationships. The various phonon models will be discussed in the following section.

2.3.3 Phonon Models

There are several levels of detail that can be used to model phonon transport in semiconductor materials. All of the methods fall into two overarching categories, either top-down or bottom-up approaches. In a top-down approach, phonon properties are estimated directly from bulk thermal conductivity values that have usually been found

experimentally. Estimates for the frequency dependence of the relaxation time can be extracted by fitting temperature dependent thermal conductivity values as in [44]. Calculating the phonon relaxation times in this way will guarantee that the correct bulk thermal conductivity will be resolved in large domains. In this category are the gray and the two-fluid (i.e. semi-gray) models, as well as other variants on these two methods. These methods will not capture the details of the phonon dispersion, but are useful for finding limiting cases. As a side effect of extracting phonon properties in this way, a spherical Brillouin zone is usually assumed when performing the integration over all phonon frequencies (Debye approximation). In both the gray and two-fluid phonon models the relaxation time is back calculated from the kinetic theory description of the isotropic thermal conductivity.

$$k = \frac{1}{3} c_v \left|\mathbf{v}\right|^2 \tau \tag{2.44}$$

In the gray model, all phonon modes are assumed to propagate with a single group velocity (linear dispersion relationship). This single group velocity is calculated as the harmonic mean of the LA and TA phonon modes, possibly along several directions in the Brillouin zone. In this way the single group velocity is representative of a directionally averaged quantity. In addition, the effects of optical phonon modes are ignored. The rationale behind this assumption is that the optical phonon modes have a near zero group velocity and therefore do not contribute to the transport of energy; their effect is still included in the specific heat term. If the Debye model is adopted (spherical Brillouin zone) Eq. (2.20) can be simplified to

$$c_v = 9\eta k_b \left(\frac{T}{\theta}\right)^3 \int_0^{\theta/T} \frac{x^4 e^x}{\left(e^x - 1\right)^2} dx \tag{2.45}$$

where η is the number density of oscillators, which can be calculated as the number of atoms in a unit cell divided by the volume of the unit cell and θ is the Debye temperature. It is also possible to use an experimental specific heat instead of Eq. (2.45). Once the group velocity and relaxation time is known, the transport of phonons can be handled with the energy density moment of the BTE. If the Debye approximation is continued the total phonon energy density is defined as

$$e(T) = \frac{9\eta k_b T^4}{\theta} \int_0^{\theta/T} \frac{x^3}{e^x - 1} dx \tag{2.46}$$

Equation (2.46) is also used to define an effective temperature, *T*. The effective temperature is defined as the temperature of an equilibrium system with the same energy as a non-equilibrium system. Using this definition it is possible to convert the spatially dependent energy density solved for with the BTE into a temperature quantity.

To correct the gray model for ignoring optical phonons another top-down model was derived, this model is referred to as the two-fluid or semi-gray model [60, 61]. In this model the spectrum of phonons is broken up into two groups, those that propagate energy (propagating mode) and those that simply store energy (reservoir mode). The two

modes are then representative of rapidly propagating acoustic phonons and slow moving optical phonons. The main equations for this model are shown below.

$$\frac{\partial e_p}{\partial t} + |\mathbf{v}| \nabla e_p = \frac{c_p \left(T_L - T_{ref}\right) - c_p \left(T_p - T_{ref}\right)}{\tau} \tag{2.47}$$

$$\frac{\partial e_r}{\partial t} = \frac{c_p \left(T_L - T_{ref}\right) - c_p \left(T_p - T_{ref}\right)}{\tau} + q''' \tag{2.48}$$

$$e_r = c_r \left(T_r - T_{ref}\right) \tag{2.49}$$

$$T_L = \frac{c_r T_r - c_p T_p}{c_r + c_p} \tag{2.50}$$

As can be seen from Eq. (2.47) the propagating phonon mode is still handled through the solution to the BTE. In this case a lattice temperature, T_L, characterizes the equilibrium phonon energy, which has been defined as the weighted average of the mode temperatures. The non-propagating assumption of the reservoir mode eliminates the need for the advection term on the left hand side of Eq. (2.48). In real devices, electrons will primarily interact with optical phonon modes a generation term is included in Eq. (2.48). It is worth noting that for energy to be conserved the relaxation time must be the same for both the propagating and reservoir modes. In reality, these relaxation times can be very different; however results from this type of model will help establish bounds on the maximum temperature experienced in a device. In a similar manner to the gray model, the relaxation time for the propagating mode is extracted from the kinetic theory definition in Eq. (2.44) with the specific heat of only the propagating phonons included. The specific heat of the two separate modes can be calculated from Eq. (2.20). If the

Debye approximation is used the upper limit in Eq. (2.45) can be modified to reflect the maximum frequency of the acoustic phonons. The optical phonon specific heat can then be estimated through the Einstein model [35].

$$c_v^{optical} = p\eta k_b \frac{\left(\hbar\omega/k_bT\right)^2 e^{\hbar\omega/k_bT}}{\left(e^{\hbar\omega/k_bT}-1\right)^2} \tag{2.51}$$

In Eq. (2.51), p represents the number of optical phonon modes and all other variables have their usual definitions.

The previous phonon dispersion models, in part, rely on the determination of a mode-averaged relaxation time. In the bottom-up approach, phonon properties are calculated directly from the phonon dispersion curves. Phonon group velocities throughout the true Brillouin zone volume can be extracted through Eq. (2.17) for each phonon branch. To calculate the phonon relaxation times from the dispersion curves it is necessary to enforce both crystal momentum conservation as well as energy conservation rules. Expressions developed from perturbation theory have allowed for analytical expressions for the relaxation time to be determined. As discussed in an earlier section the harmonic approximation to the crystal potential is useful for calculating phonon dispersion relationship, but in a purely harmonic crystal phonons will never interact. It is therefore necessary to include the anharmonic contribution to the potential, V_3, as a small perturbation to the harmonic crystal Hamiltonian [62].

$$H = H_{harm} + V_3 \tag{2.52}$$

This method still poses difficulties since the resulting V_3 term is difficult to calculate as it relies on accurate knowledge of third order derivatives of the potential function. A usual approximation made at this point is to assume that the material is an elastic continuum; previous theoretical investigations have made use of this assumption with successes [8, 9, 58, 59]. A low temperature assumption was made by Han and Klemens and a closed form expression for the relaxation time was derived for key types of 3-phonon processes for silicon [63]. With this 3-phonon interaction model it is possible to generate relaxation times that can then be used with a discretized phonon frequency spectrum (frequency bands). An isotropic transport model that incorporates the full phonon dispersion is now possible and has been presented in [58]. Recently an anisotropic model was introduced for silicon systems [64]. It should be noted that the relaxation times implicitly obey energy and crystal momentum conservation rules, whereas in the top-down approaches, no such restriction is enforced. In these models the relaxation times (band-averaged) can be generated prior to the transport simulation and stored in a lookup table. In contrast to the top-down approach, there is no guarantee that the generated relaxation times yield the correct bulk thermal conductivity. Therefore, a check of the relaxation times must be pursued before transport simulations can begin. Using the single mode relaxation time approximation the elements of the thermal conductivity tensor can be expressed as [31].

$$k_{ij} = \sum_{\mathbf{q}s} c_s(\mathbf{q}) \left[\mathbf{v}_s(\mathbf{q}) \cdot \widehat{\nabla T} \right]^2 \tau_s(\mathbf{q}) \tag{2.53}$$

In cubic crystals the phonon group velocity and the temperature difference are parallel to each other and therefore the above tensor is diagonal where the elements are represented by scalars, $k_{ij} = k\delta_{ij}$.

2.4 Solving the Boltzmann Transport Equation

There are several methods available that can be used to solve the Boltzmann transport equations; three methods will be briefly outlined here, Monte Carlo, Finite Volume, and Lattice Boltzmann.

2.4.1 Monte Carlo Methods

Monte Carlo methods are computational algorithms that rely on random sampling of a system to compute the final results. These methods are particularly useful when a closed form solution to the problem at hand exists, as in the case of phonon transport. Their reliance on random sampling makes Monte Carlo methods computationally expensive and therefore domain sizes are typically small. Other complications arise with programming structures, as boundary conditions can be difficult to manage if a flux is present. Additionally, since phonons are bosons there is no conservation law that governs the number of particles in a given system, phonons can be created and destroyed through scattering processes. As a result, any Monte Carlo simulations need to include detailed particle tracking routines, which only adds to the computational complexity. Despite these complications, Monte Carlo methods are valuable in studying transport, especially within complicated domains. Mazumdar *et al.* developed a phonon transport model that included dispersion and polarization [65]. Lacroix *et al.* extended the literature by providing transient simulations of phonon transport in silicon and

germanium structures [66]. Randrianalisoa *et al.* addressed the issue of computer memory handling by proposing a new steady-state Monte Carlo method [67]. Jeng *et al.* studied phonon transport in silicon-germanium nanocomposites by developing complicated simulation domains, however their simulations relied on the gray phonon approximation [68]. Their simulations of thermal conductivity matched well with experimental results that were conducted.

2.4.2 Finite Volume

The analogy between phonon transport and radiation transport (photons) was highlighted when the Equation for Phonon Radiative Transport (EPRT) was introduced [57]. Radiation transport algorithms were developed, particularly implementations of the discrete ordinates method (DOM) and were adopted for use in solving phonon transport problems [66-69]. Several levels of phonon modeling have been incorporated into the DOM method, gray, two-fluid, and isotropic full dispersion successfully [61]. The method has been shown to resolve ballistic as well as diffusive transport. In the isotropic full dispersion model relaxation times were formulated following a low temperature approximation; good agreement with experimental thermal conductivity values for silicon were shown to result. This model assumed a lumped set of optical phonon modes that did not propagate. A simple MOSFET simulation was performed and in comparison with Fourier-based models the finite volume method revealed significant temperature deviations in the hot spot; these deviations were attributed to the effects of optical phonon modes [61]. More recently, dispersive effects of optical phonons were considered and the full form of the scattering operator was included in the transport simulations [34]. Simulations revealed that while the single mode relaxation time approximation is drastic,

in reality the deviations from equilibrium are small. As such, transport models based on this approximation are still valid. The finite volume method was also recently shown to be parallelizable and was modified to include anisotropic relaxation times [55, 64]. Near-ideal speedup values were found using the full scattering model and incorporating a domain decomposition technique (it is also possible to decompose the frequency bands for parallel implementations) [55].

The current finite volume models available represent one of the most complete pictures of phonon transport. While valuable for elucidating trends in the basic physics of phonon transport, the computational load prohibits the simulation of realistic devices.

2.4.3 Lattice Boltzmann Method

The Lattice Boltzmann (LB) method is similar to the development of the discrete ordinates method, and has seen the most development in the area of fluid mechanics [69, 70]. Recently, however, several simulations of phonon transport were conducted using the LB method. The primary difference between the LB method and the finite volume method described previously is the angular discretization of the propagating phonons. Depending on the method used, phonons are allowed to propagate in either 4 or 8 directions to the next lattice site. This discretization scheme sacrifices angular resolution, and is therefore expected to yield inaccurate solutions when ballistic transport dominates. In transitional and diffusive domains the LB method has been shown to resolve transport accurately. The advantages of the LB method over others are its relatively straightforward program structure, potential for parallelization, and the potential for multiscale simulations to be developed. The multiscale development is developed in the

following chapter. The LB method is also able to handle arbitrary boundaries since boundary conditions are applied locally (per node) instead of along an entire edge.

Recently, the energy density moment of the BTE was discretized within the framework of the LB method and used to study the temperature distributions within a microelectronic device [71, 72]. The LB method was also used to study the heat flow through a nanostructure referred to as a nanoduct to study phonon transport in a bend [73]. Ghai *et al.* also implemented the LB to study the effects of a nanoscale hot spot in multilayered films as well as to study a simple coupled electron-phonon system [74, 75]. The method was also developed in order to include dispersion effects in silicon electronic devices [76, 77].

The simulations described above have all been performed on a regular LB grid (equal nodal spacing in all directions). This formulation limits the geometries that can be discretized, and while interpolation schemes have been developed to handle curved boundaries more recent efforts have been applied to the development of unstructured grid formulations [78-82]. The unstructured grid offers flexibility in meshing, but still adopts the discrete propagation directions implemented in the regular grid formulation. For this study the regular grid formulation is used.

CHAPTER 3

THEORY OF THE LATTICE BOLTZMANN METHOD

This chapter begins by outlining some of the basic theory for the Lattice Boltzmann method. The BTE discretization scheme is discussed as well as different lattice types used within the LB method. For each of these lattice types the necessary symmetry conditions are discussed and boundary conditions are developed. Test cases are presented to test for numerical accuracy and errors in the method are discussed. Next the multiscale coupling will be presented through application of the Chapman-Enskog expansion and errors at the coupling interface will be quantified.

3.1 Boltzmann Transport Equation Discretization

As presented in the previous chapter the Boltzmann transport equation can be written in the following form, assuming the relaxation time approximation for the collision operator.

$$\frac{\partial n}{\partial t} + \mathbf{v} \cdot \nabla_x n = \frac{n^o - n}{\tau} \tag{3.1}$$

This equation is formulated to account for transport in any direction **v**. To solve this equation with the LB method, the velocity space must first be discretized [83, 84]. This amounts to projecting the distribution function in discrete directions that describe paths that particles are allowed to travel. The discrete form of the BTE can then be written as

$$\frac{\partial n_i}{\partial t} + \mathbf{v}_i \nabla_x n_i = \frac{n_i^o - n_i}{\tau} \tag{3.2}$$

where *i* is a direction subscript and other variables have their usual definitions. With the velocity space now discretized it is possible to deal with the gradient operator as well as the time derivative. By approximating each term with a first order Taylor expansion (assuming a 2D domain) the discrete form is found.

$$\begin{aligned} &\frac{n_i(x,t+\Delta t) - n_i(x,t)}{\Delta t} + (\mathbf{v}_i \cdot \hat{x}) \frac{n_i(x+\Delta x,t+\Delta t) - n_i(x,t)}{\Delta x} + \\ &(\mathbf{v}_i \cdot \hat{y}) \frac{n_i(y+\Delta y,t+\Delta t) - n_i(y,t)}{\Delta y} = \frac{n_i^o - n_i}{\tau} \end{aligned} \tag{3.3}$$

By making the simplifying assumption $\Delta x = \Delta y$ and by linking the nodal spacing to the time step by setting $\Delta x = v\Delta t$ the so called Lattice Boltzmann Kinetic Equation (LBKE) found. The energy density form of the LBKE is given in Eq. (3.4)

$$e_i(x+\Delta x,t+\Delta t) = (1-\Gamma_i) e_i(x,t) + \Gamma_i e_i^o(x,t) \tag{3.4}$$

The term e_i is called the "directional non-equilibrium phonon energy", or simply the "directional phonon energy". The directional equilibrium energy is referred to as e_i^o. A phonon scattering weight is also introduced through the Γ_i term as the ratio of the time step to the relaxation time ($\Gamma_i = (\Delta x / \mathbf{v}_i)/\tau$). In essence this term governs the fraction of phonons that arrive at the new lattice site in an equilibrium energy state. If $\Gamma \sim 1$ then

more equilibrium state phonons arrive at the next site, where as if $\Gamma<1$ more non-equilibrium phonons will arrive. The LBKE has a simple physical analogue that can provide some valuable insight in to the application of LB method. Typically the LB method is described as a "stream and collide" method. When a computational domain is defined particles are assumed to exist in cells at their center node location. These particles are allowed to propagate to the nearest neighboring nodes; this is the "streaming" step of the method. Upon arrival at the next lattice site the incoming particles are allowed to collide with other incoming particles (from other directions). The equilibrium distribution is found by averaging all of the incoming non-equilibrium distribution functions. This process is then repeated for the necessary simulation time.

There are a few properties of the LBKE that must be pointed out before going into the details of the lattice types. First is that in the present form the LBKE is an explicit equation, which makes it subject to convergence criteria. Stability requirements restricts $\Gamma < 1$; another way of thinking about this is that the time step, Δt, must be smaller than the phonon relaxation time. However, an explicit equation allows the incorporation of more advanced phonon physics to be made without much modification to the procedure used to solve the BTE. This added flexibility is certainly valuable and will be exploited when coupling a finite difference mesh to the LB lattice and will be discussed in a later section.

3.2 Lattice Types

While there are several choices for LB lattices, two of the most common are shown in Figure 9. Lattice types are labeled following the D*d*Q*n* convention, where *d* is the dimensionality of the domain and *n* is the number of discrete velocities per node.

Both a D2Q4 lattice and a D2Q9 (2 dimensions, 9 velocities) lattice are shown in Figure 9. It is traditional notation to use the "D2Q9" label even though the ninth velocity at the center node is set to zero due to the zero phonon group velocity at that location [73]. It is also possible to generate hexagonal lattices. This particular shape is useful when domains with hexagonal symmetry are used, or if the underlying crystal structure of the material is hexagonal. This particular lattice shape will not be used in this study; instead the focus will be on the D2Q4 and D2Q9 lattices. Whichever lattice is used, there are symmetry conditions that must be met in order to satisfy conservation of energy.

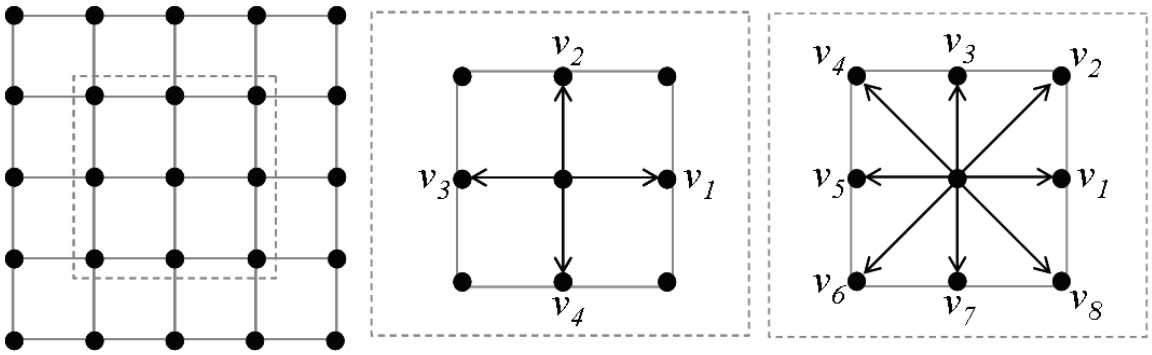

Figure 9: A regular LB lattice discretization of a domain is shown on the left with a unit cell outlined. The details of the velocity discretization scheme are shown in the other images. The middle image illustrates a D2Q4 velocity discretization and on the far right the D2Q9 scheme is shown.

Before discussing the symmetry conditions that must be satisfied by each cell in the LB simulation, it is necessary to define both the total equilibrium energy, as well as the directional equilibrium energy. The total equilibrium energy that appears in the LBKE is calculated by the sum of all directional non-equilibrium phonon energy propagations in the lattice. In the D2Q9 lattice shown in Figure 9, n, would run from 1 to 8.

$$e^o(x,t) = \sum_n e_i(x,t) \tag{3.5}$$

In addition, the directional equilibrium phonon energy is defined as the weighted total equilibrium phonon energy, represented as Eq. (3.8). The weighting coefficients are subject to the lattice symmetry requirements defined in the following equations.

$$\sum_n \mathbf{v}_i \cdot \left(w_i e_i^o\right) = 0 \tag{3.6}$$

$$\sum_n w_i = 1 \tag{3.7}$$

These requirements guarantee energy conservation, however the choice of the weighting coefficients is not unique. By introducing different weights it is possible to force phonons to scatter into preferred directions. This is an important consideration when developing boundary conditions, and will be discussed in the next section. As a quick example, if it is assumed that phonons can scatter into any direction with equal probability, all weighting coefficients have a value of 1/8.

$$e_i^o(x,t) = w_i e^o(x,t) \tag{3.8}$$

Given these definitions the time evolution of the phonon energy can be summarized in Figure 10.

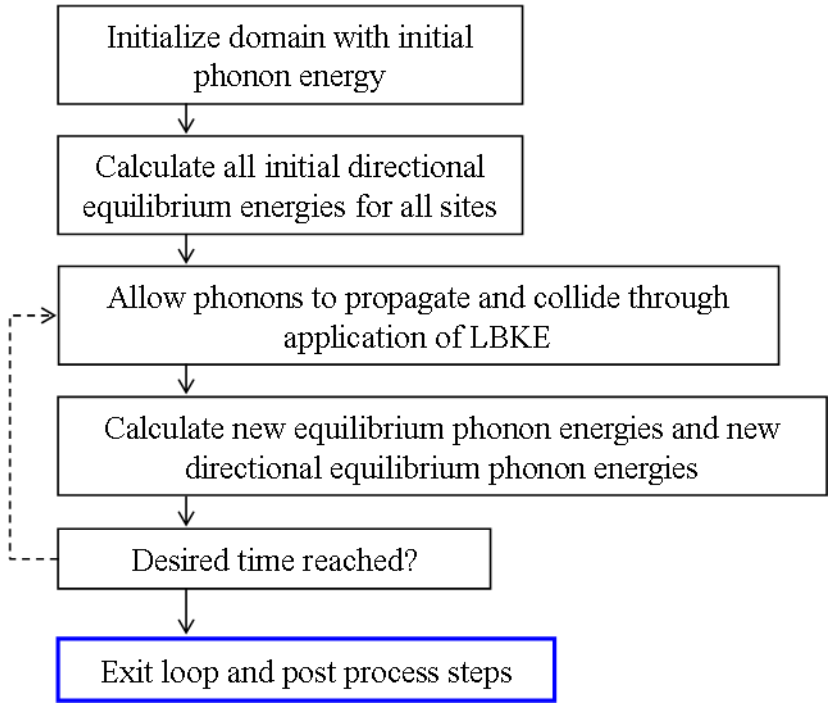

Figure 10: LBM time evolution flow chart.

The evolution caused by the LBKE can also be summarized pictorially as shown on the simplified D2Q4 lattice in Figure 11.

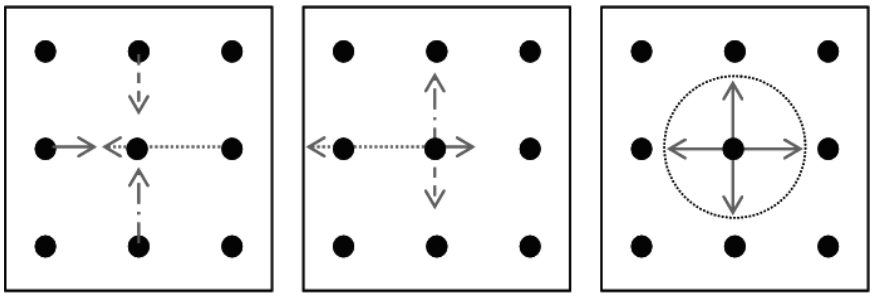

Figure 11: The representation of the propagation and collision step administered by the LBKE Eq. (3.4) is shown in on a simplified D2Q4 lattice for clarity. Step 1 shows the directional phonon energy (the magnitude is represented by the arrow length) at time t. Step 2 shows how the phonons have propagated to time $t+\Delta t$. In step 3 the new directional equilibrium phonon energies have been calculated from Eq. (3.8).

3.3 Boundary Conditions

As with computational models based on traditional partial differential equations the application of accurate boundary conditions dictates most of the success of the model; LB simulations are no different in this regard. Additional complexities arise when specifying boundary conditions for the LB models as the boundary nodes must capture the proper particle distribution functions that are often associated with a macroscopic quantity (i.e. temperature or surface heat flux). Since only one macroscopic quantity is known, several of the directional distribution functions need to be determined that then simulate accurate microscopic phenomena. This problem can be seen pictorially with a D2Q9 lattice in Figure 12.

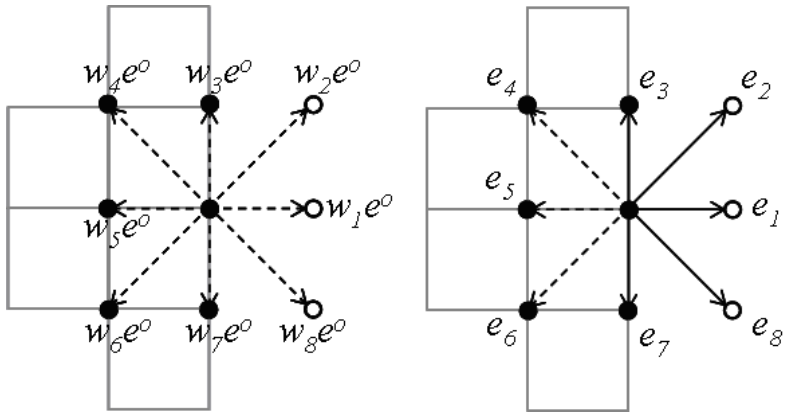

Figure 12: Dirichlet boundary node (left) and a Neumann boundary node (right) for the LB domain. The missing particle distribution functions (dashed arrows) in each case will be found from the application of the boundary condition. The other distribution functions (solid arrows) are found directly from the application of Eq. (3.4).

It is possible for the LB method to properly handle both Dirichlet and Neumann boundary conditions. To specify a temperature at a boundary (Dirichlet type) Eq. (2.46) can used to calculate the corresponding phonon energy density. The phonon energy density is then

divided into the proper directional non-equilibrium phonon energies and held constant for all time as shown in the left cartoon in Figure 12. This way all directional distribution functions can be solved for knowing only the temperature at the boundary node. To apply a Neumann boundary condition the heat flux vector across a node must first be defined.

$$\vec{q} = \sum_{n} \mathbf{v}_i e_i \left(x, t \right) \tag{3.9}$$

In Eq. (3.9), $\mathbf{v}_i$ is the phonon group velocity vector in the *i* lattice direction. To specify a value of the surface heat flux, the missing distribution functions in Figure 12 can be solved for through Eq. (3.9) and knowledge of the incoming heat flux vector; for an adiabatic boundary, $\vec{q} \cdot \hat{n} = 0$. By definition, an adiabatic boundary results in the non-equilibrium phonons reflecting off the boundary. This process of reflecting phonons can occur in several ways; the mode of reflection is a function of the phonon wavelength, λ, and the surface roughness, σ. If the phonon wavelength is much smaller than the surface roughness ($\lambda \gg \sigma$) then the phonons behave as if the boundary is perfectly smooth and reflection is specular in nature. In the contrary case ($\lambda \ll \sigma$), the impinging phonons will reflect diffusely [29]. Intermediate cases can arise where $\lambda \approx \sigma$ in which case there is some fraction of phonons that is reflected specularly and another fraction reflected diffusely.

3.4 Test Cases

Before presenting the LB/FD coupling methodology it is important to continue the verification processes to show that the LB technique is adequate at describing the micro and macroscopic diffusion of heat. In order to investigate the effect that the boundaries have on the effective thermal conductivity a test domain was created as shown in Figure 13.

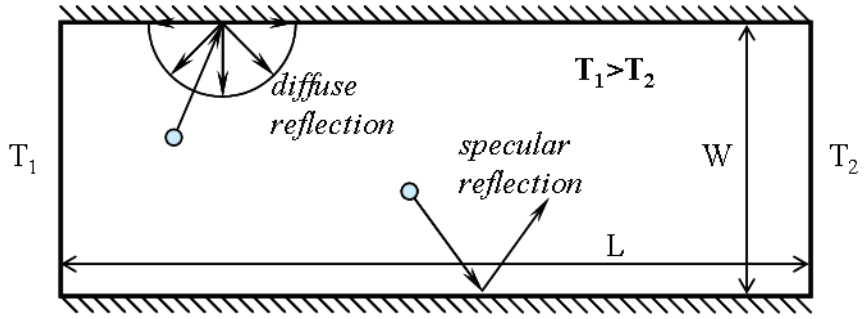

Figure 13: Test problem for determining the effect that the boundary conditions have on the effective thermal conductivity. In all simulations the dimension $L \gg \Lambda$, where Λ is the mean free path of the phonon.

While a boundary can be specified as adiabatic, there is some flexibility in choosing the boundary reflection mode (diffuse, specular). In Figure 14 the boundary conditions are given explicitly.

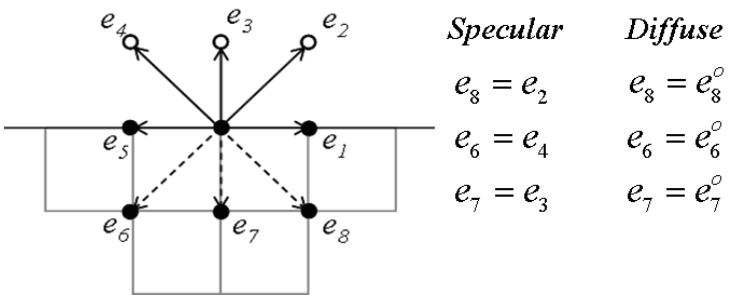

Figure 14: Adiabatic boundary conditions for specular and diffuse reflection.

The formulation given here is similar to the "bounce-back" boundary presented by Zou and He for the specular reflection case [85]. However, there is a difference for the purely diffuse case. It is assumed that when a phonon encounters the boundary it will relax into an equilibrium state. This boundary condition is directly analogous to a velocity slip boundary that is observed in the free molecular flow regime in fluid flow problems. All of the missing directional distribution functions here can be solved for through application of the boundary condition and are functions of local variables only. Local variables are those that are associated with a particular node. Non-local boundary conditions rely on an auxiliary lattice outside of the physical domain. This local treatment of the boundary is possible by placing a lattice node directly on the physical boundary. Jiaung *et a.* placed a lattice node $\Delta x/2$ off the physical boundary and therefore needed to develop a more complicated boundary condition expression that was then non-local in nature [73]. Simulation results of the test domain for perfectly specular and perfectly diffuse boundaries are shown in Figure 15. Solutions developed by Flik and Tellier that assume diffuse boundary scattering are also presented for comparison; good agreement can be seen over a range of Knudsen numbers for the local boundary conditions presented in this work [86, 87]. As expected, there is no observed drop in the

thermal conductivity with specular boundaries due to perfect phonon reflection. These series of simulations confirms proper application of microscopic boundary conditions.

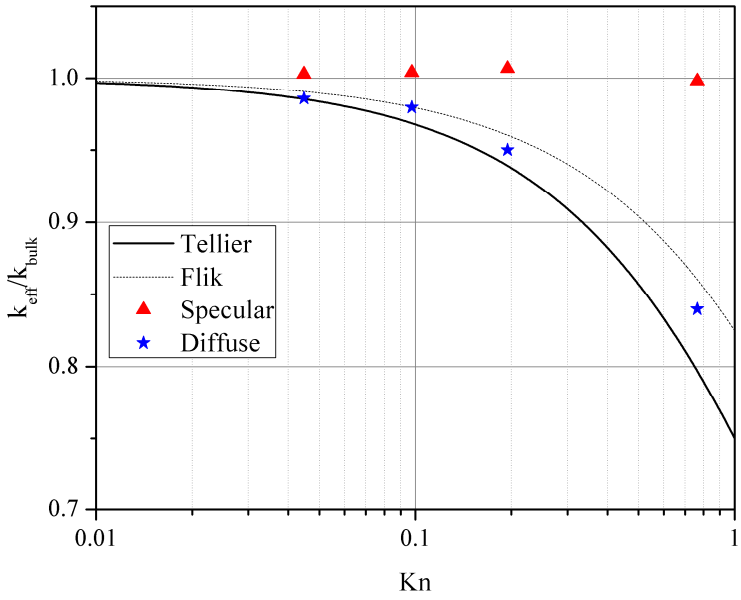

Figure 15: The effect of boundary conditions on the thermal conductivity of a thin film. Flik [86]. Tellier [87].

To study the macroscopic behavior of the LB method and quantify the errors in the technique a large (Kn=0.0082) square domain was simulated using a phonon group velocity of 6400 ms^{-1} and a relaxation time of 6.438 ps (gray model); these properties were calculated by assuming a thermal conductivity of 148 $Wm^{-1}K^{-1}$ for silicon and using the kinetic theory definition of the thermal conductivity. Three of the boundaries were held at a constant 300 K while a heat flux was applied to the fourth boundary. The results of these simulations were compared to an analytical solution. The analytical solution for the square domain in Figure 16 is presented.

$$T(x,y)=\sum_{m=1}^{\infty}\frac{2q''a}{m^2\pi^2k}\left[1-\cos(m\pi)\right]\operatorname{sech}\left(\frac{bm\pi}{a}\right)\sin\left(\frac{m\pi}{a}x\right)\sinh\left(\frac{m\pi}{a}y\right) \qquad (3.10)$$

To further test the LB method an L-shaped domain was simulated in order to resolve the more complicated heat flux patterns that result. This specific domain was designed in order to test the quality of the D2Q9 lattice structure. Both domains and their boundary conditions are shown in Figure 16. For the L-shaped domain a converged finite element solution was used for comparison purposes. As all sides of this domain were adiabatic, phonons must be able to travel through the corner accurately. In this example the behavior of the phonons must converge to what is expected from a diffusive simulation. It is also possible to perform this simulation with a D2Q4 lattice, even though the dominant heat flux vectors through the corner region are aligned along a diagonal. While phonons on a D2Q4 lattice will flow through the corner on a stair-stepped path, the average effect of this is small since the total number of mesh points is very large. It is expected that as the domain size decreases and the ballistic regime is approached, the D2Q4 lattice will begin to show erroneous results where as the D2Q9 lattice will be more robust. Additionally, as the domain size decreases, the effects of boundary scattering begin to dominate. Nanoscale heat flow patterns through complicated domains (i.e. those with non-uniform cross-section) results in the effective thermal conductivity being position dependent as can be seen in [72].

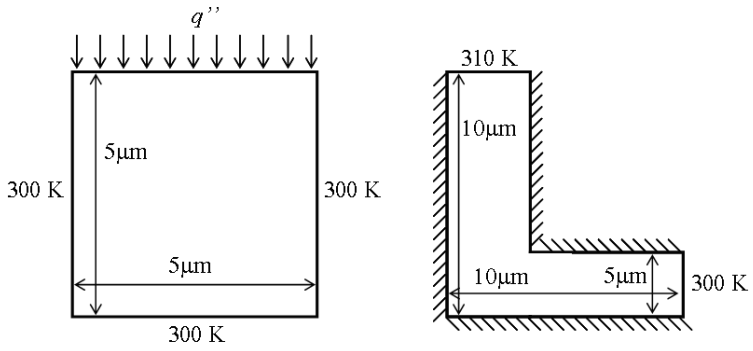

Figure 16: Simulation domains for testing the LB method.

In the first set of simulations the temperature along the top surface (x-direction) and through the middle (y-direction) was calculated for the square domain shown in Figure 17. The analytical temperature distribution in this particular domain was determined through a standard separation of variables method. The results of the LB simulation were plotted against the analytical solution as shown in the Figure 17.

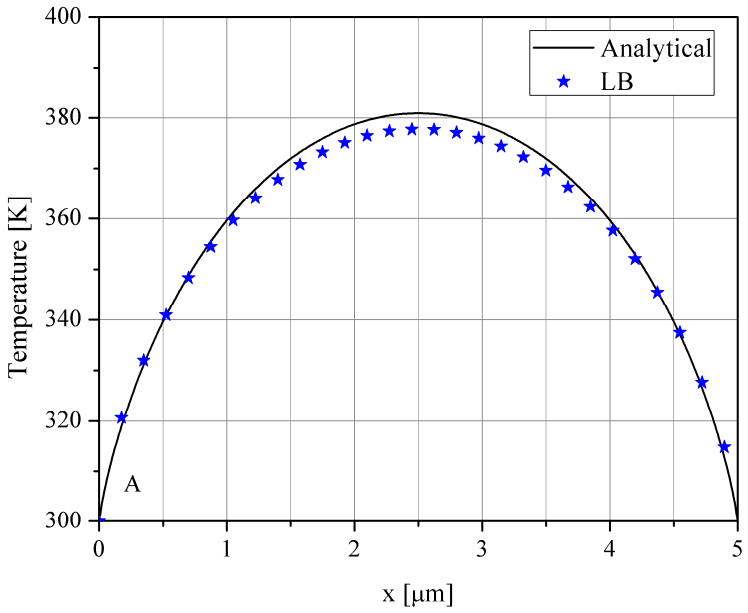

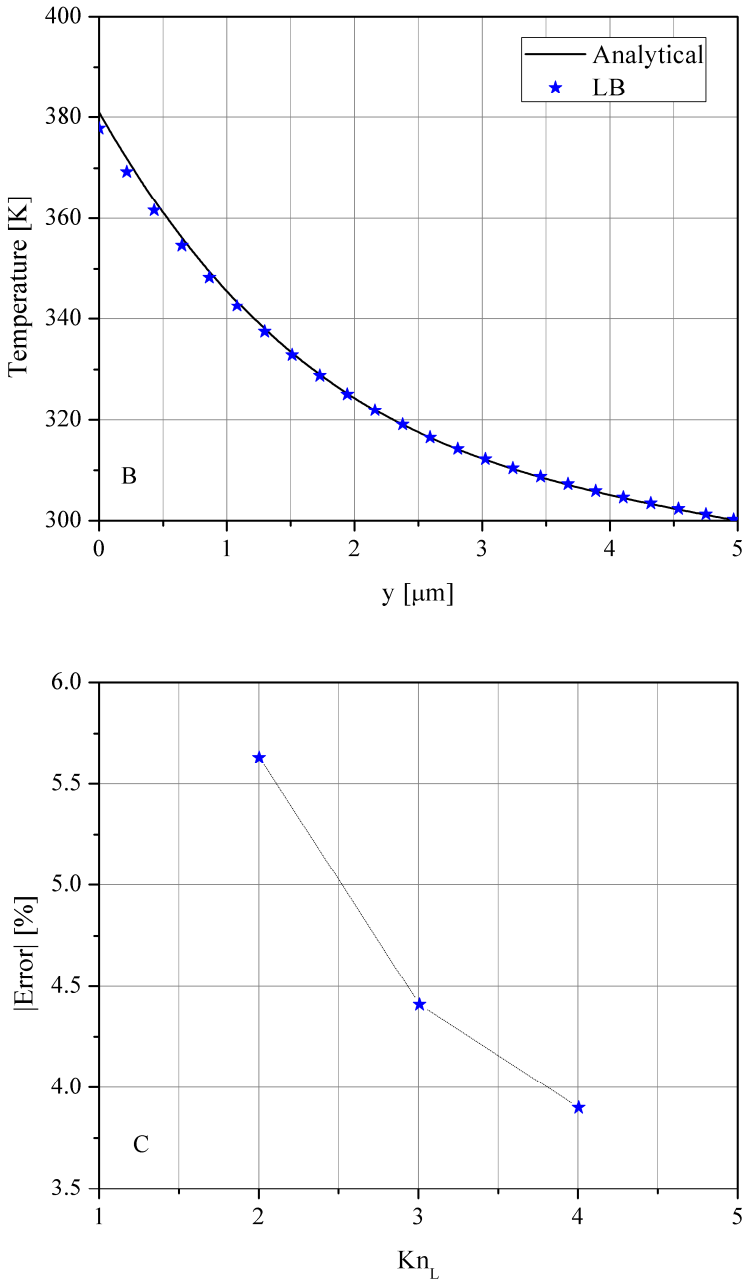

Figure 17: (A & B) Absolute temperature contours from both the LB simulations and the analytical solution. (C) Error introduced by the discrete nature of the LB method. The lattice Knudsen number is defined as $Kn_L = \Lambda / L$.

While the results show good agreement, there is still some discrepancy in the maximum temperature. Errors of this kind are caused by the discrete nature of the LB method. In order to reduce the error in the maximum temperature a smaller lattice spacing is needed.

The effect of refining the lattice can be seen in Figure 17. The L-shaped domain was simulated next in order to resolve any errors that may be a result of the bent geometry. Again, all critical dimensions in this geometry were sized to be diffusive in nature. The results presented show the absolute temperature along the length of the centerline.

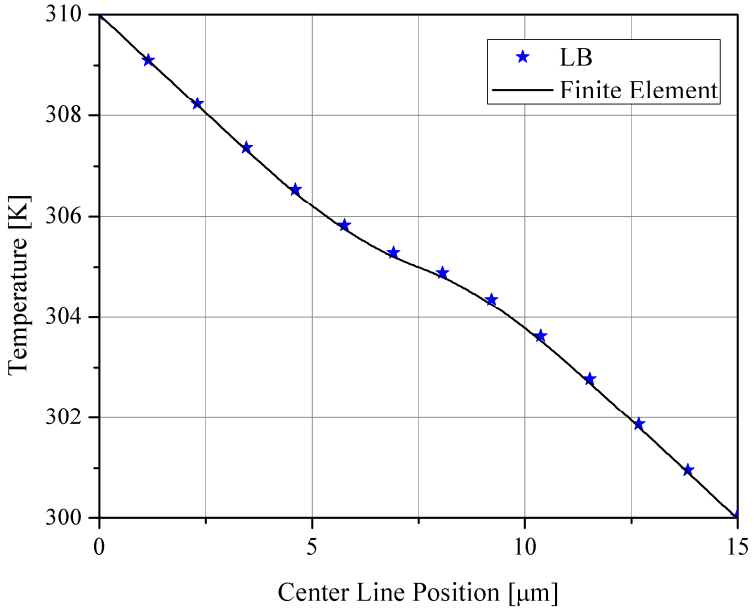

Figure 18: Centerline temperature distribution in the L-shaped domain.

It can be seen in Figure 18 that there is good agreement between the finite element simulation and the LB simulation at the edges of the domain; agreement continues in the vicinity of the corner region where the temperature distribution is non-linear.

One last test of the LB method was performed in order to study the transient behavior of a 1D system. The simulation domain was a 300 μm thick piece of silicon with the left boundary held at a constant 310 K while the right boundary was held at a constant 300 K. The transient response is shown in Figure 19. Good agreement was observed when compared to the analytical solution through several points in time.

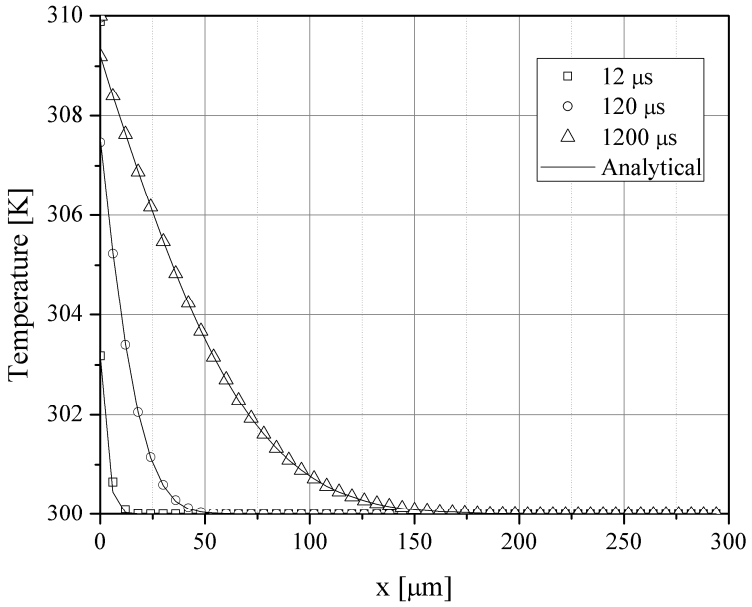

Figure 19: 1D transient temperature evolution with LB and compared to the analytical solution.

By combining the results of the diffusive simulations along with the results of the thermal conductivity reduction in thin films it can be stated that the LB method is adequate for describing phonon transport in a range of transport regimes and geometrical complexities. With this information it is now possible to proceed with the multiscale LB methodology.

3.5 Multiscale Lattice Boltzmann

While the application of LB boundary conditions is relatively straightforward it would be desirable to couple the LB method with a finite difference (FD) solver. As mentioned earlier, there are computational benefits to approach micro/nano-scale heat transfer problems from a multiscale point of view. Methods for coupling the LB method with a FD solver have been developed that allow larger domains to be solved as can be seen in Figure 20.

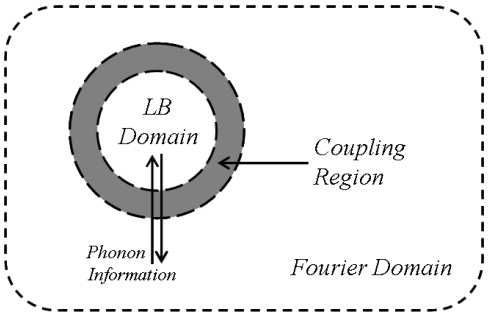

Figure 20: Conceptual domain decomposition into the Lattice Boltzmann region and the Fourier region. The handshaking region allows for phonon information to pass between the two domains.

As with traditional LB boundary conditions the key component to coupling LB and FD is to solve for the missing distribution functions that appear at the LB/FD interface. This was see in applying the Dirichlet and Neumann boundary conditions in Figure 12. Phonon information flowing out of the LB sub-domain in the form of a heat flux upon the Fourier domain and is calculated through Eq. (3.9). The missing distribution functions pointing from the Fourier domain into the LB sub-domain must then be solved for in order to ensure that phonons can travel back and forth with minimal loss of information. To aid in coupling the LB and FD domains the relationship between the microscopic distribution functions of the BTE to macroscopic parameters used in the FD domain must be found. This can be accomplished by approximating the left-hand side of Eq. (3.4) with a second order Taylor expansion about $e_i(x,t)$.

$$e_i(x+\Delta x, t+\Delta t) \approx$$
$$e_i + v_i\Delta t\frac{\partial e_i}{\partial x} + \Delta t\frac{\partial e_i}{\partial t} + \frac{1}{2!}\left[(v_i\Delta t)^2\frac{\partial^2 e_i}{\partial x^2} + 2\left(v_i\Delta t^2\right)\frac{\partial^2 e_i}{\partial x\partial t} + \Delta t^2\frac{\partial^2 e_i}{\partial t^2}\right] + \ldots \quad (3.11)$$

In order to separate out the relevant transport scales the Chapman-Enskog expansion method is utilized. In this method the directional phonon energy is expanded in a power series with the form found in the following equation.

$$e_i = \sum_n \varepsilon^n e_i^n \tag{3.12}$$

Here the term, ε, is considered to be a "smallness" parameter; this parameter also can be referred to as the Knudsen number. Before employing the above expansion method, the proper scaling of the partial derivatives in Eq. (3.11) must be determined. In order to recover the Navier-Stokes equations Frisch *et al.* suggested the following scaling [88].

$$\frac{\partial}{\partial t} \to \varepsilon^2 \frac{\partial}{\partial t} \tag{3.13}$$

$$\frac{\partial}{\partial x} \to \varepsilon \frac{\partial}{\partial x} \tag{3.14}$$

The same scaling will be applied here in order to recover diffusive behavior on large spatial scales. Equations (3.13) and (3.14) effectively suggest that diffusion is a slow process overall. This follows an intuitive argument that in a simple 1D system the steady state behavior varies as a linear function of the position variable; where the transient response follows an exponential dependence. The "slower" process with time is reflected in the scaling as a second order process, ε^2. To find asymptotic solutions Eq. (3.12) is

substituted into the LBKE. In noting the proper scaling of the derivative terms the following expanded form is obtained, keeping only first and second powers of ε.

$$\begin{aligned}\varepsilon v_i \Delta t \frac{\partial}{\partial x}\left(e_i^{(0)} + \varepsilon e_i^{(1)} + \varepsilon^2 e_i^{(2)}\right) + \varepsilon^2 \Delta t \frac{\partial}{\partial t}\left(e_i^{(0)} + \varepsilon e_i^{(1)} + \varepsilon^2 e_i^{(2)}\right) + \\ \varepsilon^2 \frac{\left(v_i \Delta t\right)^2}{2} \frac{\partial^2}{\partial x^2}\left(e_i^{(0)} + \varepsilon e_i^{(1)} + \varepsilon^2 e_i^{(2)}\right) = \Gamma_i \left(e_i^{(0)} + \varepsilon e_i^{(1)} + \varepsilon^2 e_i^{(2)} - e_i^o\right)\end{aligned} \tag{3.15}$$

Here the notation of $e_i^{(n)}$ is simply used as a labeling convection for an *n* order process. It is now possible to drop all terms in ε^2. If this first order assumption is made the following results are found.

$$e_i^{(0)} = e_i^o \tag{3.16}$$

$$e_i^{(1)} = -v_i \tau \frac{\partial e^o}{\partial x} \tag{3.17}$$

For completeness the second order terms were found, however it was not used in the simulations due to its more complicated form.

$$e_i^{(2)} = -v_i^2 \frac{\Delta t \tau}{2d} \frac{\partial^2 e^o}{\partial x^2} + \frac{\Delta t}{2d} \frac{\partial e^o}{\partial t} - v_i^3 \frac{\Delta t^2 \tau}{4d} \frac{\partial^3 e^o}{\partial x^3} \tag{3.18}$$

This methodology now serves as the link between microscopic and macroscopic variables. As a result of this expansion it can be shown that the total non-equilibrium

distribution function can be divided into an equilibrium component and a first order correction term (the non-equilibrium component).

$$e_i = e_i^o - v_i \tau \frac{\partial e^o}{\partial x} \tag{3.19}$$

With Eq. (3.19) it is now possible to solve for the total phonon energy leaving the Fourier domain and entering the LB sub-domain. The first term on the right-hand side is the equilibrium energy of the coupled nodes corrected by the gradient of the equilibrium energy across the interface. In practice this gradient can be easily approximated by a second order finite difference method [89].

With traditional finite difference schemes non-uniform node spacing can be handled with relative ease. This is not the case when coupling with the LB method. The nodal spacing requirements for the LB domain are based on the physics of the phonons studied and the LB time step. The grid that is generated is therefore uniformly spaced in all dimensions. If a FD model is to be effective it is desirable that the grid be able to expand in space away from the LB sub-domain in all dimensions independently. Henio took a sub-grid method approach in order to couple the LB and FD domains together [90]. While sub-grid methods offer some advantages, the necessary intermediate interpolation steps are undesirable as they could introduce additional errors. Therefore the approach taken in this work was to couple a single layer of overlapping nodes. The grid expansion scheme shown in Figure 21 allows a macroscopic domain to be modeled, bypassing excessive computational investments.

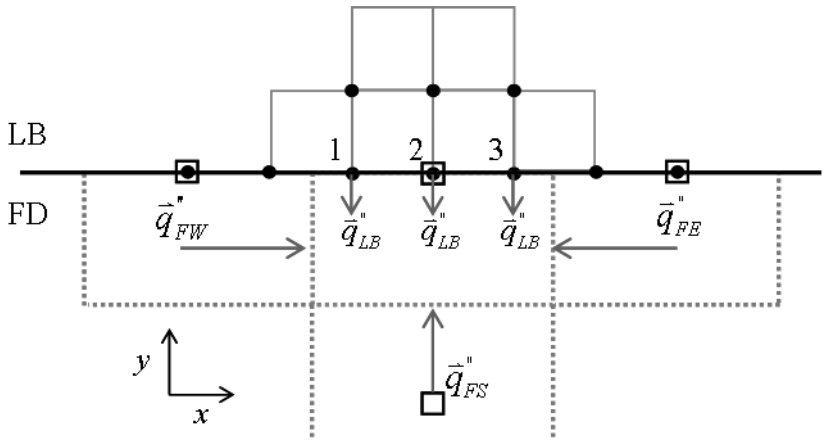

Figure 21: Grid expansion procedure in two dimensions, here the ratio of expansion is 3:1. LB nodes are represented by ●, while FD nodes are represented by □. Fourier based heat fluxes travel into the interface node through the western, southern and eastern directions. The total heat flux from the LB side is the sum of many individual heat flux values.

Energy is allowed to propagate in the FD region through the use of the thermal conductivity. At the interface the total heat flux from the LB region takes the form of absorbed phonons and is the sum of several individual heat flux values. Thermal information is allowed to travel from the Fourier region to the LB region. Care must be taken that the expansion method, in this form, is of sufficient resolution to accurately capture the energy flow across the entire interface. It is now possible to apply an energy balance to the control volume around the interface node and derive the implicit representation of the transient temperature response across a perfect interface. The resulting energy balance leads to a matrix problem of the form:

$$\mathbf{A}\mathbf{T}^{t+1} = \mathbf{T}^{t} + \mathbf{Q} \tag{3.20}$$

Here **A** is a matrix of thermal coefficients and **Q** is a column vector that includes the incident heat flux information from the coupled LB nodes. Once in matrix form direct inversion or Gauss-elimination techniques can be used to solve the system. Other variations of the implicit method can be developed based on the Crank-Nicolson (CN) method. The CN method results in equations that are second order accurate in the spatial variables.

3.6 Numerical Errors

In this study two test problems were defined, their domains and boundary conditions are outlined in Figure 22. In both cases the relaxation time (6.438 ps) was calculated from the bulk silicon thermal conductivity ($148 Wm^{-1}K^{-1}$) by using the common kinetic theory definition. The averaged phonon group velocity was taken to be $6400 ms^{-1}$, which then leads to an effective mean free path of 41 nm.

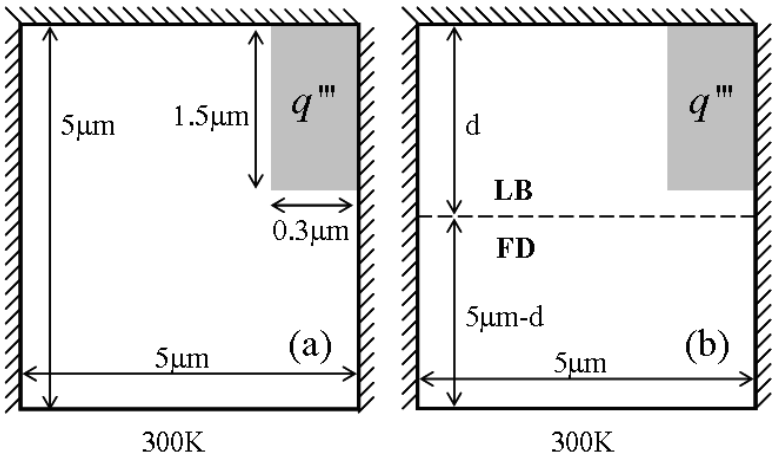

Figure 22: Test problems for the error analysis. The figure on the left contains only the LB lattice while the problem on the right contains the coupled LB/FD solution. In both cases $q''' = 1.875 \times 10^{15} W/m^3$.

While there can be many sources of error in numerical methods, the four main sources of error in the LB method are due to:

1. Discretized lattice directions for phonon propagation
2. Lattice spacing (Δx)
3. Information loss at the LB/FD interface
4. Transport regime considerations

The first two error sources have parallels in traditional FD as well at finite element (FE) methods and are easily understood. The third source of error arises from approximations made during the Chapman-Enskog expansion of the LBKE. The fourth source of error can be introduced if the dimensions of the domain are not large enough for that domain (or sub-domain) to be considered sufficiently diffusive. Problem (a) in Figure 22 was used to quantify the first two types of errors and the thickness of the LB region was varied in problem (b) to quantify the third and forth types of error. All solutions were found to be at steady state after convergence in the heat fluxes and the temperatures was observed. A traditional FE model was developed and solved to act as a comparison against each of these test cases; the results are shown in Figure 23.

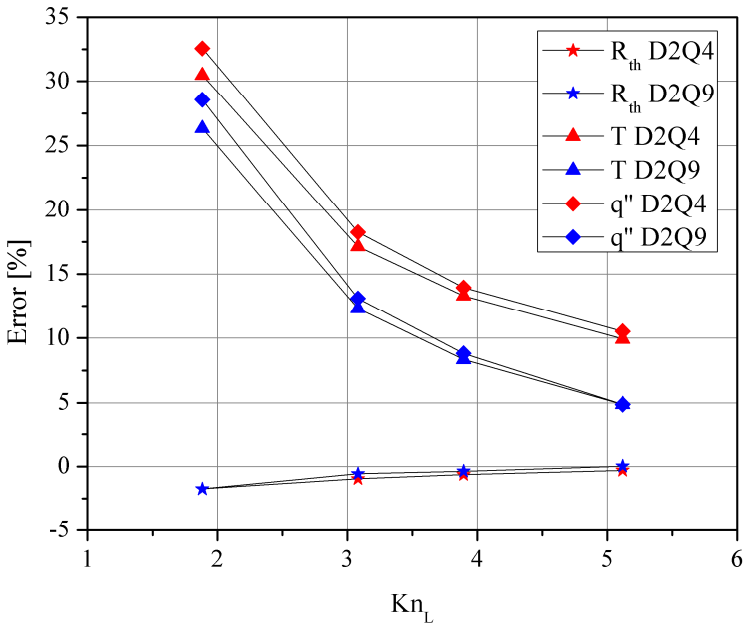

Figure 23: Error introduced as a result of the LB lattice type as well as the lattice spacing for maximum temperature, heat flux, and thermal resistance.

The results of the error analysis show a significant drop in the absolute error for both the maximum temperature and the heat flux as more phonon propagation directions are considered. The thermal resistance (units of KW^{-1}) reported here is defined as the ratio of the maximum temperature difference to the heat generated and is not sensitive to the lattice type. The absolute errors can also be significantly reduced by decreasing the lattice spacing. Figure 23 is plotted as a function of the lattice Knudsen number, the ratio of the mean free path to the lattice spacing; this quantity can be taken as a measure of how ballistic the transport is from lattice site to lattice site. In reality, purely ballistic transport is not obtainable due to the large computational expense and instead must be approximated. As $Kn_L > 5$, ballistic phonon transport dominates and the accuracy of the solution increases. To quantify the third and fourth types of error, test problem (b) was solved for a LB region that had a variable thickness, *d*. For these cases the reference

solution was taken to be a LB-only model using the D2Q9 lattice with the same Kn_L and dimensions. The FD region was discretized with the same Δx on the LB domain. While this is not computationally efficient, it allows for the isolation of the interface effects. The results are presented in Figure 24.

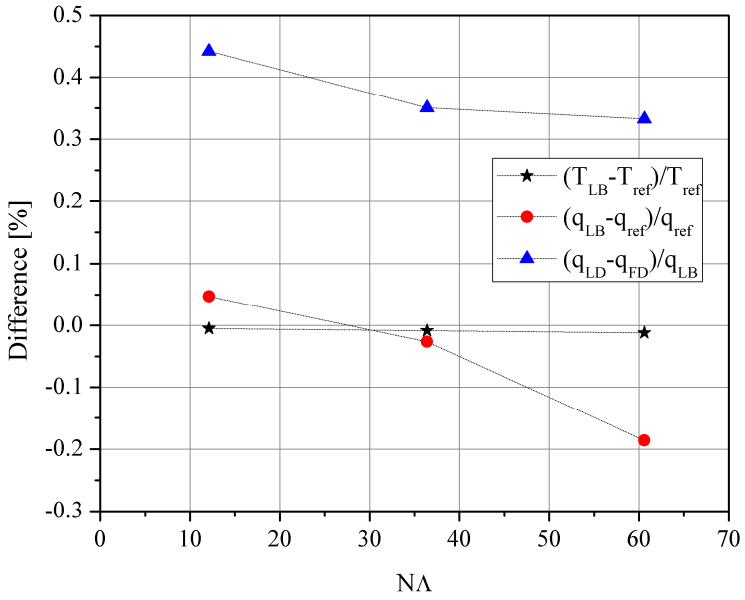

Figure 24: Errors introduced by the position of the coupling interface. Here NΛ is the number of mean free paths the coupling interface is located away from the nearest phonon generation cell.

The third type of error introduced earlier was that caused by the actual coupling methodology. Ideally, phonon information should be able to pass through the interface in both directions without loss. This is analogous to having a continuous heat flux at the interface of two diffusive domains. From the moving boundary experiment it can be seen that interface distances as small as 10Λ introduce <0.5% error from the expected values. To address the fourth type of error the maximum temperature and total heat flow were compared to the reference case. Again, from Figure 24 the interface did not cause any significant effect on the solution; errors on the order of <0.1% were found at distances of

10Λ. These findings are critical for reducing the size of the LB domain in order to minimize the computational investment all while keeping accuracy high. It was mentioned that the expansion scheme proposed here must be of sufficient resolution to retain accuracy in the solution. To test the expansion method the problem (b) from Figure 22 was solved while varying the number of LB nodes that were coupled to one FD node. A 1:1 coupling ratio was chosen as the reference case while for all simulations the lattice Knudsen number was held constant (Kn_L=2.062).

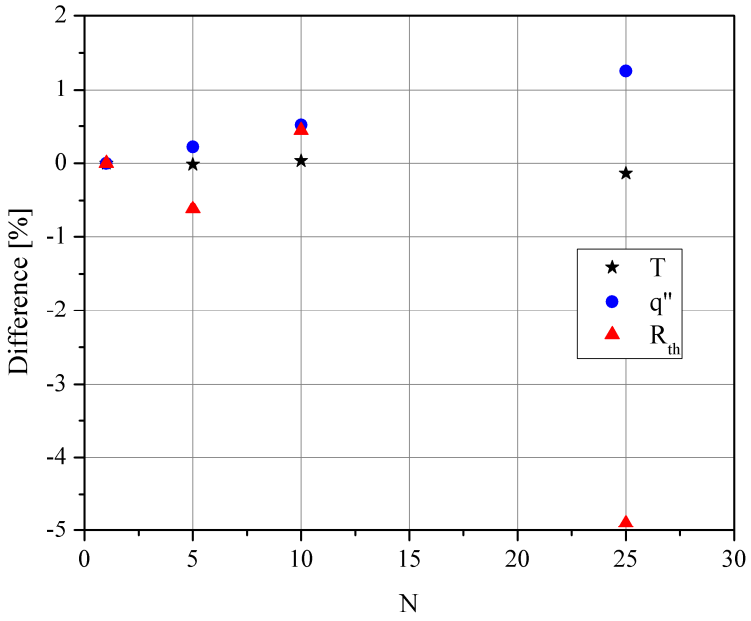

Figure 25: Error introduced into the solution by increasing the coupling ratio (N) at the LB/FD interface.

The error introduced in the maximum temperature at all coupling ratios is not significant (<0.2%), however errors in heat flux and thermal resistance are significant and cannot be ignored. It is therefore suggested that the coupling ratio not exceed 10 to ensure accurate solutions. The results provided here confirm that the coupling method proposed is accurate and provides some simplifications over previous methods.

CHAPTER 4

COMPUTATION OF PHONON RELAXATION TIMES

This chapter begins by outlining the basic phonon dispersion curves developed from lattice dynamics calculations. Using the dispersion curves and an application of Fermi's Golden Rule, expressions for the relaxation time will be presented and discussed. Using these derived expressions a detailed account of both the temperature and wave-vector dependence of the relaxation time will be presented for all phonon modes. Finally, the chapter will present calculations of the bulk thermal conductivity based on the calculated relaxation times.

4.1 Lattice Dynamics

As presented briefly in Section 2.1 the key information needed in order to begin studying phonon relaxation times is a full set of dispersion curves. Again, these dispersion curves show the wavevector/frequency relationship for a particular phonon mode. The basic input needed in order to calculate the dispersion curves comes from knowing the interatomic potential (force field). The force field chosen for this work was of the Tersoff form where the total potential energy can be written as a sum over bond energies as in Eq. (4.1) [91].

$$E = \sum_{i>j} f_{ij}\left(r_{ij}\right)\left[V_{ij}^{R}\left(r_{ij}\right) - \frac{B_{ij}+B_{ji}}{2}V_{ij}^{A}\left(r_{ij}\right)\right] \tag{4.1}$$

$$V_{ij}^{A}\left(r_{ij}\right) = \frac{SD_o}{S-1}\exp\left(-\beta\sqrt{2/S}\left(r-r_o\right)\right) \tag{4.2}$$

$$V_{ij}^{R}\left(r_{ij}\right) = \frac{D_o}{S-1}\exp\left(-\beta\sqrt{2S}\left(r-r_o\right)\right) \tag{4.3}$$

$$B_{ij} = \left(1+\chi_{ij}\right)^{-1/2} \tag{4.4}$$

$$\chi_{ij} = \sum f_{ik}\left(r_{ik}\right) g_{ik}\left(\theta_{ijk}\right) \exp\left[2\mu_{ik}\left(r_{ij}-r_{ik}\right)\right] \tag{4.5}$$

$$g\left(\theta_{ijk}\right) = \gamma\left(1+\frac{c^2}{d^2}-\frac{c^2}{\left[d^2+\left(h+\cos\theta_{ijk}\right)^2\right]}\right) \tag{4.6}$$

Equations (4.2) and (4.3) are contributions to the total potential energy from attractive and repulsive forces, respectively. The function f_{ij} in Eq. (4.1) is a cutoff function, and Eqs. (4.4), (4.5), and (4.6) are the bond-order terms and contain angular terms which are necessary in order to model the covalent nature of the crystal bonds [91]. Parameters used in the above equations can be found in [91] but are summarized here for completeness.

Table 1: Tersoff Potential Parameters from [91]

	Ga-Ga	***N-N***	***Ga-N***
γ	0.007874	0.76612	0.001632
S	1.11	1.4922	1.1122
β [Å^{-1}]	1.08	2.05945	1.968
D_e [eV]	1.4	9.91	2.45
R_e [Å]	2.3235	1.11	1.921
c	1.918	0.178493	64.207
De [eV]	0.75	0.20172	2.821
h = cos[θ]	0.3013	0.045238	0.518
2μ	1.846	0	0
R_{cut}	2.87	2.2	2.9
D [Å]	0.15	0.2	0.2

The Tersoff potential contains explicit terms that describe how the bond formation energy is affected by the atomic arrangement. Accurate material properties, such as bond length, bulk modulus, elastic constants, and solubility have been calculated through the use of the Tersoff potential and found to be agreeable with experimental results [91]. Anharmonic properties, such as the thermal expansion coefficient have also been calculated using the Tersoff potential and found to be agreeable with experimental data for a range of temperatures as shown in Figure 26 [92].

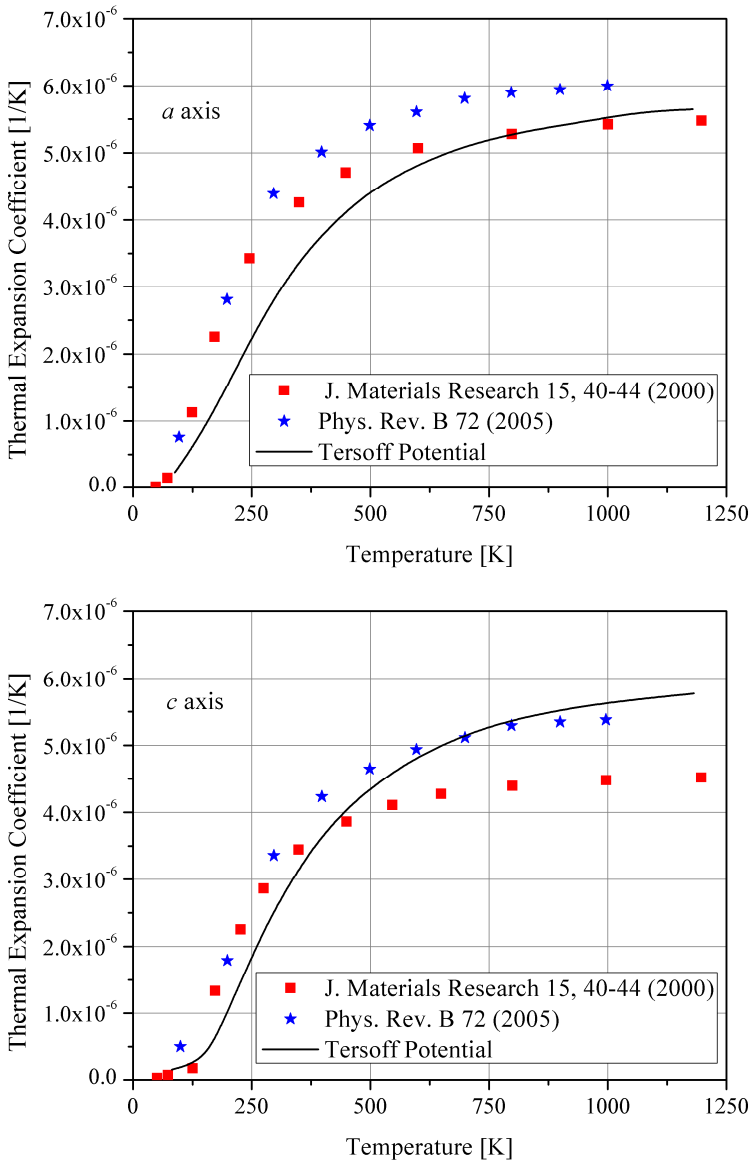

Figure 26: Thermal expansion coefficient for the *a* and *c* axes of the wurtzite GaN crystal calculated using the Tersoff potential, reproduced from [92]. Experimental data from both [93] and [94].

It should be mentioned that the Tersoff potential neglects the ionic nature of the crystal. When ionic atoms vibrate an electrical field will be induced, which can result in the splitting of optical phonon branches. The calculated phonon dispersion curves, using the Tersoff potential, are shown in Figure 27 along major crystal symmetry directions.

Calculations were performed using the computer software package, General Utility Lattice Program (GULP) [95].

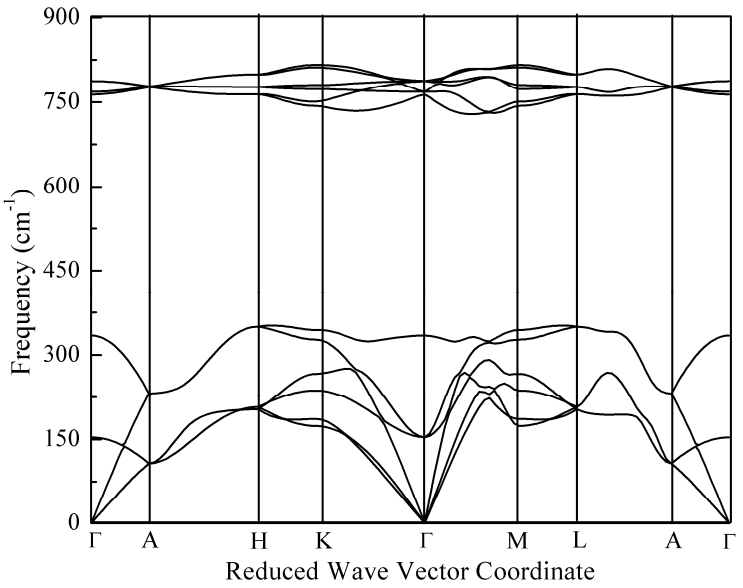

Figure 27: Phonon dispersion curves calculated with the Tersoff interatomic potential.

When comparing optical phonons frequencies at the Γ point to experimental results good agreement is seen for low energy phonons (those below the phononic bandgap). The high energy LO phonon modes also agree with available experimental data. However, when investigating the TO modes, the Tersoff potential does not resolve these as accurately. To correct for this, a set of simplified high energy optical phonon dispersion curves have been adopted to reflect the appropriate frequencies determined from experiment [96].

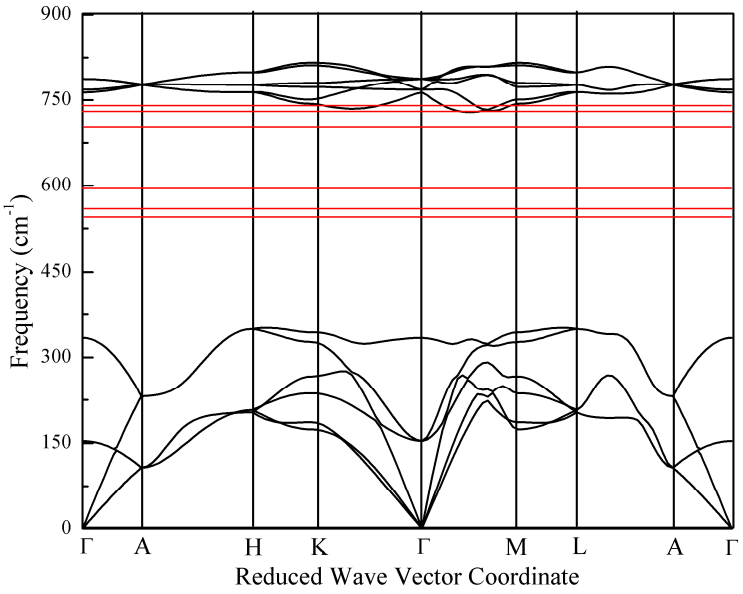

Figure 28: Simplified optical phonon dispersion curves used in this work. Optical phonon frequencies were taken from [96].

The simplified optical phonon frequencies are assumed to be dispersion-less (zero group velocity) as shown in Figure 28. As will be discussed in more detail later in this chapter, this approximation neglects the contribution of the high-energy phonons to the bulk thermal conductivity. However, the true group velocity of high-energy optical phonons is typically very small, and thus overall contribution to the thermal conductivity is small. While high-energy optical phonon contribution is small, the low energy optical phonon contribution has yet to be determined; from the dispersion curves the group velocity is non-negligible. In these modes, the Tersoff potential does resolve the proper phonon frequencies at the Γ point, and it therefore assumed to be accurate throughout the Brillouin zone. As a test, the specific heat was calculated using the full Tersoff model and the simplified high-energy optical phonon model and compared against experimental data. The specific heat was calculated using the expression in Eq. (2.20) using the full Brillouin zone shape.

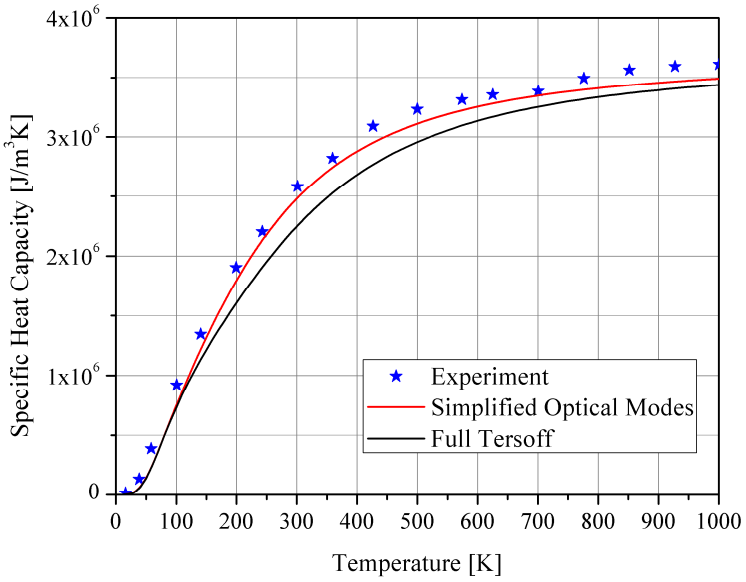

Figure 29: Specific heat of GaN calculated with the simplified high energy optical phonon branches and the full Tersoff potential dispersion curves. Experimental data is from [97].

While good agreement can be observed between experimental data and the full Tersoff model, better agreement is seen between experiment and the simplified optical phonon mode model; this agreement is most recognizable at intermediate temperatures. This highlights the importance of resolving the proper magnitude of the lower frequency TO phonon modes, even if they are dispersionless. For all future calculations, unless otherwise noted, the simplified optical phonon branches will be used in place of the frequencies calculated with the Tersoff potential.

4.2 Relaxation Time Expressions

In the previous section the basic building blocks for studying phonon interactions were discussed and verified by calculating the specific heat of wurtzite GaN. With the set of complete dispersion curves, it is possible to study how phonons interact and

ultimately scatter off each other. This scattering process is referred to as anharmonic scattering or 3-phonon scattering. Following the notation in [31] the transition probability of a phonon in an initial state ($|i\rangle$) to a final state ($|f\rangle$) is given by Fermi's Golden Rule. In Eq. (4.7) E_f is the final state's energy, while E_i was the initial state's energy, and V_3 is then a matrix that contains information about the strength of an interaction between a phonon in an initial state and a phonon in a final state. These matrix elements are derived from the anharmonic contribution to the total crystal potential.

$$P_i^f\left(\text{3-phonon}\right)=\frac{2\pi}{\hbar}\left|\langle f\left|V_3\right|i\rangle\right|^2\delta\left(E_f-E_i\right) \tag{4.7}$$

Here the final state can be given as Eq. (4.9).

$$\begin{aligned}|f\rangle&=\left|n_{\mathbf{q}s}-1,n_{\mathbf{q}'s'}-1,n_{\mathbf{q}''s''}+1\right\rangle \quad \text{fusion event}\\ |f\rangle&=\left|n_{\mathbf{q}s}-1,n_{\mathbf{q}'s'}+1,n_{\mathbf{q}''s''}+1\right\rangle \quad \text{fission event}\end{aligned} \tag{4.8}$$

Energy is conserved in the scattering process through the delta function that appears in Eq. (4.7). By substituting Eq. (4.8) into Eq. (4.7) it is possible to derive the transition probability for both fusion scattering events

$$P_i^f=\frac{2\pi}{\hbar}\left|\left\langle n_{\mathbf{q}s}-1,n_{\mathbf{q}'s'}-1,n_{\mathbf{q}''s''}+1\right|V_3\left|n_{\mathbf{q}s},n_{\mathbf{q}'s'},n_{\mathbf{q}''s''}\right\rangle\right|^2\delta\left(\omega_{\mathbf{q}s}-\omega_{\mathbf{q}'s'}+\omega_{\mathbf{q}''s''}\right) \tag{4.9}$$

and fission scattering events

$$P_i^f = \frac{2\pi}{\hbar}\left|\left\langle n_{\mathbf{q}s}-1, n_{\mathbf{q}'s'}+1, n_{\mathbf{q}''s''}+1\middle|V_3\middle|n_{\mathbf{q}s}, n_{\mathbf{q}'s'}, n_{\mathbf{q}''s''}\right\rangle\right|^2 \delta\left(\omega_{\mathbf{q}s}-\omega_{\mathbf{q}'s'}-\omega_{\mathbf{q}''s''}\right) \quad (4.10)$$

At this stage $n_{\mathbf{q}s}$ represents the total number of phonons in mode **q**s (non-equilibrium distribution function). It is necessary to introduce the isotropic continuum assumption in order to develop a tractable expression for the anharmonic potential, V_3, the details of which can be found in [31]. Through the development of the phonon transition probabilities and incorporating the single mode relaxation time approximation, an expression for the scattering operator on the right hand side of the BTE can be written.

$$-\left.\frac{\partial n_{\mathbf{q}s}}{\partial t}\right|_{\text{3-phonon}} = \frac{n_{\mathbf{q}s}-n_{\mathbf{q}s}^o}{\tau} = \sum_{\mathbf{q}'s'\mathbf{q}''s''}\left[\left(P_{\mathbf{q}s,\mathbf{q}'s'}^{\mathbf{q}''s''}+\frac{1}{2}P_{\mathbf{q}s}^{\mathbf{q}'s',\mathbf{q}''s''}\right)\right] \quad (4.11)$$

By incorporating the anharmonic potential term, Srivastava derived the following expression for the relaxation time of a 3-phonon process.

$$\begin{aligned}\tau_{\mathbf{q}s}^{-1} = {} & \frac{\pi\hbar}{4\rho^3 N_o \Omega}\sum_{\mathbf{q}'s'\mathbf{q}''s''}\left|A_{\mathbf{q}\mathbf{q}'\mathbf{q}''}^{ss's''}\right|^2 \frac{\mathbf{q}\mathbf{q}'\mathbf{q}''}{v_s v_{s'} v_{s''}}\delta_{\mathbf{q}+\mathbf{q}'+\mathbf{q}'',\mathbf{G}} \\ & \times\left\{\frac{n_{\mathbf{q}'s'}\left(n_{\mathbf{q}''s''}+1\right)}{n_{\mathbf{q}s}+1}\delta\left(\omega_{\mathbf{q}s}+\omega_{\mathbf{q}'s'}-\omega_{\mathbf{q}''s''}\right)+\frac{1}{2}\frac{n_{\mathbf{q}'s'}n_{\mathbf{q}''s''}}{n_{\mathbf{q}s}}\delta\left(\omega_{\mathbf{q}s}-\omega_{\mathbf{q}'s'}-\omega_{\mathbf{q}''s''}\right)\right\}\end{aligned} \quad (4.12)$$

Here N_o is the number of unit cells, Ω is the volume per crystal unit cell, and ρ is the mass density, $n_{\mathbf{q}s}$ in Eq. (4.12) now represents the Bose-Einstein distribution function in Eq. (2.18). The previous expression, although derived under the assumption of an isotropic continuum material, is still very complicated and will need to be simplified further before calculations begin. Before continuing it is important to note some of the terms. The expression $A^{ss's''}_{\mathbf{qq'q''}}$ is referred to as the phonon coupling constant. This coupling constant is mode and wavevector dependent, however a uniform-strain approximation was introduced by Klemens that has been incorporated in previous phonon studies with success [43]. In Srivastava's notation this uniform-strain approximation yields Eq. (4.14).

$$\left|A^{ss's''}_{\mathbf{qq'q''}}\right|^2 = \frac{4\rho^2}{\bar{v}^2}\gamma^2 v_s^2 v_{s'}^2 v_{s''}^2 \tag{4.13}$$

In Eq. (4.13) the Gruneisen parameter, γ, is introduced to account for anharmonic effects that occur; ρ is the density of the material and $\bar{v}$ is the average velocity of the acoustic modes. Formally, the Gruneisen parameter describes how the frequency of a phonon changes with crystal volume. However, the Gruneisen parameter is often left as an adjustable parameter in order to recover the bulk thermal conductivity. A reformulation of Eq. (4.13) was proposed where an anharmonic parameter, F, was introduced as simply $\gamma/\bar{v}$ [98].

$$\left|A^{ss's''}_{\mathbf{qq'q''}}\right|^2 = 4\rho^2 F^2 v_s^2 v_{s'}^2 v_{s''}^2 \tag{4.14}$$

In theory the phonon coupling constants can be derived from the third derivative of the interatomic potential, however this requires knowledge of a mature interatomic potential and a sophisticated numerical method for calculating an accurate third derivative [39]. This procedure will be left as future work since there is still development that must occur regarding GaN interatomic potentials [99].

Before discussing the methods of calculating the phonon relaxation times it is necessary to study the behavior of the anharmonic parameter, F, in order to gain confidence in the final calculated relaxation times. Ultimately, the temperature dependence of the thermal conductivity is desired, therefore as a first step the temperature dependence of the anharmonic parameter is investigated. Since F is an aggregate quantity of the Gruneisen parameter and the average group velocity, the temperature dependence of each of these quantities was initially investigated separately, and then later combined. The temperature variation of $\gamma$is shown in Figure 31, the data has been taken from [92]. Additionally, the average phonon group velocity was calculated for all low energy phonon modes (all modes below the bandgap). The velocity was calculated through application of Eq. (2.17) throughout the entire Brillouin zone. The average of all these velocities was calculated as the weighted average based on the phonon occupation number. The normalized occupation number (the weighting function) is shown in Figure 30 as a function of phonon energy and temperature. The results are presented in Figure 31.

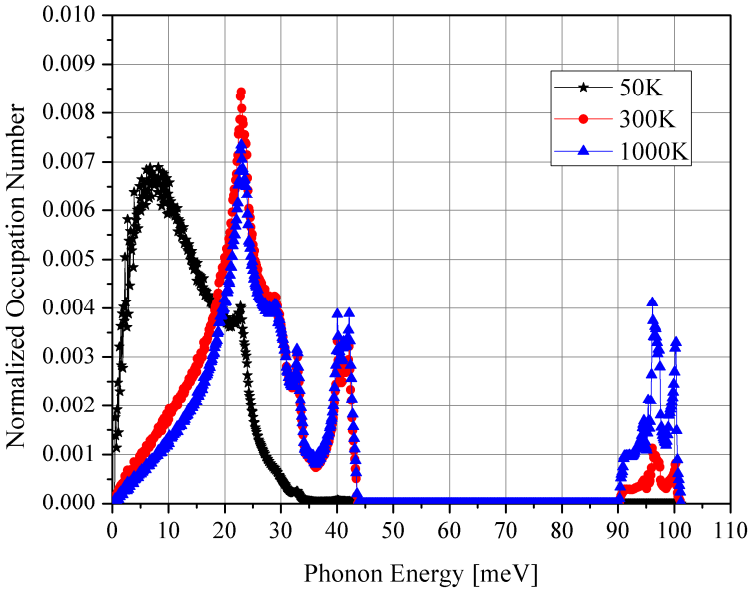

Figure 30: Normalized occupation number used for calculating the weighted average group velocity of the low energy phonon modes.

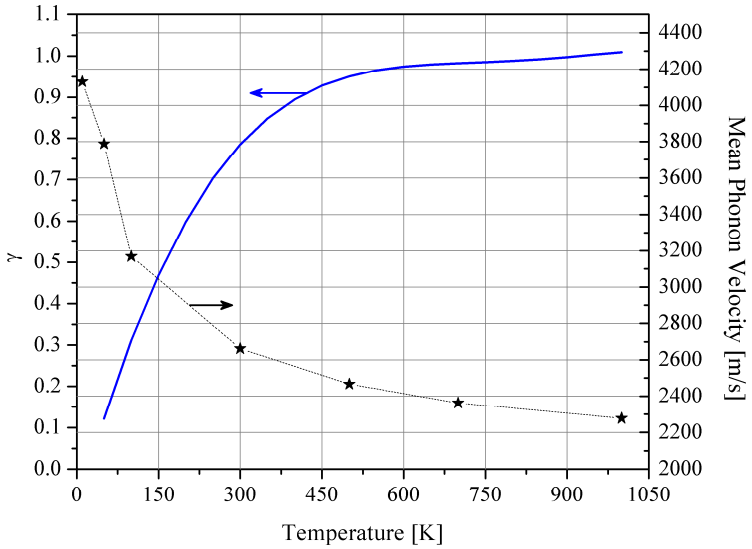

Figure 31: Temperature dependence of the Gruneisen parameter and the average phonon group velocity.

The temperature dependence of the Gruneisen parameter is difficult to generalize, but as a first order approximation the low and high temperature trends can be estimated to have the following functional form [31].

$$\gamma_{low} = \gamma_o \left(1 + bT^2\right) \tag{4.15}$$

$$\gamma_{high} = \gamma_\infty \left(1 - c/T^2\right) \tag{4.16}$$

In combining the results from Figure 31 the anharmonic parameter was calculated. The high and low temperature functional forms were estimated to be the same as that for the Gruneisen parameter. The behavior of *F* is presented in Figure 32.

$$F_{low} = F_o \left(1 + bT^2\right) \tag{4.17}$$

$$F_{high} = F_\infty \left(1 - c/T^2\right) \tag{4.18}$$

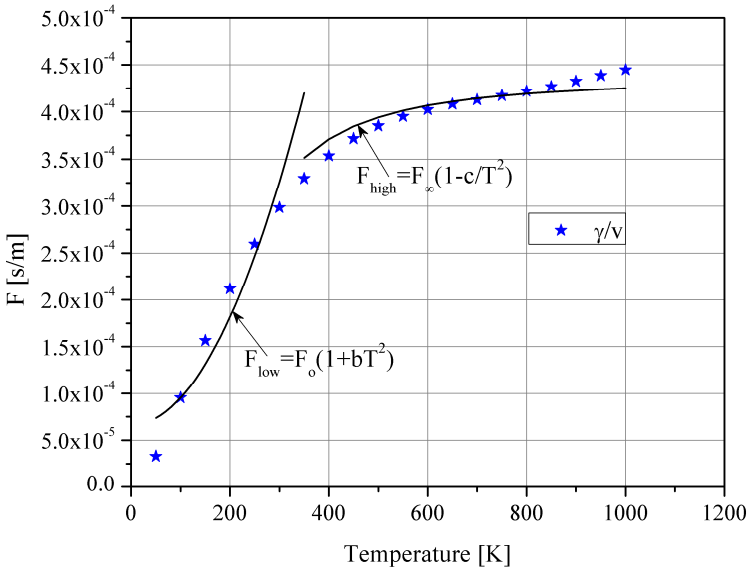

Figure 32: Temperature dependence of the anharmonic parameter, *F*. Limiting high and low temperature trends are shown as well.

In the Eq. (4.17) the F_o parameter is the low temperature limiting anharmonic parameter, in contrast F_∞ is the high temperature limiting value (Eq. (4.18)). From Figure 32 it can be seen that the anharmonic parameter in the limiting cases matches well with the first order approximation that was presented. It is also noted that for temperatures of ~300 K and above, the anharmonic parameter is only a weak function of temperature as it is close to its limiting value of F_∞. While the anharmonic parameter is a key input and dictates the final magnitude of the relaxation time, less stress should be placed on the absolute magnitude of this parameter. As mentioned previously the Gruneisen parameter is typically used as a fitted parameter in order to capture the correct bulk thermal conductivity; the anharmonic parameter is no different. Therefore instead of being concerned with the magnitude of *F*, it is more important that this fitted quantity follow a

similar temperature trend that is then congruent with the temperature trend of the relaxation time.

Capturing the proper temperature dependence of the anharmonic parameter is one component for calculating the relaxation time. It is also necessary to have a robust Brillouin zone integration scheme in order to perform the summations in Eq. (4.12). As a first step, by incorporating Eq. (4.14) into the relaxation time expression, the simplified form is achieved.

$$\tau_{\mathbf{q}s}^{-1} = \frac{\pi\hbar F^2}{\rho\Omega} \sum_{\mathbf{q}'s'\mathbf{q}''s''} \omega_{\mathbf{q}s}\omega_{\mathbf{q}'s'}\omega_{\mathbf{q}''s''}\delta_{\mathbf{q}+\mathbf{q}'+\mathbf{q}'',\mathbf{G}} \times\left\{\frac{n_{\mathbf{q}'s'}\left(n_{\mathbf{q}''s''}+1\right)}{n_{\mathbf{q}s}+1}\delta\left(\omega_{\mathbf{q}s}+\omega_{\mathbf{q}'s'}-\omega_{\mathbf{q}''s''}\right)+\frac{1}{2}\frac{n_{\mathbf{q}'s'}n_{\mathbf{q}''s''}}{n_{\mathbf{q}s}}\delta\left(\omega_{\mathbf{q}s}-\omega_{\mathbf{q}'s'}-\omega_{\mathbf{q}''s''}\right)\right\} \tag{4.19}$$

Solving this equation is not trivial due to complications with the handling the delta functions. The first delta function $\delta_{\mathbf{q}+\mathbf{q}'+\mathbf{q}'',\mathbf{G}}$, and therefore the summation over $\mathbf{q}''$, is handled by direct application of the conservation of crystal momentum expressions in Eqs. (2.26) and (2.28). The value of the vector **G** can be any one of the 8 reciprocal lattice vectors in the GaN Brillouin zone. For future equations it is assumed that this delta function is obeyed implicitly. Difficulties arise when trying to handle the conservation of energy delta functions. A Lorentzian peak has been used to approximate the delta function where a small width parameter is introduced as ε [100-103].

$$\delta(x) \approx \frac{\varepsilon}{x^2+\varepsilon^2} \tag{4.20}$$

Additionally, the delta function can be approximated by a sharp Gaussian peak [98, 104].

$$\delta(x) \approx \frac{1}{\sigma\sqrt{\pi}} \exp\left[-\left(\frac{x}{\sigma}\right)^2\right] \tag{4.21}$$

For this study the Gaussian shape will be utilized; by incorporating this approximation the relaxation time expression is then given by Eq. (4.23).

$$\begin{aligned}\tau_{\mathbf{q}s}^{-1} = {} & \frac{\pi\hbar F^2}{\rho\Omega} \frac{1}{\sigma\omega_{\mathbf{q}s}\sqrt{\pi}} \sum_{\mathbf{q}'s's''} \omega_{\mathbf{q}s}\omega_{\mathbf{q}'s'}\omega_{\mathbf{q}''s''} \\ & \times \left\{ \begin{array}{l} \dfrac{n_{\mathbf{q}'s'}\left(n_{\mathbf{q}''s''}+1\right)}{n_{\mathbf{q}s}+1} \exp\left[-\left(\dfrac{\omega_{\mathbf{q}s}+\omega_{\mathbf{q}'s'}-\omega_{\mathbf{q}''s''}}{\sigma\omega_{\mathbf{q}s}}\right)^2\right] + \ldots \\ \dfrac{1}{2}\dfrac{n_{\mathbf{q}'s'}n_{\mathbf{q}''s''}}{n_{\mathbf{q}s}} \exp\left[-\left(\dfrac{\omega_{\mathbf{q}s}-\omega_{\mathbf{q}'s'}-\omega_{\mathbf{q}''s''}}{\sigma\omega_{\mathbf{q}s}}\right)^2\right] \end{array} \right\}\end{aligned} \tag{4.22}$$

By calculating the delta function in this way a link is formed between the mesh spacing in the Brillouin zone and the peak broadening parameter, σ. If the Brillouin zone mesh is too coarse and the broadening parameter too narrow, none of the terms in the summation will survive. Conversely, if the broadening parameter is too large, the effects of the discrete phonon interactions will be washed out. It is therefore necessary to tune the broadening parameter in order to observe a stable value of the relaxation time for the phonon of interest. This convergence study was performed for every phonon mode as the broadening parameter is expected to be mode dependent. In Figure 33 a sample

converged relaxation time was achieved when the number of mesh points was large and the broadening parameter was relatively narrow (red stars).

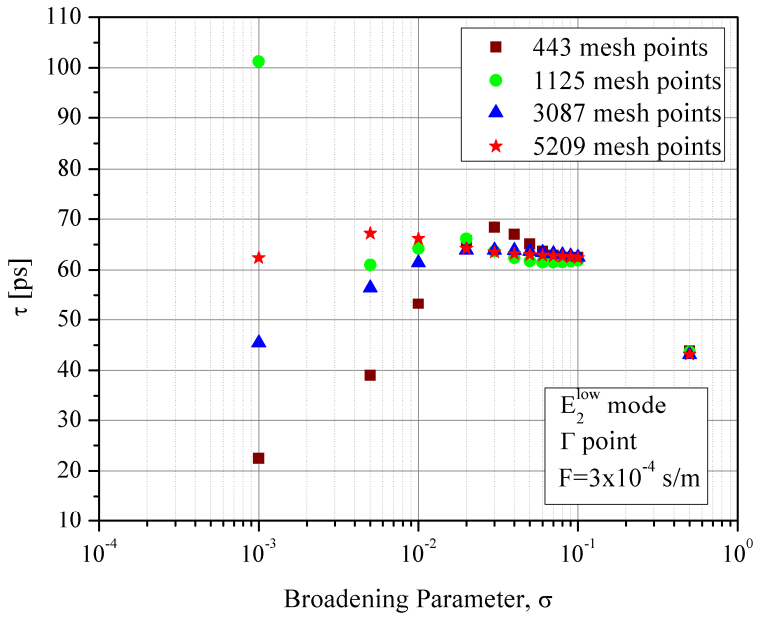

Figure 33: Convergence of the relaxation time as a function of mesh density and broadening parameter for the E_2^1 phonon mode. The anharmonic parameter was set at 3.0x10^{-4} sm^{-1} for the convergence study only.

From the above figure, it can be seen that the relaxation time can have a chaotic dependence on broadening parameter/mesh density. This highlights the necessity of this study prior to any further calculations of the relaxation time. As an initial starting point, the broadening parameter can be set to between 1-5% of the maximum phonon frequency; refinements from this point can then be made.

In order to perform the summation over the $\mathbf{q}'$ points in Eq. (4.22) a weighted summation over the irreducible Brillouin zone was performed. In general the zone averaged function $f(\mathbf{q})$ can be represented as Eq. (4.24).

$$f(\mathbf{q}) = \sum_{i=1}^{M} w_i f(\mathbf{q}_i) \tag{4.23}$$

Here the weighting factors, w_i, must sum to 1. In order to generate these weighting factors the irreducible Brillouin zone was filled with tetrahedral volume elements, as shown in Figure 34.

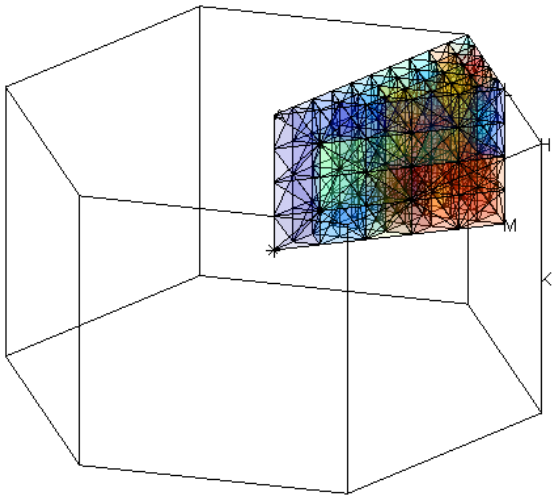

Figure 34: Tessellated irreducible Brillouin zone.

If the total volume of the irreducible Brillouin zone is given as V and the volume of each volume element is given as Eq. (4.25), the weight is then calculated as V_i/V ; where V_i represents the volume of each tetrahedron.

$$V_i = \frac{1}{3!}\begin{vmatrix} 1 & x_1 & y_1 & z_1 \\ 1 & x_2 & y_2 & z_2 \\ 1 & x_3 & y_3 & z_3 \\ 1 & x_4 & y_4 & z_4 \end{vmatrix} \tag{4.24}$$

In Eq. (4.24) the *x, y,* and *z* values represent the coordinates of the vertices of each tetrahedron. By incorporating this weighting scheme into the relaxation time expression the final usable form emerges.

$$\tau_{\mathbf{q}s}^{-1} = \frac{\pi\hbar F^2}{\rho\Omega}\frac{1}{\sigma\omega_{\mathbf{q}s}\sqrt{\pi}} \times \sum_{s's''}\sum_{i=1}^{M} w_i \omega_{\mathbf{q}s}\omega_{\mathbf{q}_i's'}\omega_{\mathbf{q}''s''} \times \left\{ \begin{array}{c} \dfrac{n_{\mathbf{q}_i's'}\left(n_{\mathbf{q}''s''}+1\right)}{n_{\mathbf{q}s}+1}\exp\left[-\left(\dfrac{\omega_{\mathbf{q}s}+\omega_{\mathbf{q}_i's'}-\omega_{\mathbf{q}''s''}}{\sigma\omega_{\mathbf{q}s}}\right)^2\right]+\ldots \\ \dfrac{1}{2}\dfrac{n_{\mathbf{q}_i's'}n_{\mathbf{q}''s''}}{n_{\mathbf{q}s}}\exp\left[-\left(\dfrac{\omega_{\mathbf{q}s}-\omega_{\mathbf{q}_i's'}-\omega_{\mathbf{q}''s''}}{\sigma\omega_{\mathbf{q}s}}\right)^2\right] \end{array} \right\} \tag{4.25}$$

It is important to note that the above expression holds true for both N-processes as well as U-processes; all future calculations will be presented as a combination of both processes. In summary, to calculate the relaxation time the following procedure is implemented for a particular phonon mode, $\mathbf{q}s$ (Figure 35).

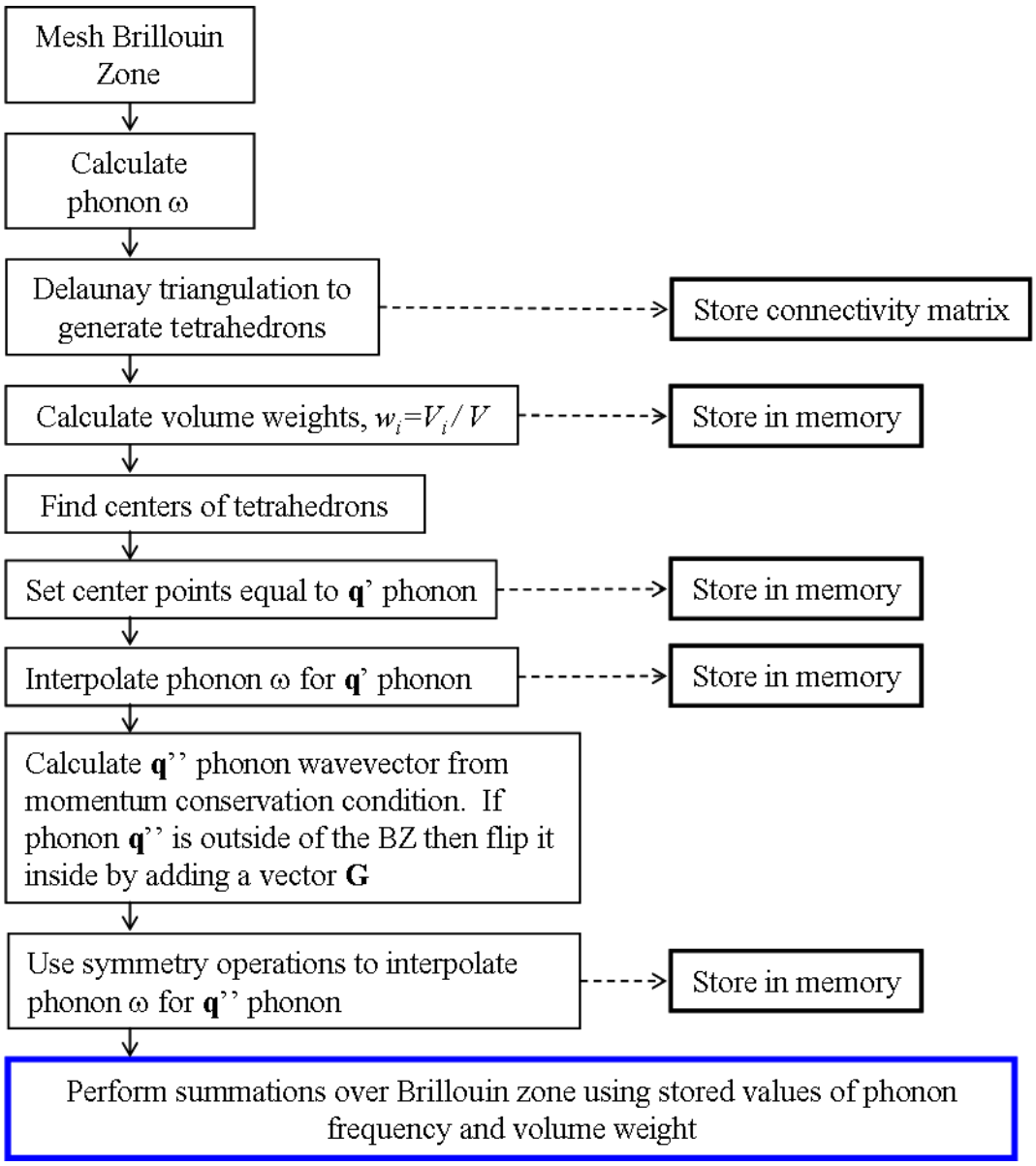

Figure 35: Flowchart describing the process used to calculate the phonon relaxation time.

During the interpolation step used to calculate $\omega(\mathbf{q}"s)$ a linear function was found to be sufficient. Interpolation within a tetrahedron is made easier by transforming the problem into volume coordinates [105].

4.3 Relaxation Time Results

The previous section outlined the method used for calculating the relaxation time for a particular phonon mode. This section discusses the results of relaxation time calculations in detail for all phonon modes in GaN. The temperature and wavevector dependence of the relaxation times will also be discussed.

4.3.1 Relaxation Processes

For any particular phonon mode there are several possible interaction pathways. Again, energy and crystal momentum conservation laws govern these interactions. There are four specific phonon interaction pathways that may occur in any given material that will be discussed. The Klemens pathway occurs when an optical phonon mode decays into two acoustic phonons [106].

$$O \leftrightarrow A + A \quad \text{Klemens Pathway} \tag{4.26}$$

This process is the dominant decay mechanism in materials that have no phononic bandgap, such as silicon. The Ridley process occurs when a high energy optical phonon decays into a lower energy optical phonon and an acoustic phonon [107].

$$O \leftrightarrow O' + A \quad \text{Ridley Pathway} \tag{4.27}$$

The Ridley pathway occurs primarily in materials that have a phononic bandgap; however the bandgap is not large enough to prevent decay into low energy acoustic modes. The process is dominant in GaN high energy LO modes. If the phononic

bandgap is very large, a Barman-Srivastava decay process might be necessary [108]. In this process a high-energy optical phonon mode decays into lower energy TO phonon modes.

$$LO \leftrightarrow TO + TO \quad \text{Barman-Srivastava Pathway} \tag{4.28}$$

This type of process exists in materials such as InN where the mass ratio between the two atoms in the unit cell is very high ($m_{In}/m_N = 8.20$). One last process is referred to as the Vallee-Bogani pathway [109, 110]. In this case there is sufficient dispersion of an optical mode where a zone center phonon can decay into a zone edge phonon of the same branch as well as an acoustic phonon.

$$O_{center} \leftrightarrow O_{edge} + A \quad \text{Vallee-Bogani Pathway} \tag{4.29}$$

Other processes are possible; however these do not have any particular name associated with them.

$$\begin{aligned} O_{\text{high energy}} &\leftrightarrow O_{\text{low energy}} + O_{\text{low energy}} \\ A &\leftrightarrow A + A \end{aligned} \tag{4.30}$$

The first of these processes shown in Eq. (4.30) is the dominant decay pathway for zone center GaN TO phonons. As an example, Figure 36 is presented that highlights possible decay pathways for a low energy TO mode in GaN. It is possible to see from this figure

that if a zone center phonon decays it must produce two large wavevector phonons; this decay process occurs through an N-process.

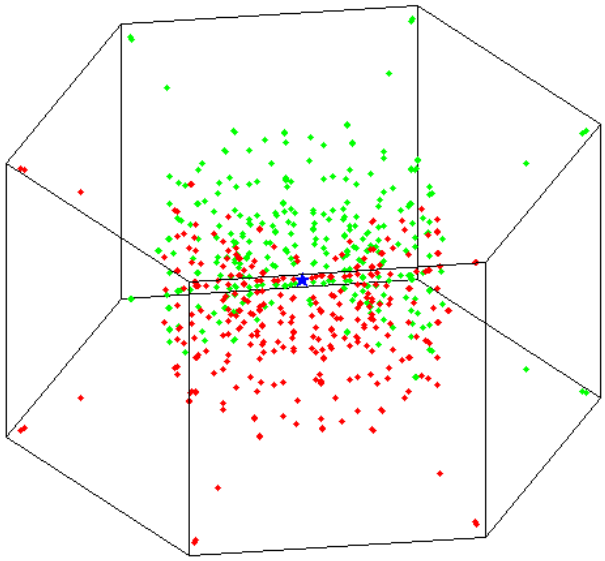

Figure 36: Phonon decay possibilities for a zone center TO mode. Red points are **q**' phonons and the green points are **q**" interacting phonons. This figure was generated with a phonon interaction searching algorithm developed in [34].

4.3.2 Optical Phonon Mode Relaxation Times

Recently there have been a number of experimental investigations into the relaxation time of zone center optical phonons in GaN [111-117]. These phonons can be interrogated and their relaxation times characterized through a variety of optical techniques such as linewidth based Raman spectroscopy measurements and sub-picosecond time-resolved Raman spectroscopy. It should be noted that not all optical phonon modes are Raman active, both the B_1^1 and B_1^2 modes are always silent and cannot be measured experimentally. Using the experimental values for optical phonon modes it

is possible to determine the anharmonic parameter, *F*, for each mode, the anharmonic parameter for the Raman silent modes must be estimated.

When comparing the relaxation time determined from experiments to a theoretical value it is important to take into account the crystal quality of the grown GaN layer. Most of the films investigated were grown by either molecular beam epitaxy (MBE) or metal-organic chemical vapor deposition (MOCVD) techniques. Both methods can result in high quality films, with low dislocation densities ($<10^8$ cm^{-3}) and low levels of impurity atoms. While this can be qualitatively said, a full characterization of the grown film for any of the referenced studies was not performed. Therefore, it must be assumed for all modes that the GaN is of high enough quality where, at high temperatures, the main contribution to the total phonon relaxation time comes from anharmonic scattering instead of from other temperature-independent scattering mechanisms. Extrapolations of the relaxation times were made to low temperatures for completeness; no attempt to estimate the effects of other scattering mechanisms was attempted. As discussed earlier, the anharmonic parameter must be fit in order to recover the experimental values of the relaxation time. The fit value of *F* was determined by matching the model with an experimental value at 300 K only. At high temperatures Figure 32 showed that there is a weak dependence of *F* with temperature, therefore a constant value should result in reasonable recovery of all high temperature relaxation times. As will be seen, this was observed to be true for all optical phonon modes, giving confidence that the model, with all the incorporated approximations, can still accurately capture the underlying physical phenomena.

For all phonon modes the full form of the relaxation time expression in Eq. (4.25) was used; the first term in the braces accounts for fusion events while the second term accounts for fission scattering processes. It has been proposed that the scattering rate of phonon fusion and fission processes are roughly equal for any phonons scattering event; therefore both types of processes must be considered when calculating the total relaxation time [118]. This is in contrast with results presented in Usher *et al.*, where it was found that for high energy LO phonon modes the contribution to the total anharmonic relaxation time is dominated by fission processes only [62]. The results of this work support the latter study for LO phonon modes, but in investigating the scattering rate of low energy phonons it was found that the total relaxation time is dominated by fusion events. This is especially apparent for the low energy E_2^1 mode scattering rate. In considering phonons of intermediate energy, the contribution to the total scattering rate is due to nearly equal parts of fission/fusion scattering processes. These trends will be developed in the following sections.

4.3.2.1 E_2^1 (E_2^{low}) Mode

The E_2^1 phonon mode is the lowest energy optical phonon and a frequency at the Γ point of approximately 137 cm^{-1}. Bergman *et al.* measured the phonon relaxation time with a Raman spectroscopy technique based on measuring the linewidth of the spectra and using the energy-time form of the Heisenberg uncertainty principle [112]. The results from this experiment are shown in Figure 37.

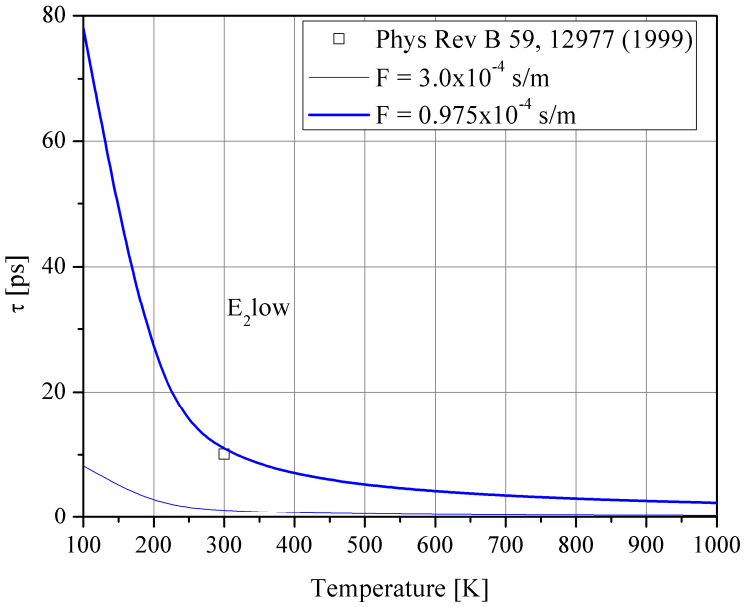

Figure 37: Temperature dependence of the E_2^1 phonon mode.

The figure shows the results of the estimated anharmonic parameter from Figure 32 as well as a value that allowed for the experimental value to be recovered. It is interesting to note that this phonon mode has the longest relaxation time by a factor of 5 more than any other optical phonon mode. Combining the mode's long relaxation time and non-negligible group velocity, the E_2^1 mode is hypothesized to contribute to the total thermal conductivity in a significant way; this contribution will be discussed in more detail in section 4.3.3. Breaking the contributions to the total relaxation times into components the following trends were observed, the results are presented in Figure 38.

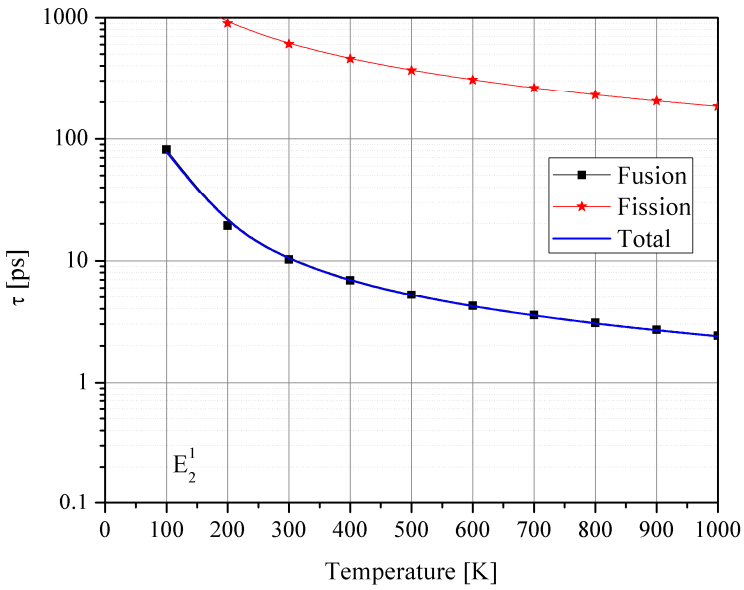

Figure 38: Contributions to the total relaxation time from both fusion and fission phonon scattering processes.

It can be clearly seen from Figure 38 that the total anharmonic relaxation time is completely dominated by the fusion process; phonon fission events have relaxation times that are many orders of magnitude larger. It should be noted that the total relaxation time is a balance of both fusion and fission processes; each of these processes has a unique transition probability associated with it. The transition probability is a function of both the phonon distribution function as well as an intrinsic transition probability as discussed in [31]. Following the principle of microscopic reversibility, the intrinsic transition probability must be equal for both fusion and fission processes. Therefore the transition probability from an initial state into a final state is governed by the details of the distribution function of the scattering phonons. These details can cause the total relaxation time to be dominated by one type of process, as is the case in Figure 38.

4.3.2.2 B_1^1 Mode

This phonon mode is Raman inactive and therefore there exist no data in order to fit the anharmonic parameter. The value of *F* was approximated to be the same as the E_2^1 low energy phonon mode; a value of 0.975×10^{-4} sm^{-1} was adopted. In Figure 39 the estimated relaxation times are presented. In contrast to the E_2^1 phonon mode, the total relaxation time is governed by contributions from both fusion and fission processes, particularly at low temperatures, as seen in Figure 40.

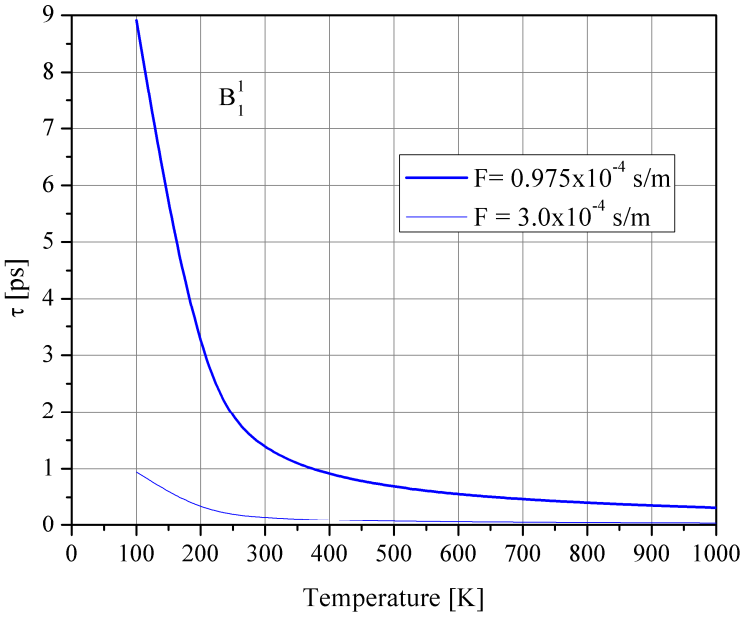

Figure 39: Temperature dependence of the B_1^1 phonon mode.

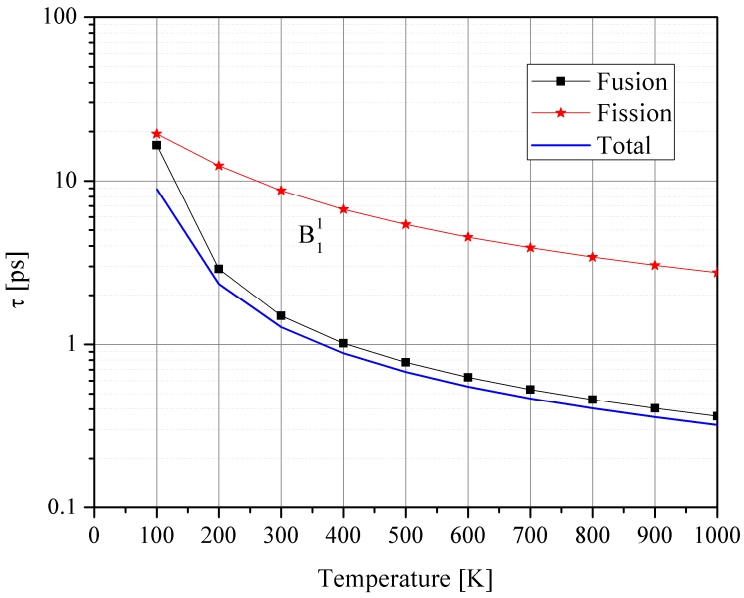

Figure 40: Contributions to the total relaxation time from both fusion and fission phonon scattering processes.

4.3.2.3 $A_1(TO)$ Mode

Many experimental investigations have been made into the temperature dependence of the relaxation time for the $A_1(TO)$ mode [111-114]. All of these investigations were performed with Raman spectroscopy linewidth measurements. In [111] corrections were made to the collected spectra that removed the dispersion effects of the spectrometer [119, 120]. While all relaxation time data was approximately equal, the value at 300 K from [111] was used in order to fit the anharmonic parameter. As expected, relaxation times at higher temperatures continued to match experimental data. This agreement is possible since the anharmonic parameter at temperatures >300 K is only a weak function of temperature. Differences in the experimental data are likely caused by differing levels of crystal defects.

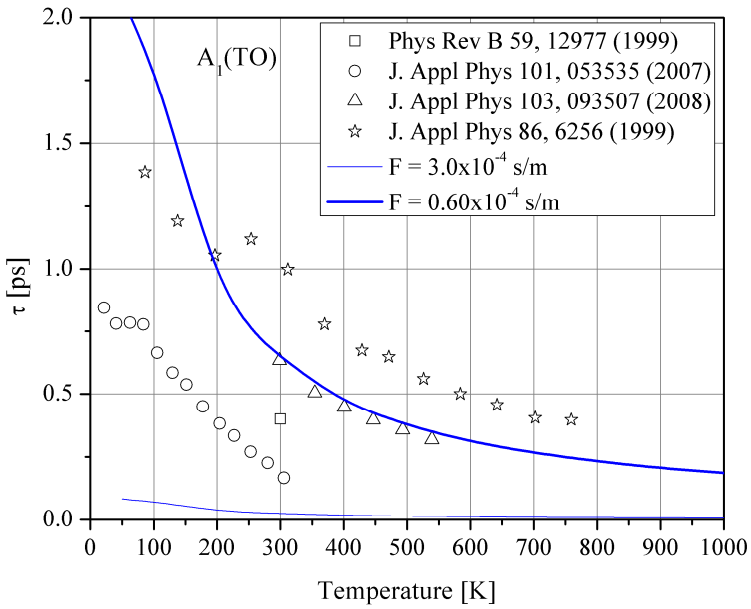

Figure 41: Temperature dependence of the $A_1(TO)$ phonon mode.

The contributions to the total relaxation time follow the same trend as the B_1^1 mode; the contributions from both fusion and fission processes are very similar except at low temperatures where fission processes dominate.

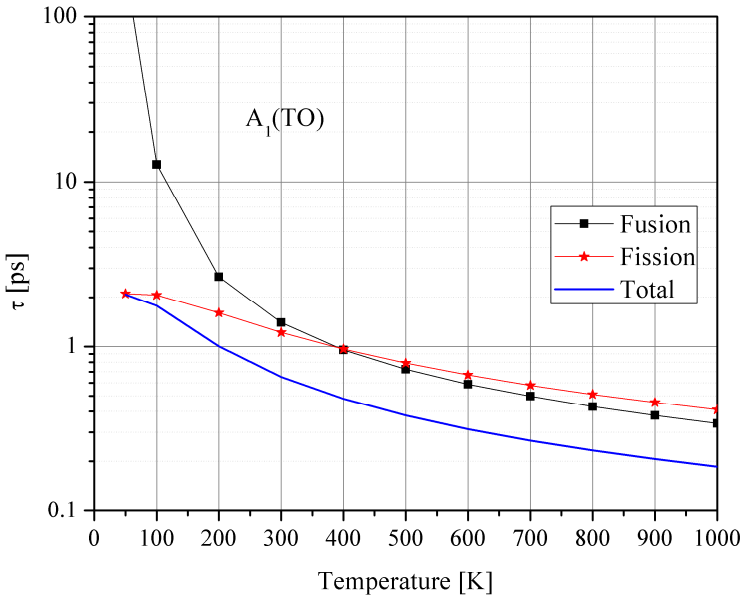

Figure 42: Contributions to the total relaxation time from both fusion and fission phonon scattering processes.

4.3.2.4 $E_1(TO)$ Mode

The $E_1(TO)$ phonon mode was measured by Bergman *et al.* as well as by Song *et al.* [112, 114]. This particular mode is only accessible with the $x(yz)\bar{x}$ or $x(yz)y$ Raman scattering configurations [121]. Since temperature dependent data was only available from one source the relaxation time at 300 K from this set was used to fit the anharmonic parameter; Figure 43 presents the results from the simulations. As can be seen from Figure 43 there is remarkable agreement with the modeled relaxation times, even at low temperatures. In Song *et al.* it was assumed that only symmetric fission processes involving both 3 and 4 phonons contribute to the total relaxation time. In order to match experimental data, a phonon frequency shift due to thermal expansion was also included. The modeled relaxation time in this work was obtained with the full expression shown in Eq. (4.25) and did not assume any thermal expansion-induced frequency shifts. With this more general model, it is concluded that the dispersive nature of the low energy

phonons leads to the strong temperature dependence rather than thermal expansion effects. Additionally, it is emphasized that the balance between fission and fusion phonon scattering events must be developed in order to calculate the total relaxation time. In Figure 44 the importance of including both fission/fusion scattering processes is highlighted as they have nearly equivalent scattering rates.

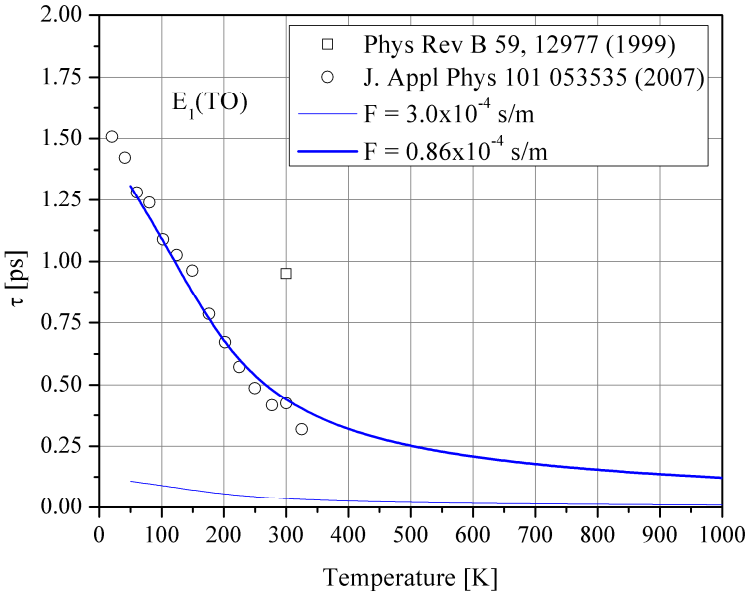

Figure 43: Temperature dependence of the $E_1(TO)$ phonon mode.

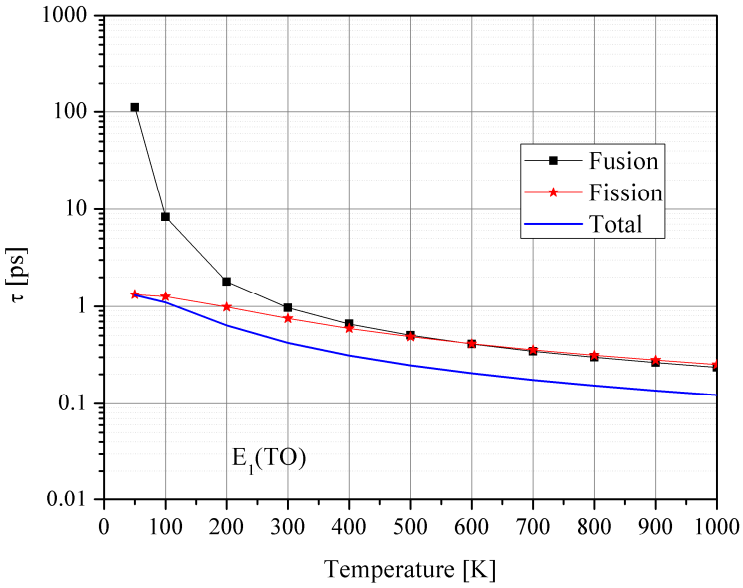

Figure 44: Contributions to the total relaxation time from both fusion and fission phonon scattering processes.

4.3.2.5 E_2^2 (E_2^{high}) Mode

As with the $A_1(TO)$ there exist numerous experimental studies into the temperature dependence of the E_2^2 phonon mode relaxation time [111-114]. The results of the various experiments as well as the fitted model are shown in Figure 45. As with previous modes, the high temperature trends match well, even though the anharmonic parameter is considered to be temperature independent. At low temperatures (<300 K) there is some deviation from the model and experimental data; this difference is attributed to various impurities or defects within the experimental sample. This argument is reinforced by the fact that the relaxation time at these low temperatures is relatively constant; signifying that only temperature independent scattering processes are dominate.

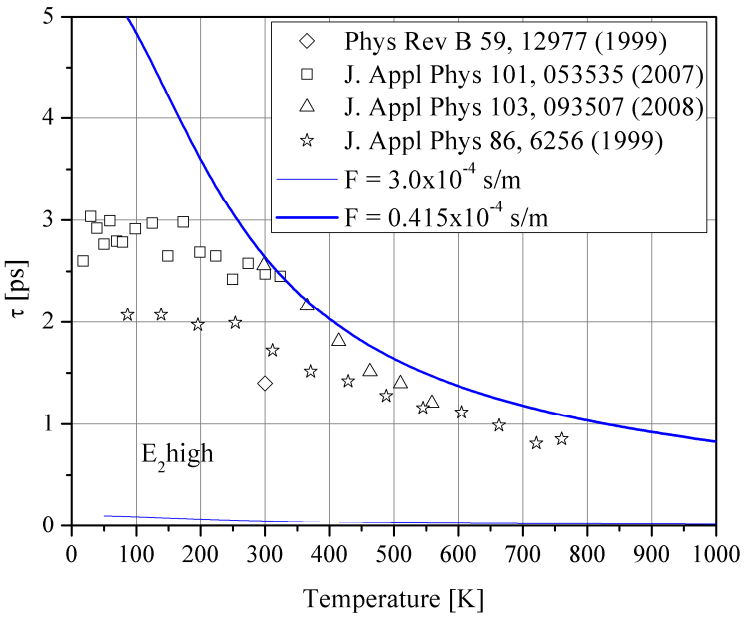

Figure 45: Temperature dependence of the E_2^2 (E_2^{high}) phonon mode relaxation time.

The contributions to the total relaxation time are shown in Figure 46. It is clear with the E_2^2 mode that fission processes are tending to dominate the final value of the relaxation time at all temperatures. This figure highlights the fact that there exists a region at intermediate phonon energies in which the dominant scattering process switches from the fusion processes to the fission processes.

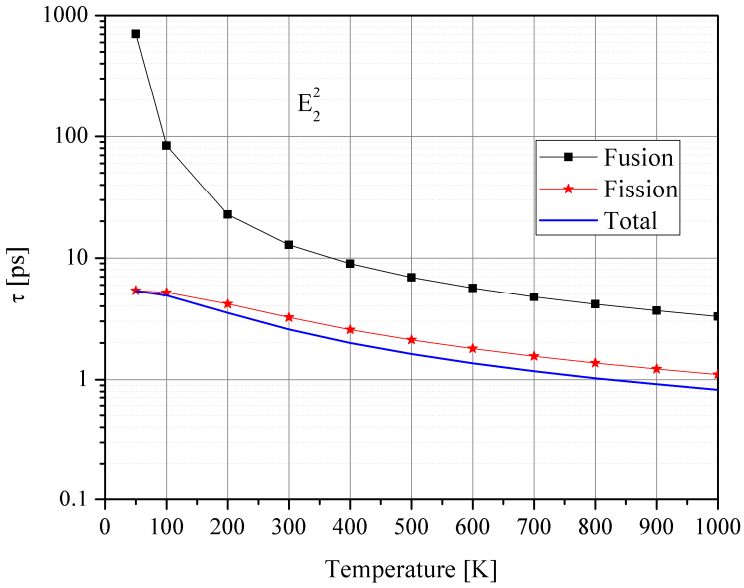

Figure 46: Contributions to the total relaxation time from both fusion and fission phonon scattering processes.

4.3.2.6 B_1^2 Mode

As with the B_1^1 phonon mode, the B_1^2 mode is Raman inactive, and as such no experimental data was available for the relaxation time. In order to approximate the anharmonic parameter a value of 0.60×10^{-4} sm^{-1} was chosen. This value was found to be nearly constant across other high-energy optical phonon modes. It was assumed that this value also held for the B_1^2 mode. The estimated relaxation time is presented in Figure 47. The diminishing importance of the fusion process continues as the scattering rate contribution is several orders of magnitude slower for fusion processes. This data is reflected in Figure 48.

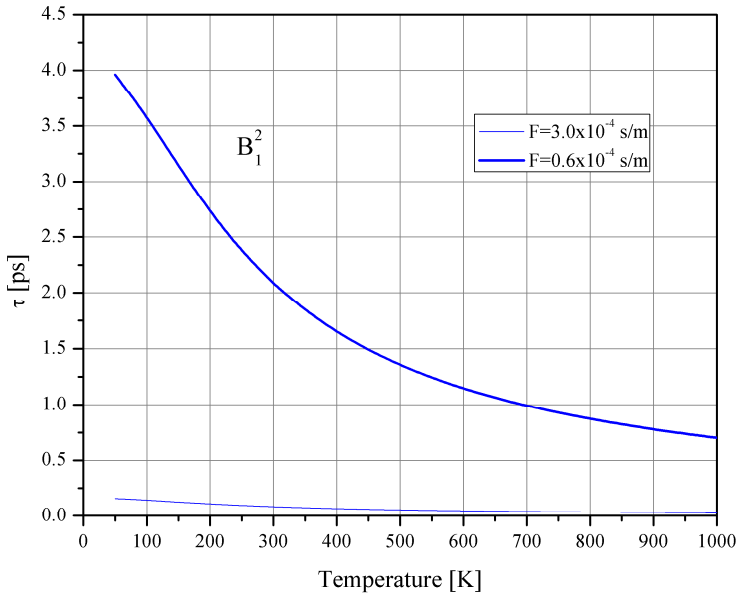

Figure 47: Temperature dependence of the B_1^2 phonon mode relaxation time.

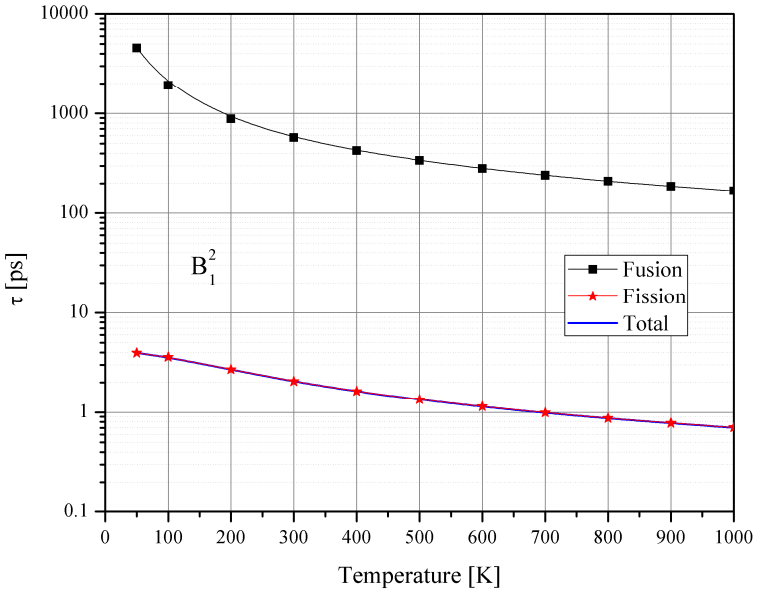

Figure 48: Contributions to the total relaxation time from both fusion and fission phonon scattering processes.

4.3.2.7 $A_1(LO)$ Mode

Experimental results for the relaxation time of the $A_1(LO)$ mode have been given in [111, 114, 115, 117]. The results from these experiments are summarized, along with the modeling results, in Figure 49. In order to fit the anharmonic parameter, the relaxation time at 300 K from Beechem *et al.* was used, as it agrees closely with two of the other references. Results from Tsen *et al.* are a factor of 3 higher than other experimental results. The data from Tsen *et al.* were determined from the time resolved non-equilibrium LO phonon signal. This method requires the fitting of a functional form of the decay process, as well as assuming phonon frequencies that the LO phonon decays into. This relaxation time extraction process is very sensitive to the fitting procedure as well as which phonon frequencies are chosen to be the surviving phonons; it is thought that this method of determining the relaxation time will be less accurate than using the energy-time uncertainty relationship. This data is therefore considered to be an outlier from the other experiments. As can be seen from the fitted model, there is excellent agreement over a wide temperature range when compared with the other experimental results.

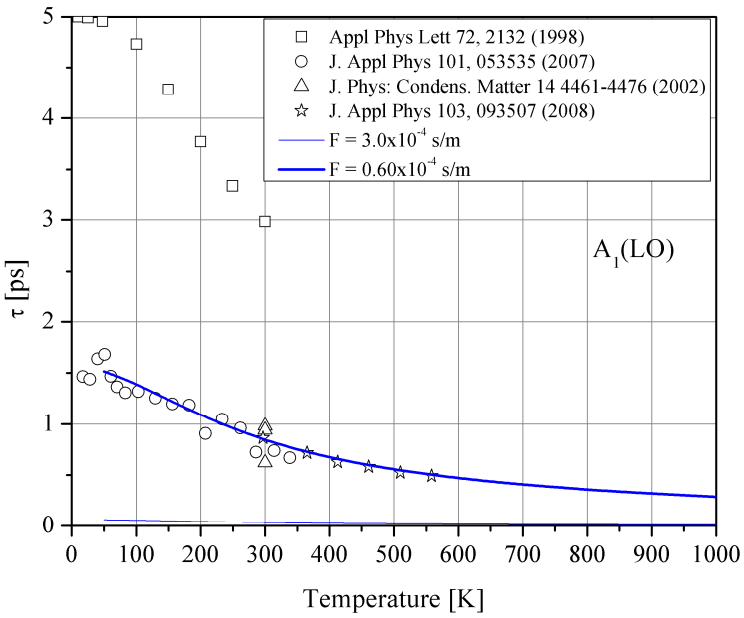

Figure 49: Temperature dependence of the $A_1(LO)$ phonon mode.

The data presented in Figure 49 is only the contribution from the fission process. It was found that the scattering rate for the fusion process was many orders of magnitude slower and therefore did not contribute to the total relaxation time. This trend is consistent with Usher *et al.*

4.3.2.8 $E_1(LO)$ Mode

Experimental studies of the relaxation time for the $E_1(LO)$ mode are available from [111, 114]. Both methods are based on an analysis of spectra acquired with a Raman spectrometer. Beechem *et al.* used the energy-time uncertainty method to calculate the relaxation time, while Song *et al.* used a procedure where the temperature dependent linewidth of the $E_1(LO)$ mode was tracked. The temperature dependence of

the linewidth was then related to the phonon relaxation time by relationship [114]. Where c is the speed of light, Γ is the linewidth in cm^{-1} and τ is the relaxation time.

$$2\pi c\Gamma = \frac{1}{\tau} \tag{4.31}$$

While both experiments resulted in relaxation times that are of the same order of magnitude, the temperature dependence of the data in Song *et al.* is much stronger when compared to that in Beechem *et al.* This difference is attributed to differences in crystal quality. Since high temperature data was only available from Beechem *et al.* the anharmonic parameter was fit to the relaxation time at 300 K from this reference. The continuing trend with increasing temperature is captured with the relaxation time model. Again, the importance of fusion processes is negligible as the scattering rate is many orders of magnitude slower than that of fission processes.

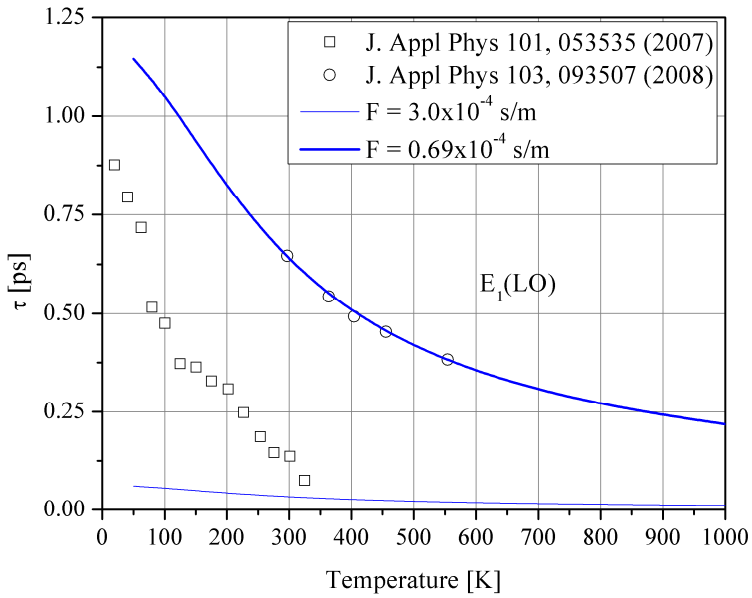

Figure 50: Temperature dependence of the $E_1(LO)$ phonon mode relaxation time.

4.3.2.9 Wavevector Dependence of Relaxation Time

From the previous sections the anharmonic parameters for all the optical modes were determined by fitting the temperature dependent trends of zone center phonons. The anharmonic parameters are summarized in Table 2.

Table 2: Summary of anharmonic parameters used in the calculations of the relaxation time.

Mode	**F [sm^{-1}]**
E_2^1	$0.975\text{x}10^{-4}$
B_1^1	$0.975\text{x}10^{-4}$
$A_1(TO)$	$0.60\text{x}10^{-4}$
$E_1(TO)$	$0.86\text{x}10^{-4}$
E_2^2	$0.415\text{x}10^{-4}$
B_1^2	$0.60\text{x}10^{-4}$
$A_1(LO)$	$0.60\text{x}10^{-4}$
$E_1(LO)$	$0.69\text{x}10^{-4}$

It is very important to study the relaxation of these zone center phonons as they are generated by Fröhlich interactions with electrons (the dominant mechanism for phonon generation in GaN). However, it is common for high electron mobility transistors to reach high biases during normal operation, where carriers are driven far from equilibrium. At these levels, deformation potential scattering of electrons can become significant as well. These intervalley scattering events involve large momentum transfer (large **q**) between the interacting particles and therefore primarily involve phonons at or near the Brillouin zone boundary. Resolving the relaxation times of these zone-boundary phonons is of critical importance when performing electro-thermal simulations of devices that are operated under biases that push carriers far from equilibrium.

In order to assess the relaxation time of zone boundary phonons Eq. (4.25) was solved along the Γ-M and Γ-A directions in the Brillouin zone. These directions correspond to the phonons along the *a* and *c* axes respectively. In presenting the anisotropic relaxation times it should be noted that the simplified optical phonon dispersion assumption was used. This assumption may artificially dampen the anisotropy; however there exists some wavevector dependence due to the anisotropic nature of the low energy phonons (which high energy optical phonons will decay into). Additionally, issues of phonon band crossings were not studied in this work. Band crossings will not affect the calculation of zone center phonon relaxation times; however there exists an opportunity that some phonon modes at arbitrary **q** will be misclassified. With these assumptions, the relaxation times are presented in Figure 51. Unlike the decay of zone center phonons, which decay primarily through N-processes, zone-

boundary phonons can undergo a range of both N and U processes. The relaxation time presented here is a combination of the two types of processes.

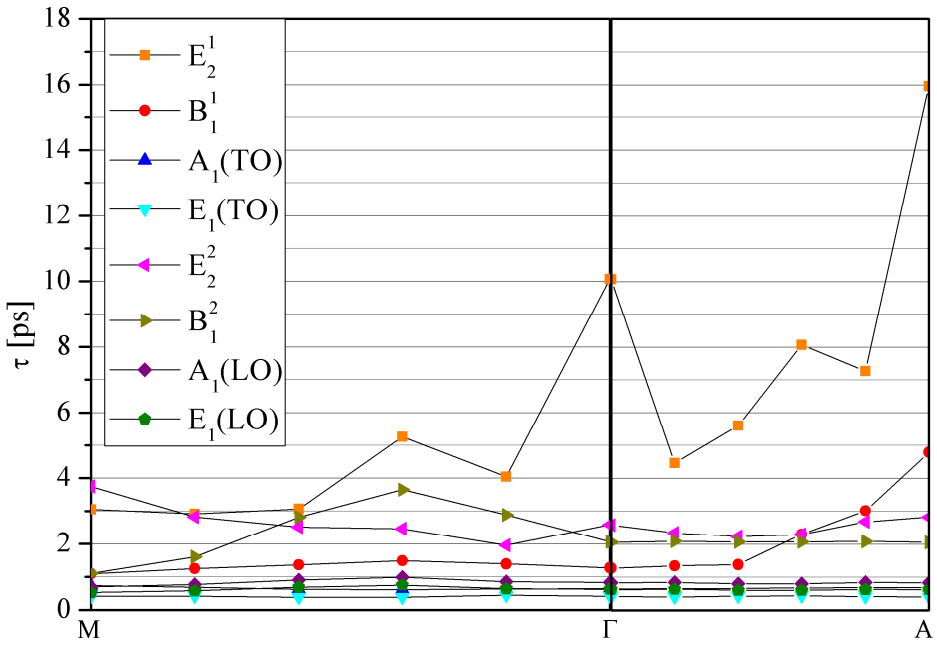

Figure 51: Anisotropic phonon relaxation times in GaN along the Γ-A and Γ-M crystal directions.

As can be seen from the above figure, there is some anisotropy that appears in the lower energy optical phonon modes. Most pronounced is the behavior of the E_2^1 mode where at a reduced wavevector of 0.5 in either direction there is a factor of 2 difference in the relaxation time. While it is known that the acoustic phonons propagate the majority of thermal energy in a semiconductor crystal, the anisotropy of the optical modes points to potential anisotropy in the acoustic modes. The relaxation times for acoustic phonons will be discussed in the next section where their anisotropy will be explored further.

4.3.3 Acoustic Phonon Mode Relaxation Times

In section 4.3.2 only a discussion of the optical phonon mode relaxation times was presented. Optical phonons are critical to consider in heat transport models since they tend to behave as an energy capacitor, due to their small group velocities and their preferential interaction with electrons. However, as will be quantified in the next section, the bulk of the thermal transport is being performed by acoustic phonons. It is therefore necessary to determine the relaxation times for all three of the acoustic phonon modes. By definition acoustic phonons at the Γ point have zero energy, and therefore the relaxation time cannot be determined by the same Raman-based methods used to characterize the optical modes. Recently a pulse-echo scheme was used to investigate the relaxation time of acoustic phonons at 380 GHz and 470 GHz [122]. At 300 K the relaxation time was on the order of 150 ps for the 380 GHz acoustic phonon and 100 ps for the 470 GHz phonon. This data, while not complete provides some insight into the behavior of low energy acoustic phonon modes.

The key unknown parameter for the acoustic phonons is the anharmonic parameter, F, just as in the case of optical phonon modes. Since adequate relaxation time data does not exist in order to fit the value of F, another method must be used. It is first noted that optical phonon modes that cluster around similar energies had similar anharmonic parameters. Following similar logic it is assumed that all three acoustic branches have the same value of F. The single value of F was then fit in order to recover the experimentally determined isotropic bulk thermal conductivity at 450 K. A discussion of this calculation is left until the next section. For all acoustic phonons a

value of 0.415×10^{-4} sm^{-1} was used in the following temperature and wavevector dependent calculations.

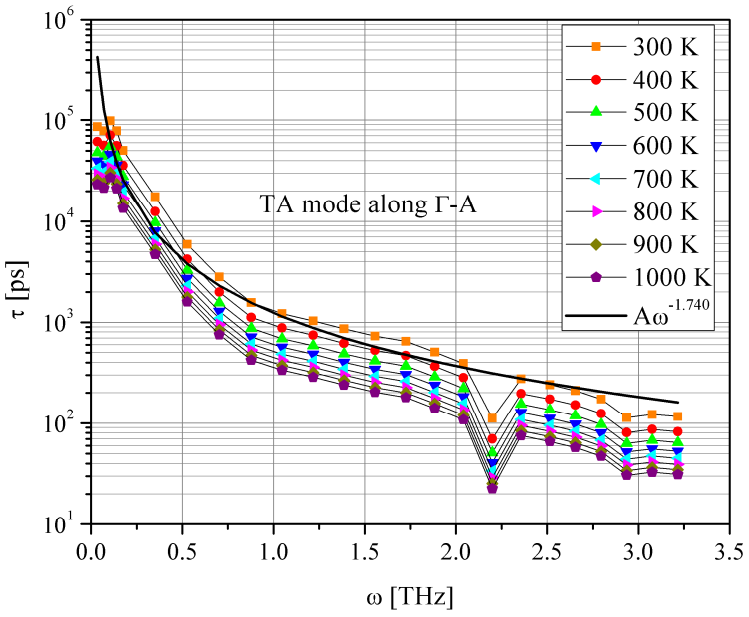

Figure 52: Relaxation times for a TA mode phonon along the Γ-A (*c-axis*) Brillouin zone direction.

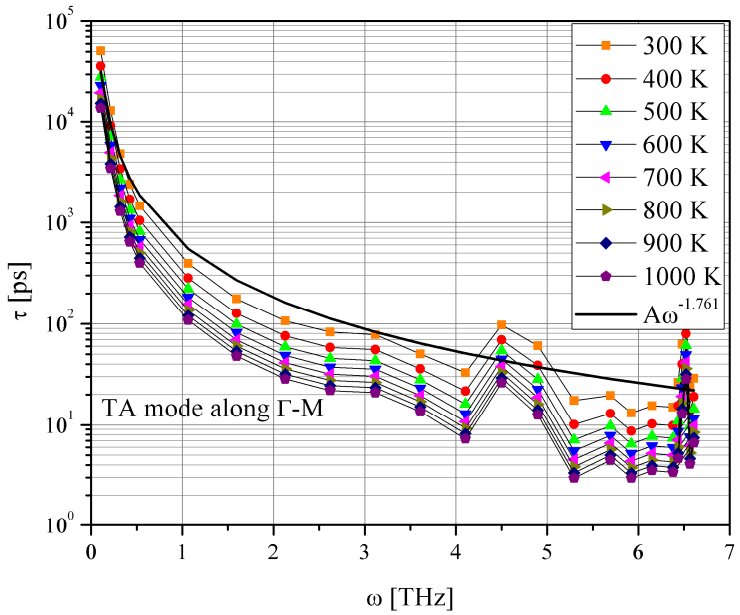

Figure 53: Relaxation times for a TA mode phonon along the Γ-M (*a-axis*) Brillouin zone direction.

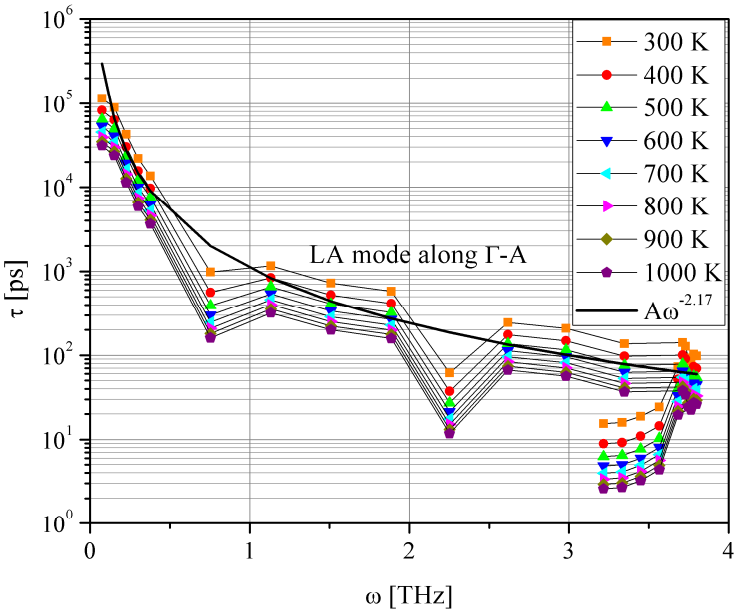

Figure 54: Relaxation times for a LA mode phonon along the Γ-A Brillouin zone direction.

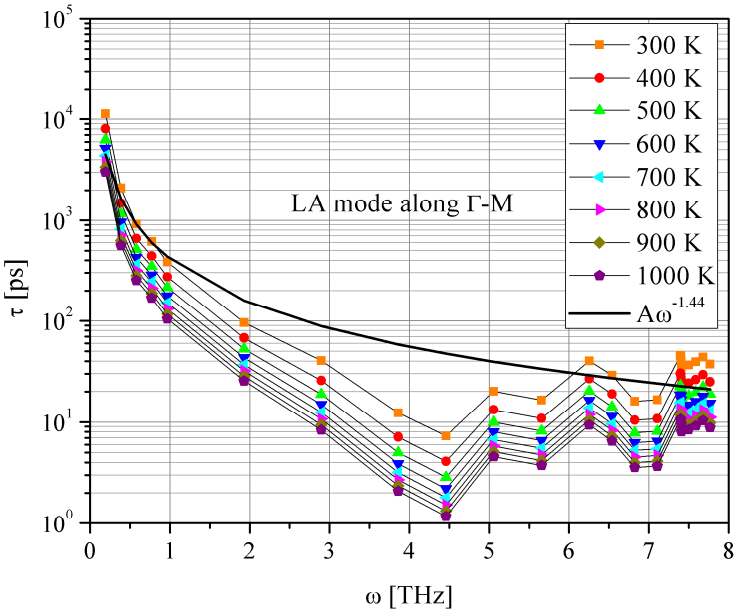

Figure 55: Relaxation times for a LA mode phonon along the Γ-M Brillouin zone direction.

In the previous figures the temperature and wavevector dependence is shown for the TA and LA phonon modes in both the Γ-A and Γ-M directions. In order to resolve the frequency dependence of the relaxation time a curve fit was performed for each of these phonon modes. The general form for the fit was $A\omega^{-n}$, and was chosen because of the general frequency dependencies outlined in chapter 2. Determining the value for *n* also provides a way to check that the calculations are capturing the underlying physical phenomena of the scattering processes. Ideally, the value of *n* would be –1 for N-processes and –2 for U-processes. The calculations shown here do not distinguish between these two types of scattering events and therefore the value of *n* is expected to be between these two idealized values. Along both directions, the TA mode's frequency dependence follows a $\omega^{-1.7}$ relationship while the LA mode (in the Γ-M direction) follows an $\omega^{-1.4}$ dependence. The values of n in each of these cases are within the expected range and therefore it is assumed that the details of the collision processes are captured throughout the Brillouin zone. The LA mode (in the Γ-A direction) has a larger frequency dependence as $\omega^{-2.17}$. This value is only slightly outside the expected range; therefore it is still assumed that the proper scattering phenomena are being resolved. Due to the anisotropic nature of the acoustic phonon modes shown in Figure 52, Figure 53, Figure 54, and Figure 55 it is expected that the final values of the thermal conductivity will also include some anisotropy. These effects will be explored more in section 4.3.3.

4.3.3 Recovery of the Bulk Thermal Conductivity

While calculating the phonon relaxation time provides useful information about the transport dynamics, it is only useful to a point since there is no guarantee that the

anharmonic parameter chosen will allow the recovery of the bulk thermal conductivity. Typical published values of the Gruneisen parameter may need to be fine tuned in order to obtain a set of realistic relaxation times. The relaxation times presented in the previous sections will allow for the recovery of the thermal conductivity; the procedure used to verify this will now be discussed.

Before approaching the results, it is necessary to outline the assumptions used to build the model of thermal conductivity given by Eq. (2.53). First, the simplified high-energy optical mode dispersion was again adopted for these calculations. The dispersionless modes consequently have a zero group velocity and therefore cannot participate in thermal transport. Low energy optical modes, those below the bandgap, are included as calculated by the Tersoff potential and therefore can contribute to the final value of the thermal conductivity. It is also assumed that all anharmonic parameters for optical modes have been fixed to match the relaxation time data found experimentally. Therefore, in order to recover the bulk thermal conductivity, only the anharmonic parameter for the acoustic modes was adjusted; this value was the same for all acoustic modes. Again, this anharmonic parameter was fit to a value 175 $Wm^{-1}K^{-1}$ which is the value of the thermal conductivity at 450 K [123]. It would be ideal to fit the anharmonic parameter to a data point at even higher temperatures to ensure that anharmonic phonon scattering events dominate the value of the thermal conductivity. At this time high temperature experimental data on the thermal conductivity of GaN does not exist. Other processes, such as those described in section 2.1.3, are ignored for this study.

In the general case the thermal conductivity is then a tensor quantity, however only bulk isotropic experimental values exist for comparison. In order to calculate the

isotropic thermal conductivity the isotropic thermal conductivity was calculated following Eq. (4.33) [43].

$$k = \frac{1}{3}\sum_{\mathbf{q}s} c_s(\mathbf{q})\left|\mathbf{v}_s(\mathbf{q})\right|^2 \tau_s(\mathbf{q}) \tag{4.32}$$

The largest computational cost encountered in calculating the thermal conductivity is in determining the unique relaxation times for all Brillouin zone mesh points. In these calculations a discretization similar to that shown in Figure 34 was used that has 768 points. Each of these 768 points has 6 branches that contribute to the final value of the thermal conductivity; 4608 unique relaxation times were then needed in order to calculate one value of the thermal conductivity. Each of these relaxation time calculations are independent of each other, therefore the calculation time can be decreased dramatically by parallelizing the code structure.

After generating sets of relaxation times for various temperatures the total thermal conductivity was calculated through the generalized kinetic theory description. While general trends for the frequency/temperature dependence of the relaxation time were resolved (4.3.2) the proper trend of the thermal conductivity has not been addressed. In the high temperature limit the thermal conductivity should be proportional to T^{-1} [31]. Other estimates of the temperature trend have been made and show a $T^{-1.2}$ dependence [105, 106]. During the fitting process the anharmonic parameter was tuned to capture the proper magnitude of the thermal conductivity. This fitting process will not change the underlying functional dependence of the collision processes. Therefore, for verification purposes, a function of the form aT^{-n} was fit, in a least squares sense, to the modeled

values of the thermal conductivity in order to extract the value n. The results of the modeled thermal conductivity are presented in Figure 56 along with several sets of measurements [124-127].

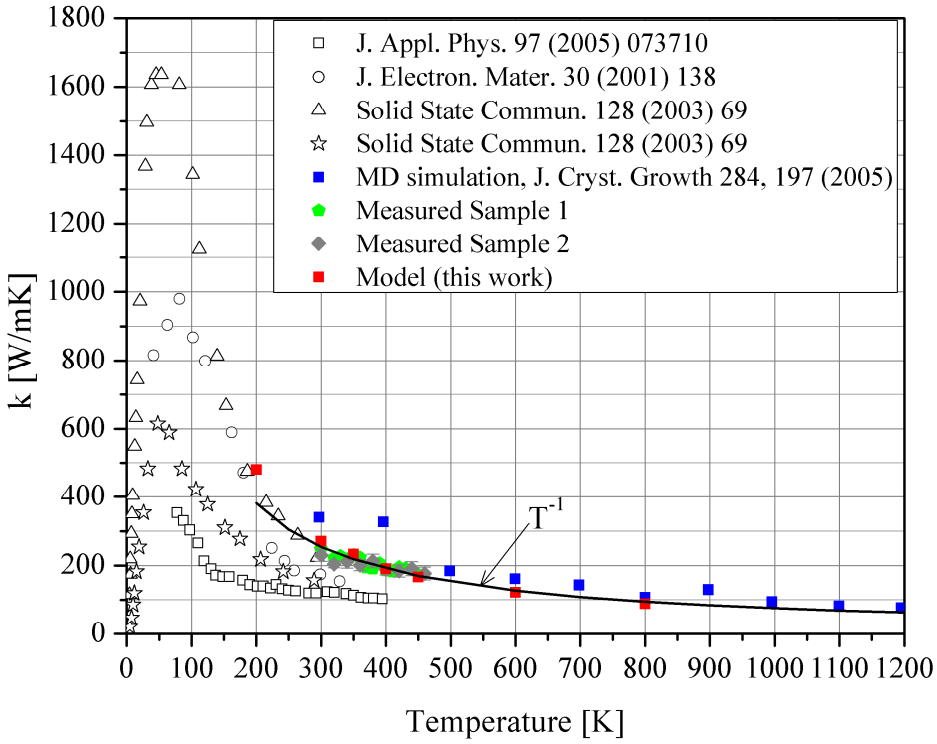

Figure 56: Thermal conductivity as a function of temperature for several measured samples as well as predicted values from recent molecular dynamics simulations. Red squares, represent modeled values of the thermal conductivity from this work. Measured samples 1 and 2 are from [128].

As can be seen from Figure 56 there is good agreement with the modeled thermal conductivity values and experimentally determined values. The functional dependence of the thermal conductivity, at high temperatures, is shown to follow a T^{-1} relationship as predicted by high temperature theoretical limits.

In resolving the correct thermal conductivity temperature dependence it is now possible to study some of the phonon-level details that contribute to the total thermal conductivity value. As hypothesized previously, the acoustic modes do contribute the most to the total thermal conductivity (~95%). The remaining 5% of the thermal conductivity is due to low energy optical modes. This trend is unchanging across a wide range of temperatures as shown in Figure 57.

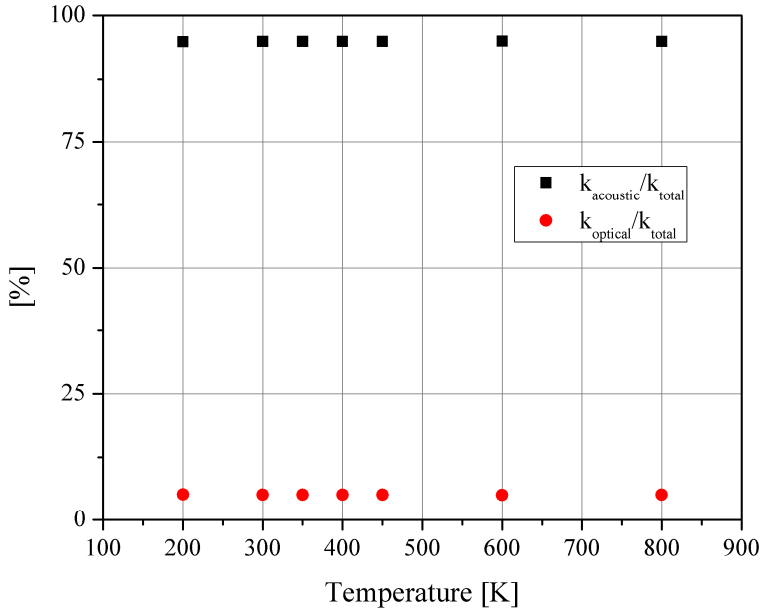

Figure 57: Contributions to the total thermal conductivity from all acoustic and optical modes.

In addition to investigating the contributions from optical/acoustic phonon modes it is also possible to investigate the thermal conductivity as a function of mean free path. In this way it is possible to investigate which phonon populations contribute the most to the thermal conductivity. Additionally, as many transport simulations also rely on mode averaged relaxation times (and therefore mode averaged mean free paths) it is possible

probe the effectiveness of these estimations. The mean free path distribution function is shown in Figure 58 and shows that there is a peak in the number of phonons that have mean free paths on the order of ~2 nm at 300 K. Also shown in Figure 58 is the thermal conductivity accumulation function. This function describes the cumulative percentage contribution that each mean free path value adds to the total thermal conductivity.

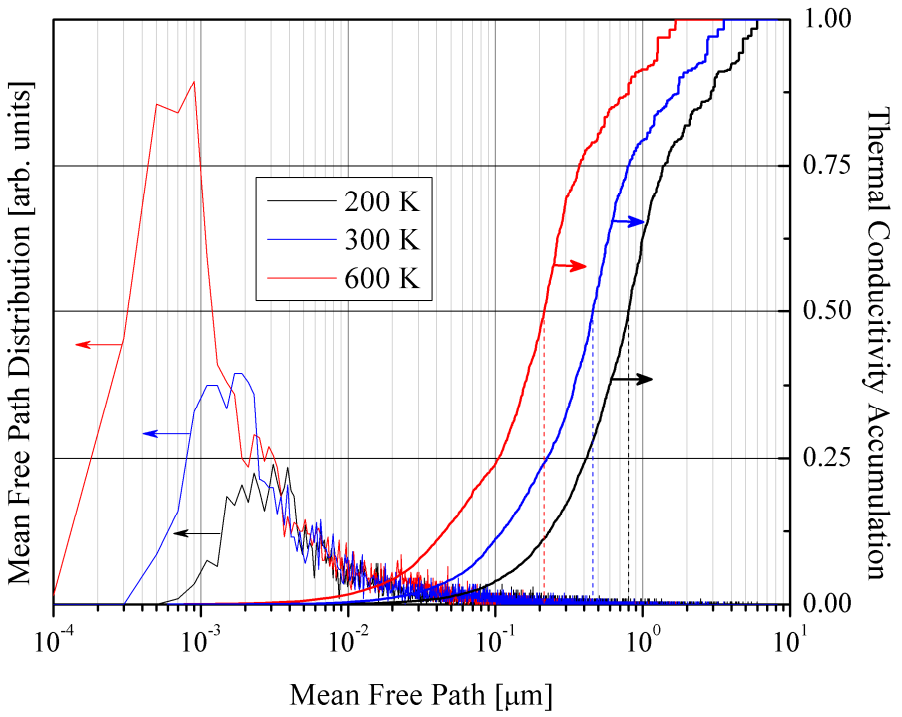

Figure 58: Mean free path distribution function and the thermal conductivity accumulation function.

When the two distributions are overlaid it is seen that phonons with small mean free paths contribute very little to the total thermal conductivity. It is primarily phonons with mean free paths >400 nm that contribute to the bulk thermal conductivity (up to 50%) at 300 K. When phonons with mean free paths >50 nm are considered their total contribution is ~90% of the total thermal conductivity. This finding reinforces the notion

that phonons with long mean free paths contribute in a disproportionate way to the total thermal conductivity.

4.3.4 Anisotropy

The data presented in Figure 56 is the isotropic bulk thermal conductivity. However, with the developed relaxation time models it is possible to investigate anisotropy within the GaN crystal by using Eq. (2.53) instead of Eq. (4.32). Due to the hexagonal crystal structure the anisotropy is typically presented as a ratio of the transport along the *a* axis to that along the *c* axis (k_a/k_c). This ratio as a function of temperature is shown in Figure 59.

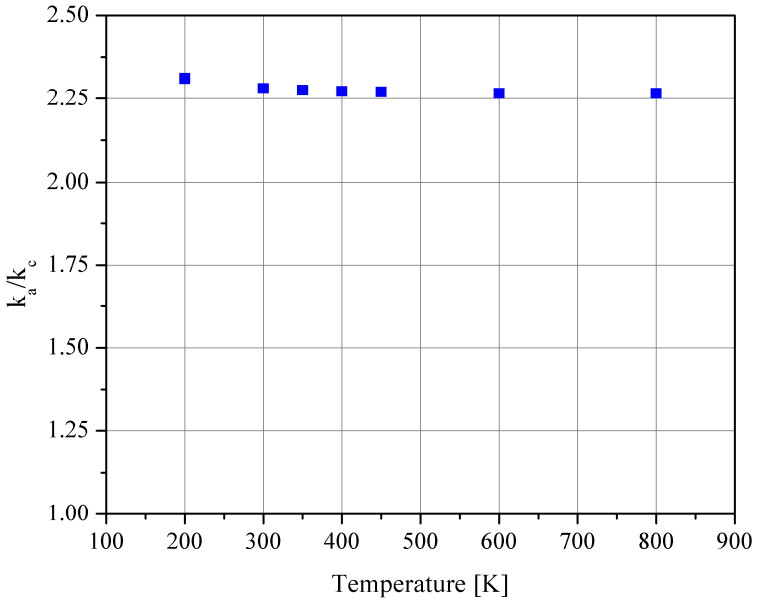

Figure 59: Anisotropy ratio as a function of temperature for wurtzite GaN.

The absolute thermal conductivity values along the *a* and *c* axes are shown in Figure 60.

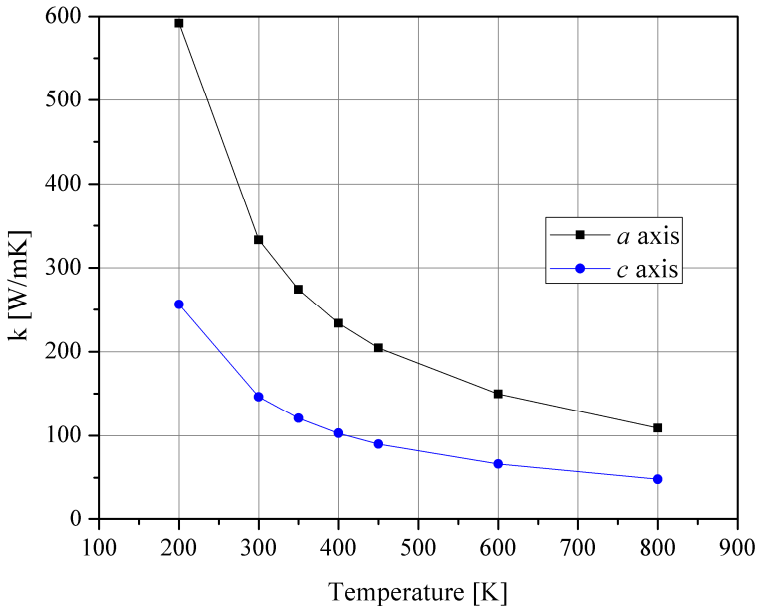

Figure 60: Absolute thermal conductivity values along the *a* and *c* axes in wurtzite GaN.

The results from the previous two plots show that the anisotropic ratio is on the order of 2.2. Recently a molecular dynamics study was performed where the anisotropic ratio was found to be 0.78 at 500 K and 0.81 at 800 K [99]. While the MD results show that the *c* axis thermal conductivity to be larger, the estimated error in the simulations could put the k_a/k_c ratio as high as 1.11 at 500 K. The discrepancy between these results is thought to be due to issues of band crossing within the phonon dispersion curves, particularly within the LA mode. As can be seen in Figure 54 there is a portion of the relaxation time curve that folds back under the initial trend. This folding could be due to a band cross point that would then artificially increase the anisotropy ratio. This band crossing effect would also effect the calculation of the phonon group velocity at these points, and may also contribute to an artificially high anisotropy ratio. At this point, a detailed account of band crossing effects has not been attempted and is recommended as an area of future work.

4.4 Summary

The calculations performed in the previous sections lay the foundation for which thermal transport in GaN was studied. To summarize, for each phonon mode the temperature and wavevector dependence of the relaxation time was quantified and verified against experimental measurements (for optical modes only). In studying the acoustic modes the anharmonic parameter was tuned in order to recover the proper bulk isotropic thermal conductivity. The resulting values of the isotropic thermal conductivity followed the proper high temperature trends. These bulk values of thermal conductivity were then decomposed into distribution functions based on phonon mean free path. By decomposing the thermal conductivity into this distribution function, additional insight into the nature of thermal transport is gained. The chapter concludes with a brief discussion of the anisotropic nature of thermal transport in wurtzite GaN.

CHAPTER 5

MULTISCALE DEVICE MODELING

In the previous chapter a framework has been constructed in which to study the relaxation time of a phonon. This parameter is one of the key components in developing a transport model that can then be used to solve for the temperature distribution in an operating device. As mentioned previously, a multiscale transport approach will be investigated for modeling devices, as it can allow for larger computational domains to be solved. The chapter will be organized around the two primary devices that were investigated in this study. The first device was a silicon beam that had been doped in a small region; this doped region was the heat source. The second system is a 6 finger GaN HEMT built upon a silicon carbide substrate. After introducing the device, the details of the modeling methodology will be outlined and all assumptions will be discussed. The chapter will then conclude with a short discussion of the computational requirements necessary to solve these systems.

5.1 Silicon Suspended Beam

The first device that was modeled was based off of a suspended silicon device in [129]. This was one of the first experimental investigations to quantify the role that both ballistic phonon transport and optical phonons play in the total thermal resistance of a device. The device under test in this study was a suspended silicon film with the dimensions shown in Figure 61.

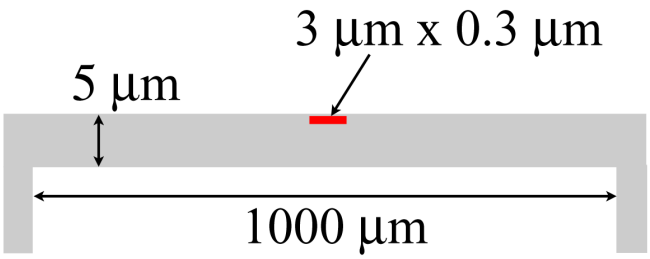

Figure 61: Cartoon of the suspended silicon beam used in [129]. The red spot indicates the location of a p-type doped resistor; this is where heat is being generated in the system

The doped resistor, once calibrated, acted as both the primary heater and temperature probe at the hot spot location. In addition to the doped resistor shown in the previous figure, aluminum wires were evaporated onto the top surface of the device. These small wires, allowed for the measurement of temperature at locations along the length of the suspended beam. This was important, since with this information, the thermal conductivity of the silicon could be verified simultaneously. The experiments were carried out at temperatures that ranged from 100-300 K. Knowing the power dissipated into the device and the temperatures of both the hot spot and ambient conditions, it was possible to calculate the total thermal resistance of this device. At room temperature an estimate of the phonon mean free path in silicon is approximately 300 nm [59]. However, as the ambient temperature decreases to between 100-200 K, the mean free path is expected to increase dramatically to between 2-10 µm [129]. Due to the increase in the phonon mean free path at low temperatures the Knudsen number changes from 0.06 (diffusive transport) to 2 (ballistic transport). It is therefore expected that at low temperatures there may be a significant deviation from diffusive-type simulations. These deviations would then be caused by a significant amount of boundary scattering. During the experiment, a reduced thermal conductivity was determined directly from the

aluminum temperature probes. This reduced value of the bulk thermal conductivity inherently includes boundary scattering, and is similar to the effects seen in Figure 15. The proper thermal resistance could not be captured even if this reduced thermal conductivity parameter within a diffusive transport model. This indicates that other effects might be present that are not described in the transport model. Sverdrup *et al.* included effects of optical phonons through a two-fluid model and were able to recover the proper thermal resistance experienced in experiments.

This experimental data was then used in order to verify the coupled Lattice Boltzmann/finite difference solver. The experimental system shown in Figure 61 was approximated as illustrated in the following figure.

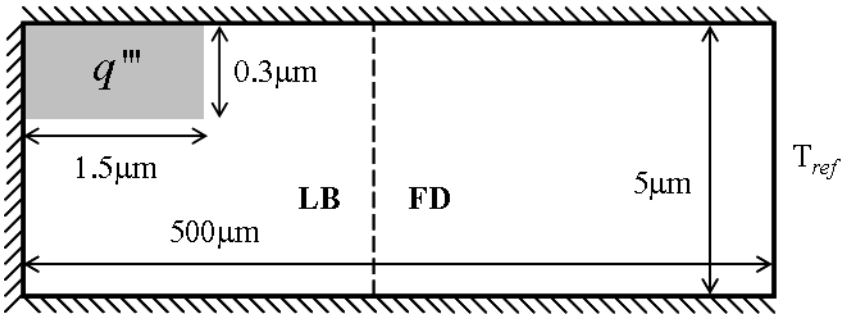

Figure 62: Simplified domain used to model the experimental structure. The dashed line represents the division of the Lattice Boltzmann and the finite difference domain.

As a test of the method introduced, a simulated device was modeled using the both the gray phonon model and a two-fluid model and then compared to previously published experimental results [129]. As discussed earlier the two-fluid model simulates the interaction between the zero-velocity optical phonons with long relaxation times and the propagating acoustic phonon modes [58, 61, 130]. A critical component to the two-fluid model is the knowledge of the optical and acoustic phonon modes' contribution to the

total specific heat. In order to calculate the contributions of the optical and acoustic phonons the Debye model was used. The contribution from one acoustic branch is [35].

$$c_a = \frac{k_b^4 T^3}{2\pi^2 \hbar^3 v_g^3} \int_0^{\theta_D/T} \frac{x^4 e^x}{\left(e^x - 1\right)^2} dx \tag{5.1}$$

At room temperature it has been assumed that the majority of the heat is being carried by the LA phonon mode as in [61]. As the simulation temperature is decreased below 300 K the TA phonons begin to dominate [65]. The specific heat given here is calculated over an average LA phonon group velocity of 6400 m/s. This value, given by Holland, provides a good estimate of the average velocity for the all LA phonons. The Debye temperature was taken as 570 K, also provided by Holland [44]. By choosing a lower Debye temperature the effects of the optical phonons are not included in Eq. (5.1). In order to calculate the contribution from the optical phonons the total specific heat was calculated with a Debye temperature of 623 K. Using this Debye temperature the total specific heat was found to agree well with experimental data. The specific heat contribution from the optical phonons was found from subtraction of the total specific heat and that part that is due to the dominant phonon mode. Another critical component of the two-fluid model is the relaxation time used in the LBKE. For these simulations, the relaxation time was calculated from $k = 1/3 c_p v^2 \tau$. The specific heat in this expression was calculated using an average phonon velocity over each of the acoustic branches. Following Sverdrup *et al.*, the low frequency TA and LA phonons have been assumed to not carry as much energy as their high frequency counterparts [59]. The primary reason

for this is that the phonon occupation number approaches zero as the frequency approaches zero. Therefore it is assumed that in order to calculate the relaxation time the group velocity for the high frequency TA and LA should be used. This methodology allows the recovery of the bulk thermal conductivity in large domains. The parameters used for this experiment are summarized in Table 3.

Table 3: Table of properties used in the two-fluid model simulations.

T (K)	k ($Wm^{-1}K^{-1}$)	c_P ($Jm^{-3}K^{-1}$)	c_R ($Jm^{-3}K^{-1}$)	v(ms^{-1})	τ(ps)
100	884	$1.293x10^5$	$0.379x10^6$	2000	5126
150	409	$1.450x10^5$	$0.849x10^6$	2000	2115
200	264	$1.512x10^5$	$1.180x10^6$	2000	1309
300	148.3	$3.106x10^5$	$1.3730x10^6$	4240	79

More details of the equations solved for the two-fluid model have been provided in Chapter 2, however there are some modifications that are necessary due to the coupling interface that will be explained here [60, 61]. A modification to must Eq. (2.46) be made to reflect the fact that only acoustic phonons are assumed to be propagating. In the two-fluid model the equilibrium energy is given by Eq. (5.2).

$$e^o = c_P \left(T_L - T_{ref} \right) \tag{5.2}$$

Here, T_L represents the lattice temperature that can be calculated as a weighted average of the reservoir mode temperature and the propagating mode temperature as defined in Eq. (2.50). This modification results in the missing distribution functions at the coupling interface to have the form of Eq. (5.3).

$$e_i(x,t) = w_i\left[c_P\left(T_L - T_{ref}\right) - v_i\tau c_P\nabla\left(T_L - T_{ref}\right)\right] \tag{5.3}$$

Using the modeling methodology outlined here the doped suspended silicon membrane found in [129] was modeled. Originally, this device was fabricated in order to experimentally investigate the impact of non-equilibrium phonons on the overall heat transfer in the material. As previously mentioned the average mean free path in silicon is 41 nm at room temperature, but as the ambient temperature is decreased the mean free path increases due to the temperature dependence of the relaxation time. In the experiments the suspended silicon membrane was cooled to 100 K where the mean free path is on the order of 30 μm. At this point the dimensions of the device are smaller than the mean free path and as a result there is significant phonon scattering at the boundaries that cause a decrease in the effective thermal conductivity. Measurements of this effective thermal conductivity were made simultaneously during device operation and values of the thermal resistance were calculated. It was shown that including the effects of boundary scattering did not recover the full value of the device thermal resistance. However, good agreement was seen between the experimental results and a Monte Carlo based two-fluid phonon model; that included the effects of both boundary scattering and non-equilibrium optical phonons. This result highlights the importance of considering optical phonon transport effects when modeling devices. In this work, the coupled LB/FD model was used to model the heat transfer through the silicon membrane. The coupled technique was used along with symmetry conditions to minimize the total computational load and the results were compared to experiments to further verify the method.

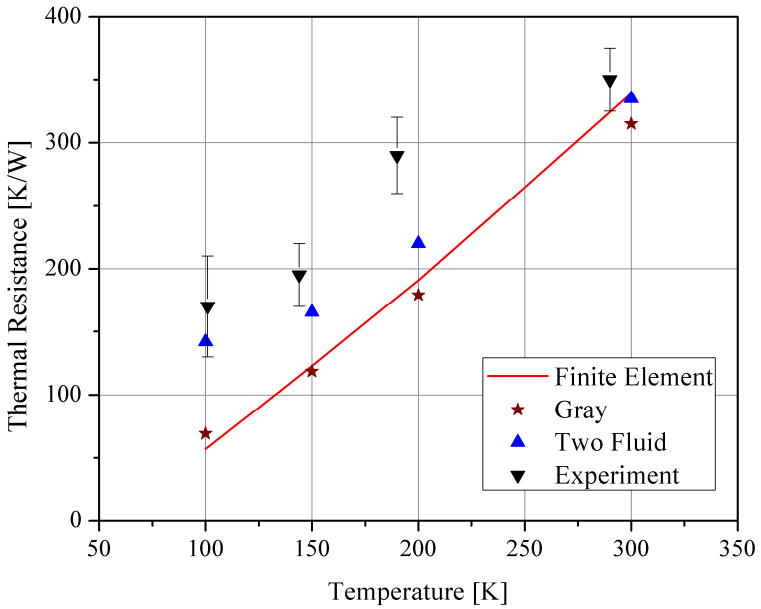

Figure 63: Data from [129] and predictions made with several modeling methodologies.

For the data points at 200K and 300K the phonon MFP is small enough to justify using the bulk thermal conductivity for the FD region calculations. At temperatures lower than this the MFP is large enough that the boundaries of the 5μm thick device begin to impact the behavior of the phonon transport. Therefore, and intermediate step is needed to calculate an effective thermal conductivity that can then be used to quantify the transport in the FD region. This effective thermal conductivity can be calculated by defining a 2D LB domain and imposing a temperature difference, then using the relationship $k = q"\left(\partial T/\partial x\right)^{-1}$. Data in Figure 63 has been calculated considering these effects. For comparison a standard finite element model was created. Within this model only the bulk thermal conductivity of silicon has been used. The experimental data show a clear deviation from this modeling methodology due to ballistic phonon transport that is introduced by lowering the device temperature. Using the gray model it was still not possible to capture the departure of the thermal resistance from Fourier models. Only

with a simplified picture of the phonon dispersion was the departure from traditional models captured. It is important to note that the two-fluid model, while providing a more physical picture of phonon transport, should not be assumed perfect. Pop *et al.* have shown through Monte Carlo simulations that high energy electrons, while they do interact preferentially with optical phonon modes, there is some direct emission of acoustic modes [17].

5.2 GaN HEMT Modeling

5.2.1 Gray Phonon Model Material Properties

The key input parameter for the LB model is the phonon relaxation time. In this work the relaxation time has been calculated from the kinetic theory description of the thermal conductivity, $k = (1/3) c_P v^2 \tau$. This method of calculating the relaxation time implicitly assumes that all phonons all have a single group velocity; this approximation is commonly called the gray phonon assumption. At room temperature, high quality GaN has a thermal conductivity of 250 $Wm^{-1}K^{-1}$ [125] and a volumetric heat capacity of 3.013×10^6 $Jm^{-3}K^{-1}$ [131]. An averaged phonon group velocity was found from dispersion curves in the Γ-A direction; a value of 4959 ms^{-1} was calculated. This direction corresponds to phonons traveling along *c* axis of the unit cell, which also corresponds to the epitaxial growth direction. With these material parameters the relaxation time for GaN was 10 ps; the mean free path is then approximately 50 nm. By calculating the relaxation time through the kinetic theory formula it is guaranteed that the correct bulk thermal conductivity is recovered. The thermal conductivity of SiC at room temperature

was assumed to be 330 $Wm^{-1}K^{-1}$ [132] and its volumetric heat capacity was assumed to be $2.22x10^{6}$ $Jm^{-3}K^{-1}$ [131].

5.2.2 Two-Fluid Phonon Model Material Properties

As discussed in Chapter 2, the two-fluid phonon model breaks the total population of phonons into two groups; a low energy propagating population as well as a non-propagating high-energy population. The dynamics of the non-propagating phonons cause them to act as an energy reservoir. The main equations were presented as Eqs. (2.47), (2.48), (2.49), and (2.50) [60]. The relaxation time in the two-fluid model is again calculated from a kinetic theory description of thermal conductivity. With the added model parameters it is worth discussing how values were chosen. From inspection of the GaN phonon dispersion curves it can be seen that phonon modes above the phonon bandgap have a near zero group velocity. These modes are therefore considered to be stationary ($v_g = 0\ ms^{-1}$). Modes below the phonon bandgap have a non-negligible group velocity. To clarify, the propagating low energy phonon modes in GaN include both acoustic and optical modes, unlike silicon where it is usually assumed that only acoustic phonons propagate energy. Since a mix of several phonon modes help propagate energy, a weighted average group velocity was calculated for all low energy phonons throughout the entire Brillouin zone. The group velocities were calculated through the relationship in Eq. (2.17) utilizing a finite difference approximation to the gradient term. The normalized occupation number was then used to determine the averaging weights; the occupation number is shown in Figure 30 for several temperatures. This procedure results in a velocity that is a representative average over all propagating phonon modes. For device temperatures of 300 K the average group velocity was found to be 2671 ms^{-1}.

This averaging scheme eliminates the need for assumptions regarding the dominant phonon propagation direction and speed.

The other key parameters for the two-fluid model are the specific heat contributions from the high energy modes as well as the low energy modes. In order to calculate the specific heat contribution from these two populations a direct summation over the Brillouin zone was performed. The total specific heat can be calculated through Eq. (2.20). The results of the summation are shown Figure 64.

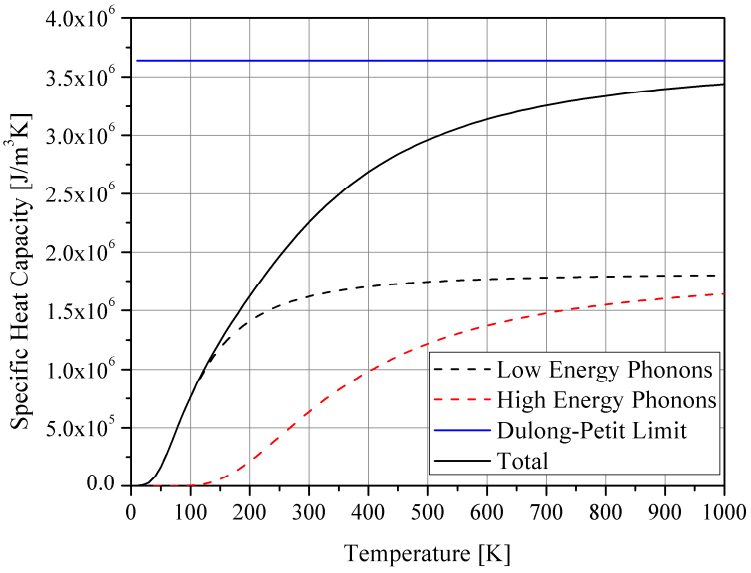

Figure 64: Temperature dependent specific heat contributions from low energy (propagating) phonons as well as high energy (non-propagating) phonons.

All device simulations in this work were performed at 300 K, therefore the propagating modes' specific heat was calculated to be 1.6183×10^6 $Jm^{-3}K^{-1}$; the non-propagating modes' specific heat was calculated to be 6.3635×10^5 $Jm^{-3}K^{-1}$. In calculating the specific heat slight deviations from experiments arise and are attributed to inaccuracies in modeling the high energy phonon modes through the Tersoff potential as highlighted

earlier [91]. From the kinetic theory description of the thermal conductivity it is then possible to approximate a phonon relaxation time. The bulk thermal conductivity of GaN was again assumed to be 250 $Wm^{-1}K^{-1}$, leading to a relaxation time of 65.5 ps and a mean free path of 174 nm. This calculated value of the mean free path is one the same order of magnitude as the dimensions of the hot spot; therefore non-equilibrium phonon transport effects are expected.

5.2.3 Mean Free Path Calculations

Since a detailed analysis of the phonon properties was presented in Chapter 4 it is possible to evaluate the feasibility of the mean free path calculations for both the gray and two-fluid models. From Figure 58, the average mean free path is approximately 450 nm. This mean free path value corresponds to the point where the thermal conductivity accumulation function equals 0.5. The gray model, with an estimated mean free path of 50 nm, under estimates the average mean free path by a factor of 9, and therefore may under predict some of the ballistic transport effects that occur in the material. The two-fluid model (estimated mean free path = 174 nm) also under predicts the average mean free path by a factor of 2.58. While the two-fluid model may still under predict the true mean free path, the nature of the phonon transport will be much closer to the real material behavior than the gray model can predict. The two-fluid model, however, still over predicts the optical phonon mode's relaxation time and ultimately can over predict the effective temperature in a device, as will be discussed in

5.2.4 Device Specifications

A 6 finger GaN device was developed that included a 2 μm thick GaN layer that had been grown on a 100 μm thick SiC substrate, the gate spacing was 50 μm and the

gate length was assumed to be 370 μm long. The device can be seen in Figure 65; blue areas in the figure designate the LB sub-domain locations.

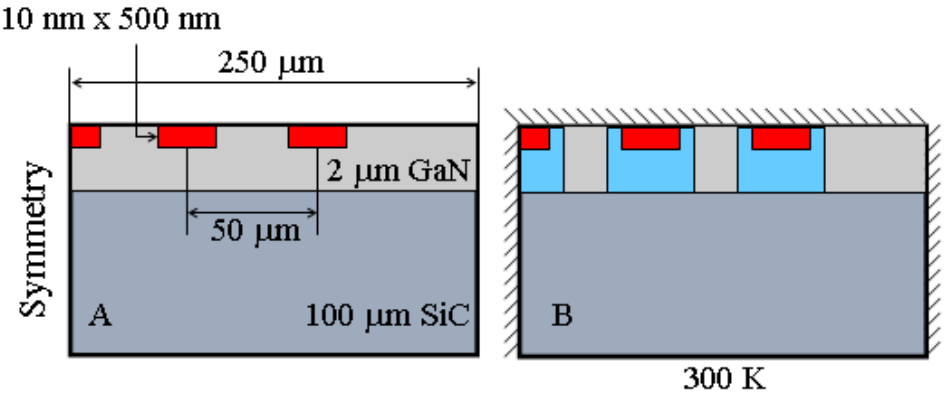

Figure 65: (A) Dimensions of the 6 finger GaN HEMT; a symmetry line has been used in order to simplify the diagram. (B) Boundary conditions for the thermal simulation, hashed boundaries are adiabatic in nature. Adiabatic boundaries in the LB region are assumed to be diffuse phonon reflectors. Shaded areas around the hot spot designate the LB domains that are embedded within a finite difference domain. Pictures are not to scale.

All boundaries of the simulation domain were assumed adiabatic except for a constant temperature (300 K) boundary on the bottom side of the SiC substrate. All adiabatic boundaries for the LB sub-domains were assumed to be diffuse scattering surfaces except along the symmetry line, where a specular surface was enforced. At distances far (>10Λ) from the hot spot diffusive heat transport is recovered; non-diffusive transport is then isolated within the vicinity of the hot spot. Following this modeling methodology, an LB region was centered on each gate contact that measured 2 μm x 2 μm for the gray phonon model and 6 μm x 2 μm in the two-fluid model. This region was coupled to a larger FD domain that handled macroscopic heat transfer through the rest of the system. As a result of the LB sub-domain size there is a shared interface between the LB GaN region and the

FD SiC region. The phonon transmission across the interface has been assumed to be perfect between the two materials. However, due to the complex crystalline structure (large dislocation densities) that exist at the interface it has also been assumed that all interface phonons are in equilibrium. Heat generation within the device was handled by defining a volume within the LB regions. These generation regions effectively behave as phonon sources; there were no energy sources within the FD regions. These phonon sources were estimated to be 10 nm deep by 500 nm wide, as shown for a simulated V_{ds} of ~25V [133].

5.2.5 Mesh

Due to the nodal spacing requirements enforced by the LB regions a non-uniform rectangular FD mesh was used in order to describe the heat transfer throughout the rest of the system. In order to help minimize the computational demand within the FD region a grid expansion method was used at the interface of the two domains, in all simulations the expansion ratio was 5:1. A detailed view of the mesh at the interface of the LB and FD regions is shown in Figure 66.

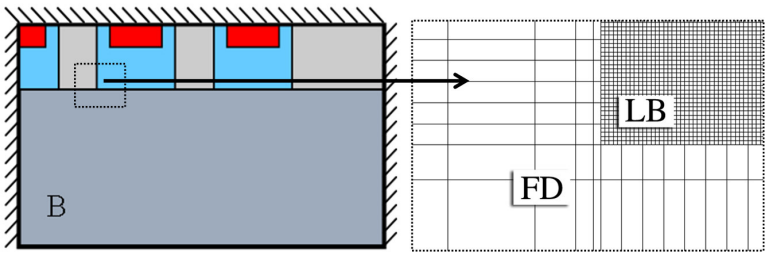

Figure 66: Detailed mesh view at the coupling interface.

5.2.6 Simulation Results

Simulations were performed for several device powers in order to probe the temperature response of the device. The coupled LB/FD simulations were also compared against traditional finite element solutions to probe any differences that may arise. The results are shown in Figure 67.

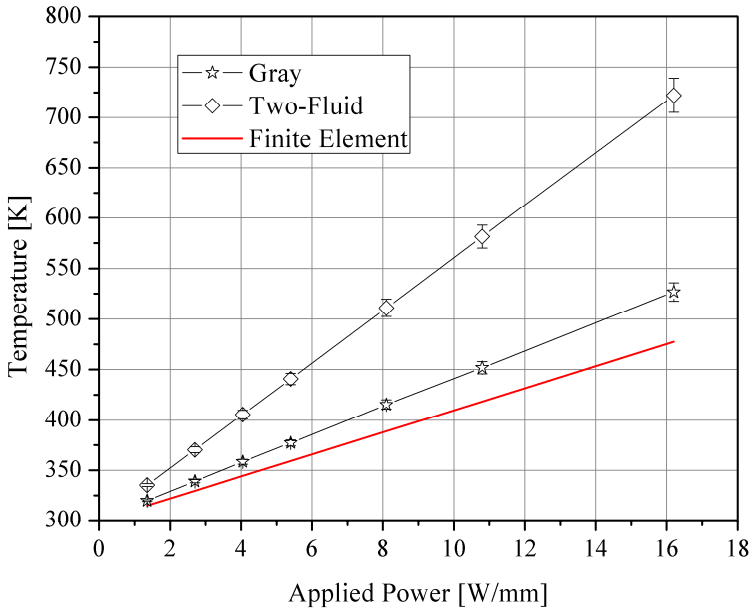

Figure 67: Trend of maximum device temperature with total dissipated power.

Error bars have been added to the simulation data and reflect the error based on the lattice spacing. The lattice spacing results in an error of approximately 4% in the maximum temperature rise experienced in the device. The results from both the gray and two-fluid models of the coupled LB/FD simulation are plotted against a standard finite element simulation for comparison. Recall that the phonon relaxation time, in both models, was calculated in order to recover the bulk thermal conductivity. Therefore in a macroscopic domain, as is modeled here, the temperature distribution should intuitively approach the diffusive solution. However, both phonon models are subject to confinement effects

within the hot spot that contribute to the deviation from diffusive modeling methods. Additionally, the hot spot is in the proximity of a diffuse scattering surface. The diffuse surface acts to hinder transport away from the hot spot due to the phonon relaxation process the occurs. The combinations of these two effects are further supported by the data in Figure 68. Agreement is seen between a finite element model and the LB/FD simulation at points far from the hot spots. Confinement and boundary effects are localized around the hot spot, where the largest deviations in temperature occur. A detailed view of the temperature distribution around the second gate is shown in Figure 69.

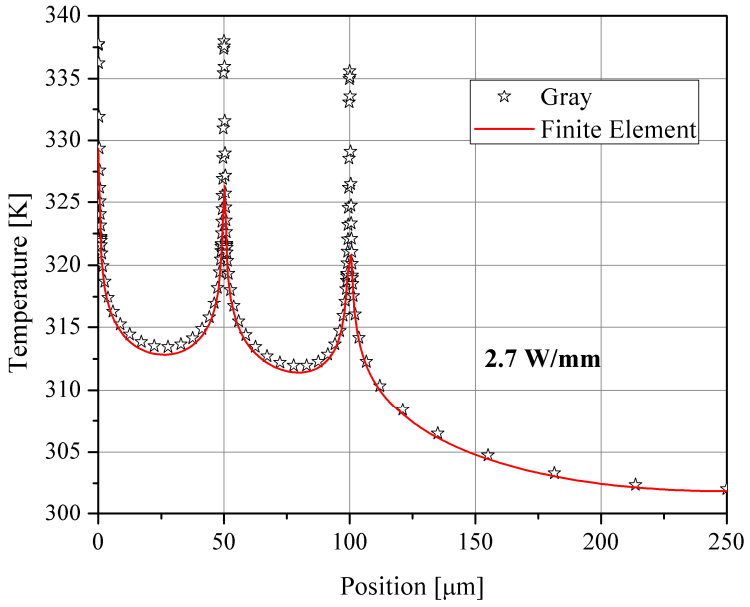

Figure 68: Temperature distribution along the top surface of the HEMT dissipating 2.7 W/mm

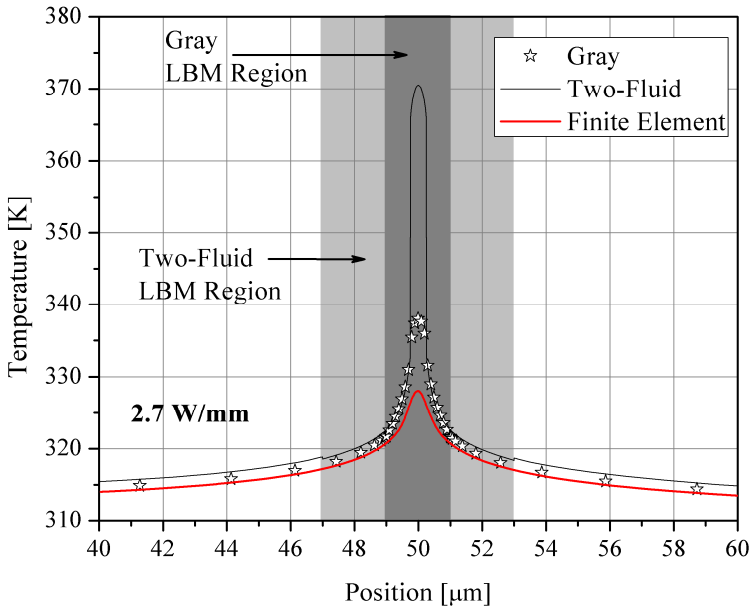

Figure 69: Temperature distribution detail around second gate. The gray shaded regions show the extent of the LB domain.

The temperature deviations outside of the hot spot are also seen in Figure 70 through the thickness of the GaN layer. As expected, the solution within the LB region converges to the finite element solution at large distances away from the hot spot.

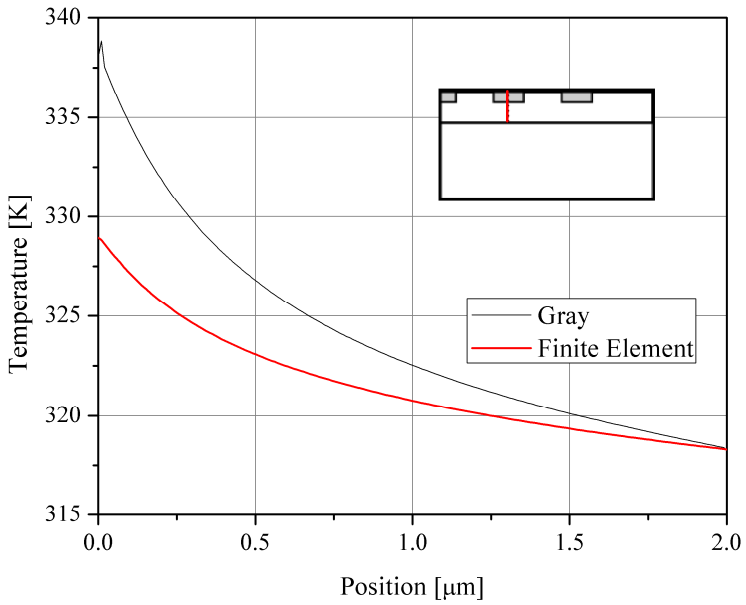

Figure 70: Temperature distribution detail through the thickness of the GaN layer as shown in the inset. Data is plotted from within the LB sub-domain only.

Regarding the two-fluid model, additional deviations from the gray phonon model are due to the non-propagating nature of the optical phonon branches. While this deviation is expected, the proper magnitude of this deviation is difficult to assess. It has been discussed with regard to silicon devices that the relaxation time calculated with the two-fluid model is an order of magnitude larger than experiments have determined [61]. This trend continues in the GaN material system as recent Raman spectroscopy experiments have measured the lifetime of LO phonon modes to be ~1-3 ps [98, 111, 114, 115]. The relaxation time used in the two-fluid model artificially emphasizes the energy bottleneck that occurs and results in excessive temperature predictions. Since the proper magnitude of the temperature rise is difficult to establish, it is desirable to determine bounds on the temperature under different phonon models. With the stationary high energy optical modes and over estimation of the relaxation time it is proposed that the two-fluid model

may provide an upper bound on the temperature rise while the gray phonon model may be a lower bound for this problem.

5.2.7 Summary

The calculations in the previous sections represent computational applications of the Lattice Boltzmann and the multiscale coupling methods. The results focused initially on verifying experimental data gathered from an experimental study with a suspended silicon beam. These studies served to benchmark and verify the multiscale method. Applications of the multiscale technique were then made to a more advance device structure, namely an operating 6 finger GaN HEMT. In these simulations the predicted temperature rise was calculated under a gray (dispersionless) phonon model as well as a simple, two-fluid type dispersion model. In both cases the calculated phonon relaxation times were compared back to quantities calculated in Chapter 4. The chapter concluded with a discussion of the assumptions within each of the models. It was proposed that the two-fluid may be an upper bound on the temperature rise while the gray phonon model may be a lower bound.

CHAPTER 6

CONCLUSIONS AND FUTURE WORK

6.1 Summary of Work

The work presented here addresses concerns about the thermal response of high power GaN electronic devices and the affects that temperature may have on device reliability. The computational models that were developed quantify the temperature distribution within an operating device from a multiscale point of view through the coupling of the Boltzmann transport equation and the energy equation. Previous thermal simulations presented in literature have primarily focused on a simplified picture of phonon transport or have been limited to small domain sizes that then rely on simplified boundary conditions. The multiscale solution method allows for a balance to be struck between computational load and details of the phonon transport physics. Several benchmarking tasks were needed in order to understand the numerical behavior of both the coupling method as well as the Lattice Boltzmann method itself. Contributions were made in the following areas:

- Verified the Lattice Boltzmann scheme against analytical solutions in order to quantify solution accuracy. The Lattice Boltzmann method was also verified to recover the complicated temperature contours in a bent domain.
- Characterized errors introduced into the system by various discretization/coupling restrictions; errors of this kind had not been estimated in previous reports.
- Experimental data was also recovered through an implementation of the multiscale coupling. The model was built to describe heat transport in a suspended silicon film. The experimental data, taken from literature, highlighted

the importance of including the effects of optical phonons in the Joule heat dissipation process. The experimental data was reproduced, thus verifying the developed methodology.

After the method was verified with experimental data a model was developed of a 6 finger GaN high electron mobility transistor. Details of the study contributions follow:

- A gray phonon dispersive model was incorporated into the transport model in order to observe the effects that boundary scattering and phonon confinement play on the final device temperature. Additionally, a two fluid model was developed in order to incorporate effects of optical phonons. Results show that there can be significant departures in temperature from diffusion based results. These results represent a unique study into the thermal behavior of these devices.
- In the development of the two-fluid model, the specific heat of GaN was modeled using the true shape of the Brillouin zone, and did not rely on any fitted parameters, such as the Debye temperature, that many other studies rely on. Adequate agreement with experimental results was obtained with the full Tersoff potential dispersion curves. Further refinement of the model showed that resolving the proper TO mode frequencies were critical in order to obtain accurate specific heat values at moderate temperatures.
- In addition to the specific heat calculations, a Brillouin zone velocity averaging scheme was developed in order to loosen the assumptions on dominant phonon propagation direction. The averaged velocities served as inputs into the two-fluid

transport model and will better capture the true nature of transport within a GaN device.

While the transport of phonons was studied in the second half of this work, an initial study into the behavior of phonon relaxation times was undertaken in the first half. These relaxation times dictate how transport is occurring within the bulk material and therefore a study into the nature of the thermal conductivity is possible once these times are quantified. The study presented here represents the most complete study into the nature of the bulk thermal conductivity of GaN to date. The analysis does not rely on simplifying assumptions on the shape of the Brillouin zone and only one fitted parameter was used in the model, whereas other studies can rely on 3 or more fitted constants. Details of the contributions are summarized as the following:

- Relaxation times from basic energy and momentum selection rules for all phonon modes in GaN have been calculated. These calculations were verified with experimental data collected at the Γ point with Raman Spectroscopy experiments, and were estimated for silent Raman modes as well. Previous relaxation time calculations assumed simplified dispersion curves or full calculations were performed only on the high energy phonon modes. Few studies on low energy phonon modes have been performed. This work found that is it critical to include contributions from both fission and fusion processes to describe the total relaxation time. This work also found that there is a transition point in which a fusion-based relaxation time begins to dominate over fission-based events. Previous studies were primarily concerned with fission-based events only. Relaxation time calculations were verified to be physically consistent with the

temperature behavior of the anharmonic parameter as well as theoretical frequency dependencies.

- Building upon the relaxation time calculations at the Γ point, issues of anisotropy within the optical phonon modes was discussed. These calculations verified a critical assumption used in electron transport models that the phonon relaxation time for high energy optical modes is only a weak function of the wavevector.
- Relaxation times were calculated for all acoustic phonon modes. At the time of writing there exists very little experimental data on the relaxation times for acoustic phonons. Therefore, theoretical calculations are used in order to characterize the wavevector dependence as well as temperature dependence on these quantities. The reported values were verified to recover the proper bulk thermal conductivity values and trends at high temperature.
- With all phonon modes characterized, it was possible to build model for the bulk thermal conductivity of GaN. The details of the model allowed for the nature of the thermal conductivity to be explored. At the time of writing, a lattice dynamical investigation into the thermal conductivity of GaN had not been constructed from basic energy and momentum conservation rules.

With the work presented here, a more complete understanding of the basic phonon characteristics as well as transport behavior in wurtzite GaN microelectronic devices is given.

6.2 Future Work/Opportunities

While this body of work presents advancements in the area of phonon transport in GaN, there are still investigations that can be performed in order to refine the developed models. The following suggestions are made as areas that can be developed further.

One of the basic assumptions made in this work is that the Tersoff potential adequately describes the phonon dispersion relationships. While bulk harmonic and anharmonic properties were captured with this potential, it was found to be inadequate at resolving the high-energy optical phonons for calculation of the relaxation time. This is primarily due to the fact that the TO phonon modes were not resolved correctly. Further investigation into other potential models such as the adiabatic bond charge model presented in [96] should be made prior to the development of more sophisticated transport models. With a full set of dispersion curves it would be possible to refine the understanding of anisotropy among the optical phonon modes, as well as assess their contribution to the total thermal conductivity. Additionally, the effect of band crossing should be addressed with any future refinements of the dispersion calculations. In future model refinements the dispersion calculations should be able to detect where a band crossing may occur. At this point the program would need to interrogate the eigenvectors of the dynamical matrix in the neighborhood of the crossing in order to categorize the phonon modes at that point. By properly categorizing the phonon modes it will be possible to continue with the finite difference group velocity calculation, however an alternative method referred to as the Hellman-Feynman theorem can be implemented if desired [134]. This method also requires that the eigenvectors of the dynamical matrix be calculated, making it a potentially costly computational step. Further investigations into the phonon relaxation times made with molecular dynamics simulations would also

provide an added level of understanding of some basic material properties. Using the Green-Kubo (heat flux auto-correlation function) expression for thermal conductivity it would be possible to extract bulk properties from these MD simulations. This type of study would help validate the GaN potential model, and could lead to further force field refinements if necessary.

In addition to studying basic phonon properties of GaN it would be advantageous to refine the transport models. While the framework presented here has included some effects of phonon dispersion, there are still refinements that can be incorporated in order to capture the details transport phenomena. As a next step in modeling phonon transport in GaN, one could make an isotropic dispersive model, based on work developed in [58]. This type of model will demand more computational resources, therefore it is suggested that parallelizing the computer code, or investigating other solution methodologies (implicit discretization of the BTE) should be investigated. If nanoscale devices are to be simulated, a switch away from the Lattice Boltzmann method might be necessary in order to improve the angular resolution of the transport.

Another task that should be investigated is the intimate coupling between the phonons in the material with high-energy electrons. By understanding the coupling mechanism it would be possible to refine the assumption that heat is preferentially being deposited into high energy LO phonon modes. Self-consistent solutions of both the electron and phonon transport should also be investigated. These simulations would provide a level of detailed information that would be useful for both mechanical engineers involved in thermal management as well as electrical engineers involved in pushing electrical performance to the limits. With simulations that contain this level of

detail, innovative ways to ensure the multiscale methodology is still computationally possible must be developed.

APPENDIX A

Initial comparisons between the discrete ordinates method (DOM) and the LBM have been performed in order to interrogate angular resolution issues. As described earlier, the discrete ordinates method allows for the angular domain to be discretized in a generalized manner. A 2D test problem was developed as shown in Figure 71. In this test problem the heat capacity of the phonons was fixed to a constant 2 JK^{-1} and the mean free path was taken to be 100 nm. The domain size was adjusted in order to enforce different transport regimes from ballistic to near-diffusive (Kn = 4, 2, 1, and 0.2). The temperature and heat flux distributions were then plotted throughout the domain. It is expected that at high Knudsen numbers (small domains) the angular resolution will play a major role in the accuracy of the LB method, while at smaller Knudsen numbers the two methods should yield similar results. It is desirable to know the point at which these two methods begin to diverge.

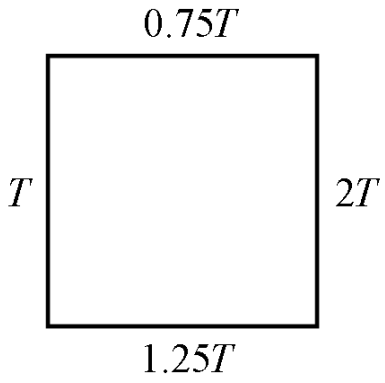

Figure 71: Test problem to investigate discrepancies between the Discrete Ordinates method and the Lattice Boltzmann method.

Each of the groups of results is for a fully converged (mesh independent) steady state solution. Since the DOM is a finite volume based scheme and the LBM is a finite difference based scheme the results from the LBM nodal solution had to be interpolated

to the node locations in the DOM spatial discretization. The following figures (Figure 72-Figure 75) show solutions of the test problem with the discrete ordinates method in the left column and the LB method in the right column. In Figure 72 (Kn = 4) and Figure 73 (Kn = 2) there are clear differences in both the temperature and heat flux distributions between the two methods; here the temperature has been nondimensionalized as $T^* = \left[T(x) - T_{left}\right] / \left[T_{right} - T_{left}\right]$. The error in the maximum temperature was 6.76% and 6.64% for the Kn = 4 x 4 and Kn = 2 x 2 cases, respectively. The error in the heat flux out each side of the domain is tabulated in Table 4.

Table 4: Heat fluxes across each of the boundaries in the test problem for both the discrete ordinates method as well as the Lattice Boltzmann method. Differences between the two methods are also calculated.

LBM Heat Fluxes [W]

Kn	*top*	*bottom*	*left*	*right*	**Maximum T***
0.2	7688.0	-1556.7	-10778.7	-1512.2	1.7489
1	2228.5	-69.0	-1017.5	-3320.1	1.5228
2	1186.8	29.2	-643.3	-1802.8	1.4752
4	608.0	36.9	-366.8	-939.0	1.4437

DOM Heat Fluxes [W]

Kn	*top*	*bottom*	*left*	*right*	**Maximum T***
0.2	8837.0	-1939.5	-11840.6	-1583.2	1.8108
1	2720.5	-182.0	-1066.3	-3960.1	1.6298
2	1472.5	-5.2	-715.2	-2197.7	1.5802
4	769.3	31.1	-424.3	-1167.2	1.5484

% Difference

Kn	*top*	*bottom*	*left*	*right*	**Maximum T***
0.2	13.0	19.7	9.0	4.5	3.42
1	18.1	62.1	4.6	16.2	6.57
2	19.4	663.2	10.1	18.0	6.64
4	21.0	-18.7	13.5	19.6	6.76

When investigating the Kn = 1 x 1 (Figure 74) case the tabulated errors continue to decrease for both the maximum temperature as well as the heat fluxes for each boundary. In the Kn = 0.2 x 0.2 case the error in the maximum temperature falls to 3.41% and the errors in the heat flux also continue to decline.

While these test cases highlight the need for finer angular resolution in domains with large Kn numbers, a full study of the LB method has not been attempted at this time and is left for future work. This study should include how factors such as domain geometry, transport regime, and boundary conditions, effect the final accuracy of the LB method.

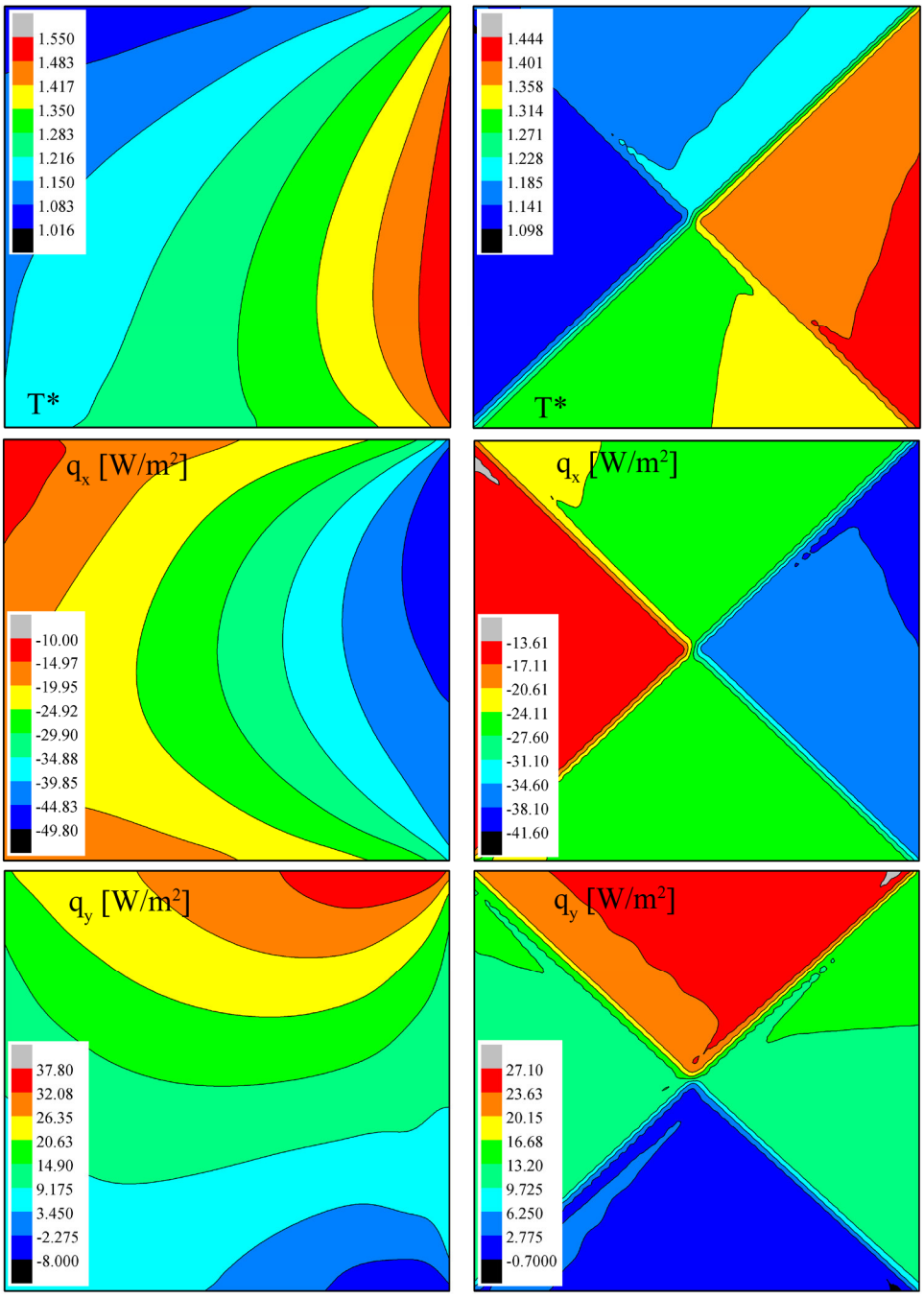

Figure 72: Comparison of DOM and LBM results for a domain measuring Kn = 4 x 4. The left column shows the results from the DOM method. The right column shows the results from the LBM method.

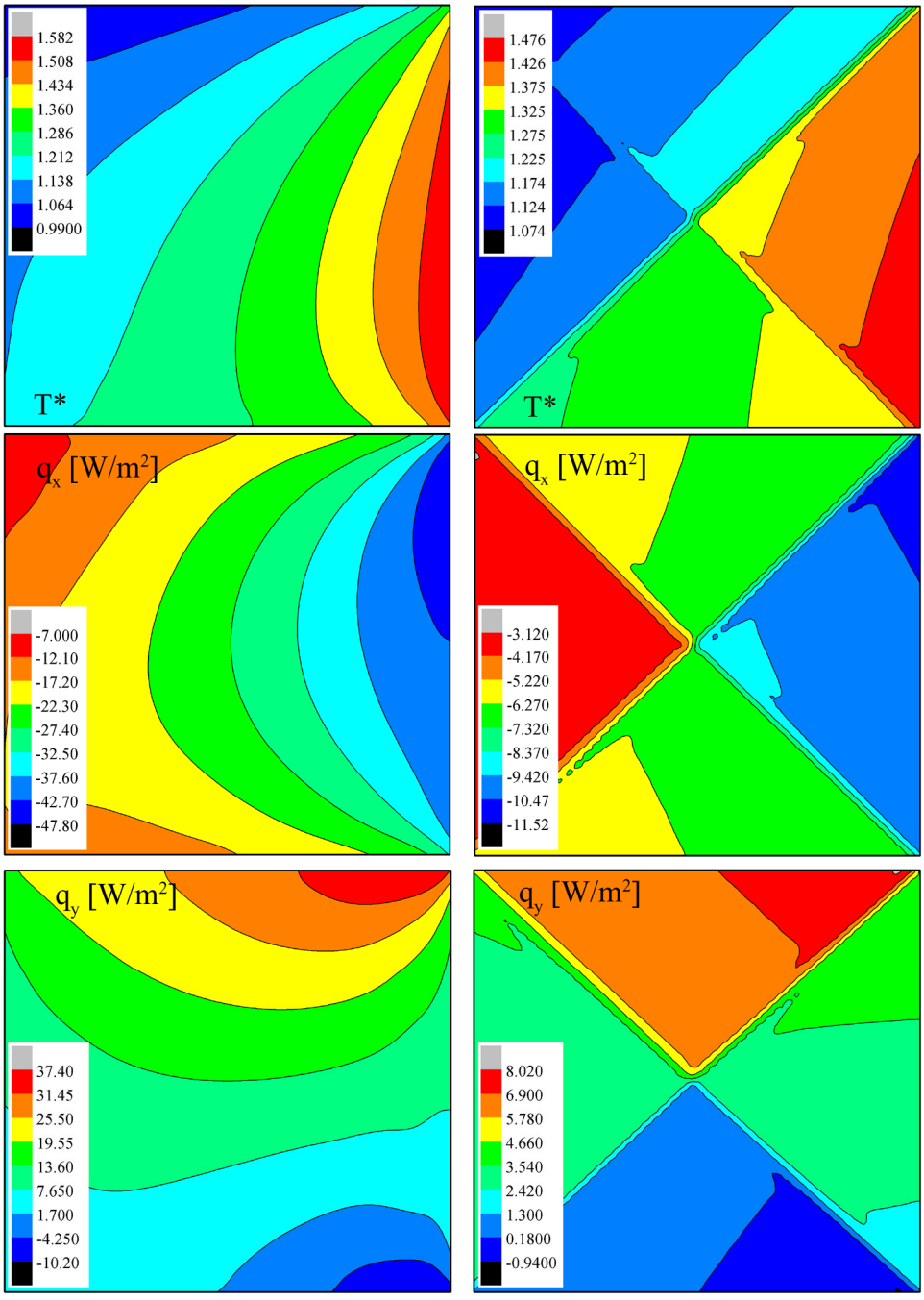

Figure 73: Comparison of DOM and LBM results for a domain measuring Kn = 2 x 2. The left column shows the results from the DOM method. The right column shows the results from the LBM method.

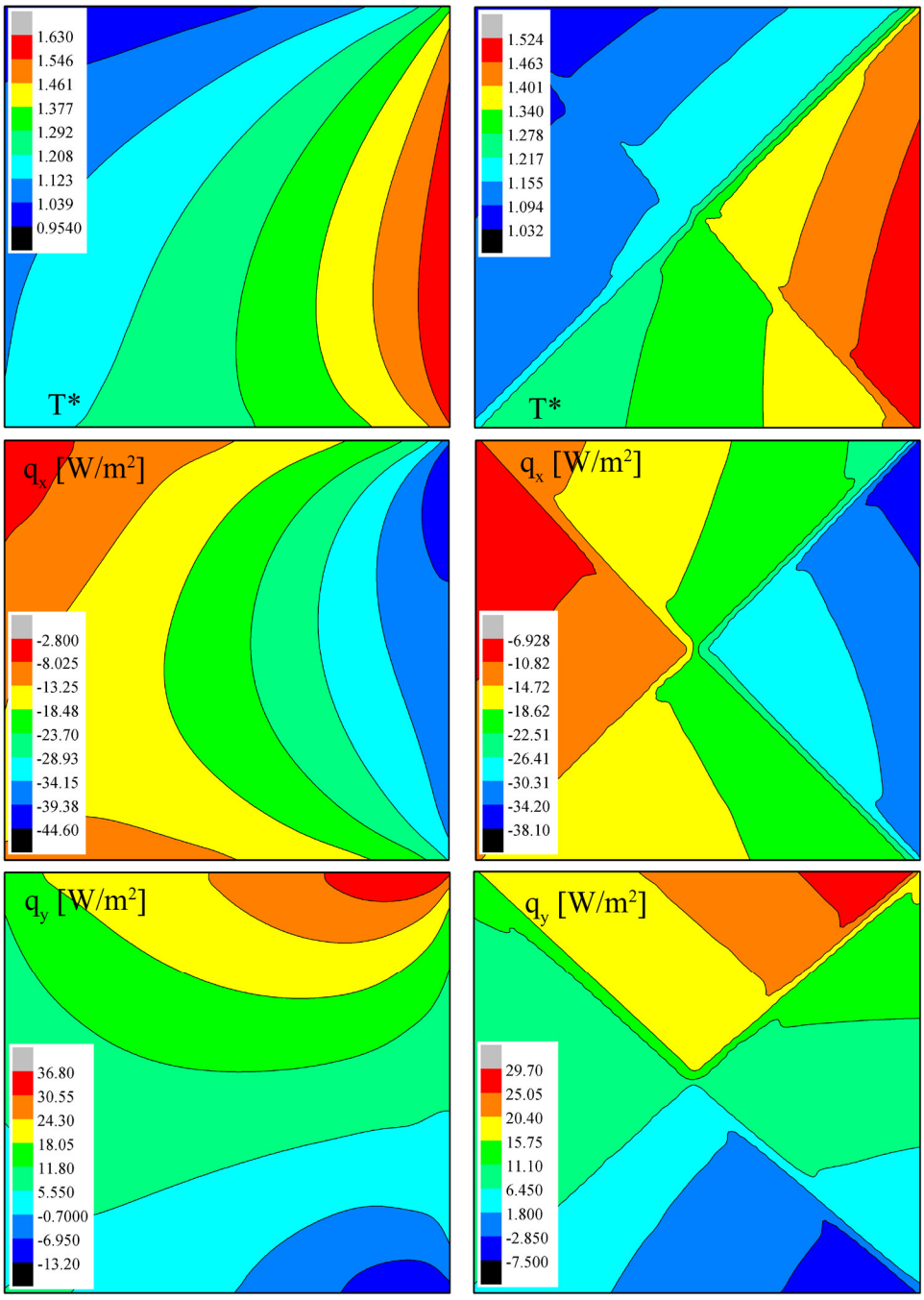

Figure 74: Comparison of DOM and LBM results for a domain measuring Kn = 1 x 1. The left column shows the results from the DOM method. The right column shows the results from the LBM method.

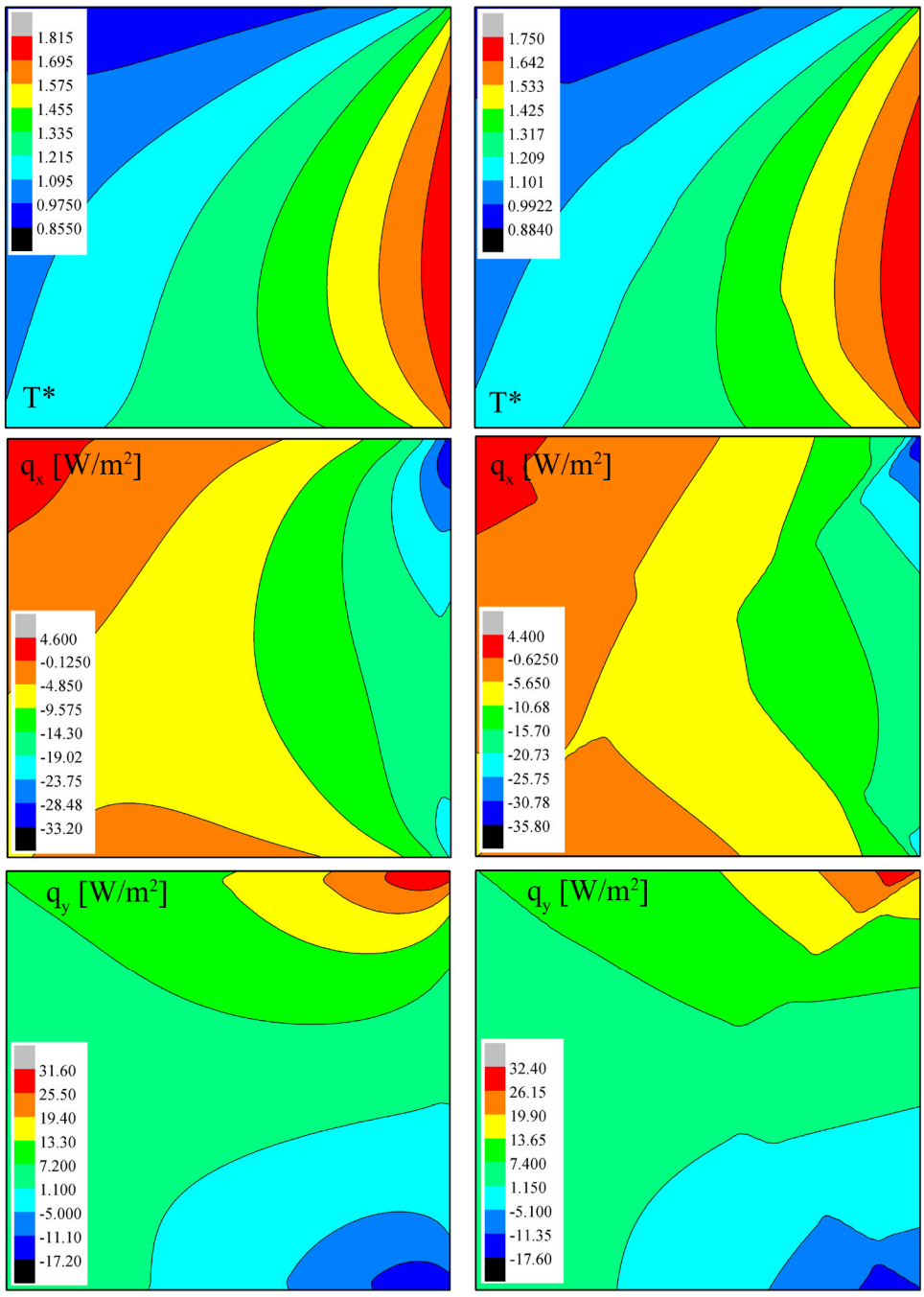

Figure 75: Comparison of DOM and LBM results for a domain measuring Kn = 0.2 x 0.2. The left column shows the results from the DOM method. The right column shows the results from the LBM method.

REFERENCES

[1] S. J. Pearton, *GaN and Related Materials* vol. 2. Amsterdam: Gordon and Breach Science Publications, 1997.

[2] S. Saygi, H. Fatima, X. He, S. Rai, A. Koudymov, V. Adivarahan, J. Yang, G. Simin, and M. A. Khan, "Performance stability of high-power III-nitride metal-oxide semiconductor-heterostructure field-effect transistors," *Physica Status Solidi (c),* vol. 2, pp. 2651-2654, 2005.

[3] M. O. Manasreh and H. X. Jiang, *III-Nitride Semiconductor Optical Properties 1* vol. 13. Amsterdam: Taylor & Francis Books, Inc., 2002.

[4] J. R. Shealy, J. A. Smart, M. J. Poulton, R. Sadler, D. Grider, S. Gibb, B. Hosse, B. Sousa, D. Halchin, V. Steel, P. Garber, P. Wilerson, P. Zaroff, B. Dick, J. Mercier, T. Bonaker, J. Hamilton, M. Greer, and M. Isenhour, "Gallium Nitride (GaN) HEMTs: Progress and potential for commerical applications," in *Gallium Arsenide Integrated Circuit (GaAs IC) Symposium*, 2002, pp. 243-246.

[5] K. Gurnett and T. Adams, "Consideration for GaN powered base stations," *III-Vs Review,* vol. 19, pp. 20-22, 2006.

[6] *Roadmap for wide bandgap semiconductors* vol. 3, 2007.

[7] J. Moon, J. Kim, and I. Kim, "GaN HEMT based Boherty amplifier for 3.5 GHz WiMAX Applications," in *Microwave Integrated Circuit Conference (EuMIC 2007)*, 2007, pp. 395-398.

[8] L. Kim, G. W. Lee, and W. J. Hwang, "Thermal analysis and design of GaN based LEDs for high power applications," *Physica Status Solidi (c),* vol. 0, pp. 2261-2264, 2003.

[9] Y. C. Chou, D. Leung, I. Smorchkova, M. Wojtowicz, R. Grundbacher, L. Callejo, Q. Kan, R. Lai, P. H. Liu, D. Eng, and A. Oki, "Degradation of AlGaN/GaN HEMTs under elevated temperature lifetesting," *Microelectronics Reliability,* vol. 44, pp. 1033-1038, Jul 2004.

[10] I. Daumiller, C. Kirchner, M. Kamp, K. J. Ebeling, and E. Kohn, "Evaluation of the temperature stability of AlGaN/GaN heterostructure FET's," *IEEE Electron Device Letters,* vol. 20, pp. 448-450, Sep 1999.

[11] H. Kim, V. Tilak, B. M. Green, J. A. Smart, W. J. Schaff, J. R. Shealy, and L. F. Eastman, "Reliability evaluation of high power AlGaN/GaN HEMTs on SiC substrate," *Physica Status Solidi A-Applied Research,* vol. 188, pp. 203-206, Nov 2001.

[12] S. Singhal, T. Li, A. Chaudhari, A. W. Hanson, R. Therrien, J. W. Johnson, W. Nagy, J. Marquart, P. Rajagopal, J. C. Roberts, E. L. Piner, I. C. Kizilyalli, and K. J. Linthicum, "Reliability of large periphery GaN-on-Si HFETs," *Microelectronics Reliability,* vol. 46, pp. 1247-1253, Aug 2006.

[13] M. Higashiwaki, T. Matsui, and T. Mimura, "AlGaN/GaN MIS HFETs with f(T) of 163 GHz using Cat-CVD SiN gate-insulating and passivation layers," *IEEE Electron Device Letters,* vol. 27, pp. 16-18, Jan 2006.

[14] P. Burgaud, L. Constancias, G. Martel, C. Savina, and D. Mesnager, "Preliminary reliability assessment and failure physical analysis on AlGaN/GaN HEMTs COTS," *Microelectronics Reliability,* vol. 47, pp. 1653-1657, 2007.

[15] T. Beechem, "Metrology of GaN electronics using micro-Raman Spectroscopy," Georgia Institute of Technology, 2008
[16] S. Sridharan, A. Venkatachalam, and P. D. Yoder, "Electrothermal analysis of AlGaN/GaN high electron mobility transistors," *Journal of Computational Electronics,* vol. 7, pp. 236-239, 2008.
[17] E. Pop, R. W. Dutton, and K. E. Goodson, "Monte Carlo simulation of Joule heating in bulk and strained silicon," *Applied Physics Letters,* vol. 86, Feb 2005.
[18] C. Bungaro, K. Rapcewicz, and J. Bernholc, "Ab initio phonon dispersions of wurtzite AlN, GaN, and InN," *Physical Review B,* vol. 61, pp. 6720-6725, Mar 2000.
[19] R. Quay, *GaN Electronics*: Springer, 2008.
[20] C. Ni and J. Y. Murthy, "Parallel computation of the phonon Boltzmann transport equation," *Numerical Heat Transfer Part B-Fundamentals,* vol. 55, pp. 435-456, 2009.
[21] S. Srinivasan, R. S. Miller, and E. Marotta, "Parallel computation of the Boltzmann transport equation for microscale heat transfer in multilayered thin films," *Numerical Heat Transfer Part B-Fundamentals,* vol. 46, pp. 31-58, Jul 2004.
[22] S. Sinha and K. E. Goodson, "Review: Multiscale thermal modeling in nanoelectronics," *International Journal for Multiscale Computational Engineering,* vol. 3, pp. 107-133, 2005.
[23] M. D. Kamatagi, N. S. Sankeshwar, and B. G. Mulimani, "Thermal conductivity of GaN," *Diamond and Related Materials,* vol. 16, pp. 98-106, Jan 2007.
[24] D. Kotchetkov, J. Zou, A. A. Balandin, D. I. Florescu, and F. H. Pollak, "Effect of dislocations on thermal conductivity of GaN layers," *Applied Physics Letters,* vol. 79, pp. 4316-4318, Dec 2001.
[25] X. G. Yu and X. G. Liang, "Effect of isotope on lattice thermal conductivity of lateral epitaxial overgrown GaN," *Diamond and Related Materials,* vol. 16, pp. 1711-1715, Sep 2007.
[26] J. Zou, D. Kotchetkov, A. A. Balandin, D. I. Florescu, and F. H. Pollak, "Thermal conductivity of GaN films: Effects of impurities and dislocations," *Journal of Applied Physics,* vol. 92, pp. 2534-2539, Sep 2002.
[27] C. Mion, J. Muth, E. Preble, and D. Hanser, "Temperature and dislcoation density effects on the thermal conductivity of bulk Gallium Nitride," in *Mater. Res. Soc. Symp. Proc.*, 2006, pp. 0892-FF29-05.1-6.
[28] W. L. Liu and A. A. Balandin, "Thermal conduction in AlxGa1-xN alloys and thin films," *Journal of Applied Physics,* vol. 97, Apr 2005.
[29] Z. Zhang, *Nano/Microscale Heat Transfer*. New York: McGraw-Hill, 2007.
[30] G. Chen, *Nanoscale energy transport and conversion: a parallel treatment of electrons molecules, phonons and photons*: Oxford University Press, 2005.
[31] G. P. Srivastava, *The Physics of Phonons*, 1990.
[32] C. Kittel, *Introduction to Solid State Physics*: Wiley Publishing, 2005.
[33] A. K. Ghatak and L. S. Kothari, *An Introduction to Lattice Dynamics*. London: Addison-Wesley Publishing, 1972.
[34] T. Wang, "Sub-micron thermal transport in ultra-scaled metal oxide semiconductor (MOS) devices," Purdue University, 2007

[35] N. Ashcroft and N. Mermin, *Solid State Physics*, 1976.
[36] P. G. Klemens, "The scattering of low-frequency lattice waves by static imperfections," *Proceedings of the Physical Society of London Section A,* vol. 68, pp. 1113-1128, 1955.
[37] P. G. Klemens, "Thermal conductivity and lattice vibrational modes," *Solid State Physics-Advances in Research and Applications,* vol. 7, pp. 1-98, 1958.
[38] D. C. Wallace, "Thermal expansion and other anharmonic properties of crystals," *Physical Review,* vol. 139, pp. A877-&, 1965.
[39] J. M. Ziman, *Electrons and Phonons*, 1960.
[40] R. Berman, *Thermal conduction in solids*. London: Claredon Press, 1975.
[41] C. Herring, "Role of low energy phonons in thermal conduction," *Physical Review,* vol. 95, pp. 954-965, 1954.
[42] P. G. Klemens, "The thermal conductivity of dielectric solids at low temperatures - theoretical," *Proceedings of the Royal Society of London Series a-Mathematical and Physical Sciences,* vol. 208, pp. 108-133, 1951.
[43] P. G. Klemens, *Solid State Physics* vol. 7. New York: Academic Press Inc., 1958.
[44] M. G. Holland, "Analysis of lattice thermal conductivity," *Physical Review,* vol. 132, pp. 2461-2471, 1963.
[45] J. Callaway, "Model for lattice thermal conductivity at low temperatures," *Physical Review,* vol. 113, pp. 1046-1051, 1959.
[46] G. Chen, "Ballistic-diffusive heat-conduction equations," *Physical Review Letters,* vol. 86, pp. 2297-2300, Mar 2001.
[47] G. Chen, "Ballistic-diffusive equations for transient heat conduction from nano to macroscales," *Journal of Heat Transfer-Transactions of the ASME,* vol. 124, pp. 320-328, Apr 2002.
[48] G. Chen and T. F. Zeng, "Nonequilibrium phonon and electron transport in heterostructures and superlattices," *Microscale Thermophysical Engineering,* vol. 5, pp. 71-88, Apr-Jun 2001.
[49] R. G. Yang, G. Chen, M. Laroche, and Y. Taur, "Simulation of nanoscale multidimensional transient heat conduction problems using ballistic-diffusive equations and phonon Boltzmann equation," *Journal of Heat Transfer-Transactions of the ASME,* vol. 127, pp. 298-306, Mar 2005.
[50] J. Y. Murthy and S. R. Mathur, "Ballistic-diffusive approximation for phonon transport accounting for polarization and dispersion," in *Proceedings of the ASME Summer Heat Transfer Conference, Paper No. HT2004-47491*, 2003.
[51] N. Mingo and L. Yang, "Phonon transport in nanowires coated with an amorphous material: An atomistic Green's function approach," *Physical Review B,* vol. 68, 2003.
[52] W. Zhang, T. S. Fisher, and N. Mingo, "Simulation of interfacial phonon transport in Si-Ge heterostructures using an atomistic Green's function method," *Journal of Heat Transfer-Transactions of the Asme,* vol. 129, pp. 483-491, 2007.
[53] N. Mingo, "Anharmonic phonon flow through molecular-sized junctions," *Physical Review B,* vol. 74, Sep 2006.
[54] K. Brennan, *Physics of Semiconductors with Applications to Optoelectronic Devices*. New York: Cambridge University Press, 1999.

[55] C. Ni, "Phonon transport models for heat conduction in sub-micron geometries with application to microelectronics," Purdue University, 2008
[56] I. Pomeranchuk, "On the thermal conductivity of dielectrics at the temperatures higher than the Debye temperature," *Journal of Physics-USSR,* vol. 4, pp. 259-268, 1941.
[57] A. Majumdar, "Microscale heat conduction in dielectric thin films," *Journal of Heat Transfer,* vol. 115, pp. 7-16, Feb 1993.
[58] S. V. J. Narumanchi, J. Y. Murthy, and C. H. Amon, "Submicron heat transport model in silicon accounting for phonon dispersion and polarization," *Journal of Heat Transfer-Transactions of the ASME,* vol. 126, pp. 946-955, Dec 2004.
[59] P. G. Sverdrup, Y. S. Ju, and K. E. Goodson, "Sub-continuum simulations of heat conduction in silicon-on-insulator transistors," *Journal of Heat Transfer,* vol. 123, pp. 130-137, Feb 2001.
[60] Y. S. Ju and K. E. Goodson, *Microscale heat conduction in integrated circuits and their constituent films*: Kluwer Academic Publishers, 1999.
[61] S. V. J. Narumanchi, J. Y. Murthy, and C. H. Amon, "Comparison of different phonon transport models for predicting heat conduction in silicon-on-insulator transistors," *Journal of Heat Transfer,* vol. 127, pp. 713-723, Jul 2005.
[62] S. Usher and G. P. Srivastava, "Theoretical study of the anharmonic decay of nonequilibrium LO phonons in semiconductor structures," *Physical Review B,* vol. 50, pp. 14179-14186, Nov 1994.
[63] Y. J. Han and P. G. Klemens, "Anharmonic thermal resistivity of dielectric crystals at low temperatures," *Physical Review B,* vol. 48, pp. 6033-6042, Sep 1993.
[64] C. Ni and J. Y. Murthy, "Sub-micron thermal transport modeling by phonon Boltzmann transport with anisotroipic relaxation times," in *IEEE Thermal and Thermomechanical Phenomena in Electronic Systems Conference, ITHERM*, 2008.
[65] S. Mazumder and A. Majumdar, "Monte Carlo study of phonon transport in solid thin films including dispersion and polarization," *Journal of Heat Transfer,* vol. 123, pp. 749-759, Aug 2001.
[66] D. Lacroix, K. Joulain, and D. Lemonnier, "Monte Carlo transient phonon transport in silicon and germanium at nanoscales," *Physical Review B,* vol. 72, Aug 2005.
[67] J. Randrianalisoa and D. Baillis, "Monte Carlo simulation of cross-plane thermal conductivity of nanostructured porous silicon films," *Journal of Applied Physics,* vol. 103, Mar 2008.
[68] M. S. Jeng, R. G. Yang, D. Song, and G. Chen, "Modeling the thermal conductivity and phonon transport in nanoparticle composites using Monte Carlo simulation," *Journal of Heat Transfer-Transactions of the ASME,* vol. 130, 2008.
[69] S. Succi, *The lattice Boltzmann equation for fluid dynamics and beyond*, 2001.
[70] R. Benzi, S. Succi, and M. Vergassola, "The Lattice Boltzmann Equation - Theory and Applications," *Physics Reports-Review Section of Physics Letters,* vol. 222, pp. 145-197, Dec 1992.
[71] R. A. Escobar, S. S. Ghai, M. S. Jhon, and C. H. Amon, "Multi-length and time scale thermal transport using the lattice Boltzmann method with application to

electronics cooling," *International Journal of Heat and Mass Transfer,* vol. 49, pp. 97-107, Jan 2006.

[72] R. Escobar, B. Smith, and C. Amon, "Lattice Boltzmann modeling of subcontinuum energy transport in crystalline and amorphous microelectronic devices," *Journal of Electronic Packaging,* vol. 128, pp. 115-124, Jun 2006.

[73] W. S. Jiaung and J. R. Ho, "Lattice Boltzmann study on size effect with geometrical bending on phonon heat conduction in a nanoduct," *Journal of Applied Physics,* vol. 95, pp. 958-966, Feb 2004.

[74] S. S. Ghai, W. T. Kim, C. H. Amon, and M. S. Jhon, "Transient thermal modeling of a nanoscale hot spot in multilayered film," *Journal of Applied Physics,* vol. 99, Apr 2006.

[75] S. S. Ghai, W. T. Kim, R. A. Escobar, C. H. Amon, and M. S. Jhon, "A novel heat transfer model and its application to information storage systems," *Journal of Applied Physics,* vol. 97, May 2005.

[76] R. A. Escobar and C. H. Amon, "Influence of phonon dispersion on transient thermal response of silicon-on-insulator transistors under self-heating conditions," *Journal of Heat Transfer,* vol. 129, pp. 790-797, Jul 2007.

[77] R. Escobar, "Lattice Boltzmann modeling of phonon transport in silicon films," Carnegie Mellon University, 2005

[78] G. W. Peng, H. W. Xi, C. Duncan, and S. H. Chou, "Finite volume scheme for the lattice Boltzmann method on unstructured meshes," *Physical Review E,* vol. 59, pp. 4675-4682, Apr 1999.

[79] H. W. Xi, G. W. Peng, and S. H. Chou, "Finite-volume lattice Boltzmann method," *Physical Review E,* vol. 59, pp. 6202-6205, May 1999.

[80] M. Stiebler, J. Tolke, and M. Krafczyk, "An upwind discretization scheme for the finite volume lattice Boltzmann method," in *Computers & Fluids*, 2006, pp. 814-819.

[81] S. Ubertini, G. Bella, and S. Succi, "Lattice Boltzmann method on unstructured grids: Further developments," *Physical Review E,* vol. 68, Jul 2003.

[82] N. Rossi, S. Ubertini, G. Bella, and S. Succi, "Unstructured lattice Boltzmann method in three dimensions," *International Journal for Numerical Methods in Fluids,* vol. 49, pp. 619-633, Oct 2005.

[83] D. Wolf-Gladrow, *Lattice-Gas Cellular Automata and Lattice Boltzmann Models*. Berlin: Springer, 2000.

[84] X. Y. He and L. S. Luo, "Theory of the lattice Boltzmann method: From the Boltzmann equation to the lattice Boltzmann equation," *Physical Review E,* vol. 56, pp. 6811-6817, Dec 1997.

[85] Q. Zou and X. He, "On pressure and velocity boundary conditions for the Lattice Boltzmann BGK model," *Physics of Fluids,* vol. 9, pp. 1591-1598, 1997.

[86] M. I. Flik and C. L. Tien, "Size effect on the thermal conductivity of high-Tc thin film superconductors," *Journal of Heat Transfer,* vol. 112, pp. 872-881, Nov 1990.

[87] C. R. Tellier, "Size effects on thermal properties of thin metal films with rough surfaces," *Active and Passive Electronic Components,* vol. 14, pp. 1-16, 1990.

[88] U. Frisch, D. d'Humieres, B. Hasslacher, P. Lallemand, Y. Pomeau, and J. Rivet, "Lattice gas hydrodynamics in two and three dimensions," *Complex Systems,* vol. 1, pp. 649-707, 1987.

[89] P. Albuquerque, D. Alemani, B. Chopard, and P. Leone, "Coupling a Lattice Boltzmann and a finite difference scheme," in *International Conference on Computational Science* Krakow, Poland, 2004.

[90] P. Heino, "Multiscale Lattice Boltzmann finite difference model for thermal conduction from nanoscale hot spots," *International Journal for Multiscale Computational Engineering,* vol. 6, pp. 169-178, 2008.

[91] J. Nord, K. Albe, P. Erhart, and K. Nordlund, "Modelling of compound semiconductors: analytical bond-order potential for gallium, nitrogen and gallium nitride," *Journal of Physics-Condensed Matter,* vol. 15, pp. 5649-5662, Aug 2003.

[92] A. Greenstein, "Analysis of thermal conductivity models with an extension to complex crystalline materials," *PhD Dissertation*, Georgia Institute of Technology, 2008

[93] R. R. Reeber and K. Wang, "Lattice parameters and thermal expansion of GaN," *Journal of Materials Research,* vol. 15, pp. 40-44, Jan 2000.

[94] C. Roder, S. Einfeldt, S. Figge, and D. Hommel, "Temperature dependence of the thermal expansion of GaN," *Physical Review B,* vol. 72, Aug 2005.

[95] J. D. Gale and A. L. Rohl, "The General Utility Lattice Program (GULP)," *Molecular Simulation,* vol. 29, pp. 291-341, Apr 2003.

[96] H. M. Tutuncu and G. P. Srivastava, "Phonons in zinc-blende and wurtzite phases of GaN, AlN, and BN with the adiabatic bond-charge model," *Physical Review B,* vol. 62, pp. 5028-5035, Aug 2000.

[97] R. K. Kremer, M. Cardona, E. Schmitt, J. Blumm, S. K. Estreicher, M. Sanati, M. Bockowski, I. Grzegory, T. Suski, and A. Jezowski, "Heat capacity of alpha-GaN: Isotope effects," *Physical Review B,* vol. 72, Aug 2005.

[98] G. P. Srivastava, "The anharmonic phonon decay rate in group-III nitrides," *Journal of Physics-Condensed Matter,* vol. 21, Apr 2009.

[99] X. W. Zhou, S. Aubry, R. E. Jones, A. Greenstein, and P. K. Schelling, "Towards more accurate molecular dynamics calculation of thermal conductivity: Case study of GaN bulk crystals," *Physical Review B,* vol. 79, Mar 2009.

[100] A. Ladd, B. Moran, and W. Hoover, "Lattice thermal conductivity: A comparison of molecular dynamics and anharmonic lattice dynamics," *Physical Review B,* vol. 34, pp. 5058-5064, 1986.

[101] L. Bohlin and T. Hogberg, "Anharmonic phonon shifts and widths for a centro-symmetrical potential," *Journal of Physics and Chemistry of Solids,* vol. 29, pp. 1805-1821, 1968.

[102] A. Maradudin and A. Fein, "Scattering of neutrons by an anharmonic crystal," *Physical Review,* vol. 128, pp. 2589-2608, 1962.

[103] J. Turney, E. Landry, A. J. H. McGaughey, and C. Amon, "Predicting phonon properties and thermal conductivity from anharmonic lattice dynamics calculations and molecular dynamics simulations," *Physical Review B,* vol. 79, p. 064301, 2009.

[104] G. P. Srivastava, "Origin of the hot phonon effect in group-III nitrides," *Physical Review B,* vol. 77, Apr 2008.
[105] D. Hutton, *Fundamentals of finite element analysis*: McGraw-Hill Professional, 2003.
[106] P. G. Klemens, "Anharmonic decay of optical phonons," *Physical Review,* vol. 148, p. 845, 1966.
[107] B. K. Ridley, *Quantum Processes in Semiconductors*, 1999.
[108] S. Barman and G. P. Srivastava, "Long-wavelength nonequilibrium optical phonon dynamics in cubic and hexagonal semiconductors," *Physical Review B,* vol. 69, Jun 2004.
[109] F. Vallee, "Time resolved investigation of coherent LO phonon relaxation in III-V semiconductors," *Physical Review B,* vol. 49, pp. 2460-2468, 1994.
[110] F. Vallee and F. Bogani, "Coherent time-resolved investigation of LO phonon dynamics in GaAs," *Physical Review B,* vol. 43, pp. 12049-12052, May 1991.
[111] T. Beechem and S. Graham, "Temperature and doping dependence of phonon lifetimes and decay pathways in GaN," *Journal of Applied Physics,* vol. 103, May 2008.
[112] L. Bergman, D. Alexson, P. L. Murphy, R. J. Nemanich, M. Dutta, M. A. Stroscio, C. Balkas, H. Shin, and R. F. Davis, "Raman analysis of phonon lifetimes in AlN and GaN of wurtzite structure," *Physical Review B,* vol. 59, pp. 12977-12982, May 1999.
[113] A. Link, K. Bitzer, W. Limmer, R. Sauer, C. Kirchner, V. Schwegler, M. Kamp, D. G. Ebling, and K. W. Benz, "Temperature dependence of the E2 and A(1)(LO) phonons in GaN and AlN," *Journal of Applied Physics,* vol. 86, pp. 6256-6260, Dec 1999.
[114] D. Y. Song, S. A. Nikishin, M. Holtz, V. Soukhoveev, A. Usikov, and V. Dmitriev, "Decay of zone-center phonons in GaN with A(1), E1, and E2 symmetries," *Journal of Applied Physics,* vol. 101, Mar 2007.
[115] K. T. Tsen, D. K. Ferry, A. Botchkarev, B. Sverdlov, A. Salvador, and H. Morkoc, "Time-resolved Raman studies of the decay of the longitudinal optical phonons in wurtzite GaN," *Applied Physics Letters,* vol. 72, pp. 2132-2134, Apr 1998.
[116] K. T. Tsen, J. G. Kiang, D. K. Ferry, and H. Morkoc, "Subpicosecond time-resolved Raman studies of LO phonons in GaN: Dependence on photoexcited carrier density," *Applied Physics Letters,* vol. 89, Sep 2006.
[117] S. Tripathy, S. J. Chua, and A. Ramam, "Electronic and vibronic properties of n-type GaN: the influence of etching and annealing," *Journal of Physics-Condensed Matter,* vol. 14, pp. 4461-4476, May 2002.
[118] B. Hejda and K. Kral, "Hot electron cooling and second generation phonons in polar semiconductors," *Physical Review B,* vol. 47, pp. 15554-15561, Jun 1993.
[119] J. W. Pomeroy, M. Kuball, H. Lu, W. J. Schaff, X. Wang, and A. Yoshikawa, "Phonon lifetimes and phonon decay in InN," *Applied Physics Letters,* vol. 86, May 2005.
[120] D. Posener, "The shape of spectral lines: tables of the Voigt profile," *Australian Journal of Physics,* vol. 12, p. 184, 1959.

[121] T. Paskova, *Nitrides with nonpolar surfaces: growth, properties, and devices*: Wiley Publishing, 2008.
[122] T. M. Liu, S. Z. Sun, C. F. Chang, C. C. Pan, G. T. Chen, J. I. Chyi, V. Gusev, and C. K. Sun, "Anharmonic decay of subterahertz coherent acoustic phonons in GaN," *Applied Physics Letters,* vol. 90, Jan 2007.
[123] T. Beechem, A. Christensen, S. Graham, and D. Green, "Micro-Raman thermometry in the presence of complex stresses in GaN devices," *Journal of Applied Physics,* vol. 103, Jun 2008.
[124] W. L. Liu and A. Balandin, "Thermal conduction in Al[sub x]Ga[sub 1 - x]N alloys and thin films," *Journal of Applied Physics,* vol. 97, pp. 073710-6, 2005.
[125] A. Jezowski, B. A. Danilchenko, M. Bockowski, I. Grzegory, S. Krukowski, T. Suski, and T. Paszkiewicz, "Thermal conductivity of GaN crystals in 4.2-300 K range," *Solid State Communications,* vol. 128, pp. 69-73, Oct 2003.
[126] C. Luo, D. R. Clarke, and J. R. Dryden, "The temperature dependence of the thermal conductivity of single crystal GaN films," *Journal of Electronic Materials,* vol. 30, pp. 138-146, Mar 2001.
[127] T. Kawamura, Y. Kangawa, and K. Kakimoto, "Investigation of thermal conductivity of GaN by molecular dynamics," *Journal of Crystal Growth,* vol. 284, pp. 197-202, 2005.
[128] A. Christensen, "Thermal Transport in III-V Semiconductors and Devices," *MS*, Georgia Institute of Technology, 2006
[129] P. G. Sverdrup, S. Sinha, M. Asheghi, S. Uma, and K. E. Goodson, "Measurement of ballistic phonon conduction near hotspots in silicon," *Applied Physics Letters,* vol. 78, pp. 3331-3333, May 2001.
[130] B. H. Armstrong, "2-Fluid theroy of thermal conductivity of dielectric crystals," *Physical Review B,* vol. 23, pp. 883-899, 1981.
[131] V. Bougrov, M. E. Levinshtein, S. L. Rumyantsev, and A. Zubrilov, *Properties of Advanced Semiconductor Materials GaN, AlN, InN, BN, SiC, SiGe*. New York: John Wiley & Sons, 2001.
[132] O. Nilsson, R. Mehling, R. Horn, J. Fricke, R. Hofmann, S. G. Muller, R. Eckstein, and D. Hofmann, "Determination of the thermal diffusivity and conductivity of monocrystalline silicon carbide (300 - 2300 K)," *High Temperatures High Pressures,* vol. 29, pp. 73-79, 1997.
[133] S. Sridharan, A. Venkatachalam, and P. D. Yoder, "Electrothermal analysis of AlGaN/GaN high electron mobility transistors," *Journal of Computational Electronics* vol. 7, pp. 236-239, 2008.
[134] D. C. Wallace, *Thermodynamics of Crystals*, 1972.